UNIVERSITY OF CALIFORNIA,
IRVINE

Extreme Precipitation Modeling Using Remotely-Sensed Information and Advanced Statistical Techniques

DISSERTATION

submitted in partial satisfaction of the requirements
for the degree of

DOCTOR OF PHILOSOPHY

in Civil Engineering

by

Mohammad Faridzad

Dissertation Committee:
Distinguished Professor Soroosh Sorooshian, Co-Chair
Professor Kuolin Hsu, Co-Chair
Professor Brett Sanders

2019

DEDICATION

This dissertation is wholeheartedly dedicated to
My dear parents, Farideh and Mohammad
My beloved wife and my best friend, Ferial
and my lovely brother, Pedram
In recognition of their worth

TABLE OF CONTENTS

LIST OF FIGURES

LIST OF TABLES

ACKNOWLEDGMENTS

The Ph.D. journey has been an absolutely life-changing experience for me. As I get closer to the end of this journey, I would like to acknowledge those people who helped, supported, and kept me motivated during these years. Individuals whom without their support, guidance, and encouragements, this thesis would not have been possible.

First an foremost, I would like to extend my deepest appreciation to my dear advisor, Professor Soroosh Sorooshian, for his invaluable guidance, continuous support, and insightful advice throughout my Ph.D. program. I am extremely grateful for having the opportunity to work under his supervision and benefit from his immense knowledge at the Center for Hydrometeorology and Remote Sensing (CHRS), where I was exposed to state-of-the-art in hydrology, hydrometeorology, and remote sensing. He showed me how to look at problems from a broader perspective and how to think out of the box. I am truly thankful for his unconditional support, continuous encouragements, and lifelong lessons which were accompanied by his humble and great personality. I would also like to express my sincere gratitude and appreciation to my co-advisor, Professor Kuolin Hsu, who immensely supported and helped me during this research. His knowledge and expertise in various areas of hydrology and remote sensing, together with his humbleness has always amazed and inspired me. This dissertation would not have been possible without his vast knowledge, patience, and exceptional support.

I must thank Professor Tiantian Yang, for his support and mentorship in various stages of my Ph.D. studies. He helped me since the earliest stages of my Ph.D. research and continuously supported me until the final days. He was a great source of motivation and encouragement for me.

I would also like to extend my gratitude to my Ph.D. committee members, Professor Brett Sanders and Professor Charless Fowlkess for their constructive comments and invaluable suggestions in my qualifying exam, as well as during my Ph.D. studies, all of which enhanced the quality of this research considerably.

Many thanks to my colleagues and friends at CHRS who made my Ph.D. years a lot more pleasing and memorable. I appreciate Mr. Dan Braithwaite for all his technical support and assistance with data, IT, and programming. Also, I wish to thank Mrs. Diane Hohnbaum for her administrative assistance and for her kind advice in every step of my Ph.D. program. I am forever thankful to all of my friends at CHRS whom I had the honor and privilege of working with. I wish all of them success in their life and career.

I am extremely grateful and indebted to my dear parents, Farideh and Mohammad, for their endless love, sacrifice, and support. They taught me how to follow my dreams and helped me achieve my goals. I wish this dissertation can serve as a tiny gift from me to them in recognition of what they have done for me. I also wish to thank my dear brother, Pedram, for his encouragement and support in whatever he could during my entire life.

Last but not least, I would like to express my deepest gratitude to my lovely wife and my best friend, Ferial, for her unconditional love and her endless support and patience. Ferial, I cannot find enough words to express how grateful I am for the piece and love you have brought to my life. Without your support, this dissertation would not have been completed. Also, I would like to express my sincere appreciation to my extended family, my mother, father, and brother in-law, for their endless support and encouragement.

I would also like to express my sincere gratitude to Dr. Fariborz Maseeh, who provided resources to to financially support me during the first year of my Ph.D. studies. The financial support of this research is from U.S. Department of Energy (DOE Prime Award # DE-IA0000018), California Energy Commission (CEC Award # 300-15-005), MASEEH fellowship, NSF CyberSEES Project (Award CCF-1331915), NOAA/NESDIS/NCDC (Prime award NA09NES4400006 and NCSU CICS and subaward 2009-1380-01), the U.S. Army Research Office (award W911NF-11-1-0422) and the National Key R& D Program of China (Grant No. 2016YFE0102400). Without this support, this thesis would not have been possible.

CURRICULUM VITAE

Mohammad Faridzad

EDUCATION

Doctor of Philosophy in Civil Engineering **2019**
University of California, Irvine *Irvine, CA*

Master of Science in Environmental Engineering **2013**
University of California, Irvine *Irvine, CA*

Bachelor of Science in Civil and Environmental Engineering **2010**
AmirKabir University of Technology (Tehran Polytechnic) *Tehran, Iran*

RESEARCH EXPERIENCE

Graduate Research Assistant **2015–2019**
University of California, Irvine *Irvine, California*

TEACHING AND MENTORING EXPERIENCE

Teaching Assistant, Surface Water Hydrology (ENGRCEE 176/276) **2017**
Instructor: Prof. Sorooshian
University of California, Irvine *Irvine, CA*

PROFESSIONAL EXPERIENCE

Reviewer, Peer-reviewed Journals **2016–Present**

- Journal of Hydrology
- Remote Sensing
- Journal of Hydrologic Engineering
- Agricultural Water Management
- Applied Soft Computing

Research Scholar **2013–2015**
EWRC, Sharif University of Technology *Tehran, Iran*

- Processing remote sensing (RS) data for hydrological and agricultural applications
- Evaluating the climate change impacts on crop water use and water balance
- Spatiotemporal modeling of evapotranspiration using RS and meteorological data
- Estimating annual water balance, irrigation performance, and water productivity
- Optimizing site selection to maximize the effectiveness of land use change on restoration of a drying lake

PEER-REVIEWED JOURNAL PAPERS

Mohammad Faridzad, Tiantian Yang, Kuolin Hsu, Soroosh Sorooshian, Spatial Modeling of Extreme Precipitation Using Satellite Information and a Bayesian Hierarchical Framework **2019**
In Preparation

Mohammad Faridzad, Tiantian Yang, Kuolin Hsu, Soroosh Sorooshian, Extreme Precipitation Modeling for the Pacific Northwest United States Using Satellite Information and Max-Stable Processes **2019**
In Preparation

Mojtaba Sadeghi, Ata Akbari Asanjan, Mohammad Faridzad, Vesta Afzali Grooh, Phu Nguyen, Kuolin Hsu, Soroosh Sorooshian, Evaluation of PERSIANN-CDR Constructed using GPCP V2.2 & V2.3 and a Comparison with TRMM 3B42 V7 and CPC Unified Gauge-based Analysis in Global Scale **2019**
Remote Sensing, 11, 2755

Mojtaba Sadeghi, Ata Akbari Asanjan, Mohammad Faridzad, Phu Nguyen, Kuolin Hsu, Soroosh Sorooshian, Dan Braithwaite, PERSIANN-CNN: Precipitation Estimation from Remotely Sensed Information Using Artificial Neural Networks - Convolutional Neural Networks **2019**
Journal of Hydrometeorology

Mohammad Faridzad, Tiantian Yang, Kuolin Hsu, Soroosh Sorooshian, Rainfall Frequency Analysis For Ungauged Regions Using Remotely Sensed Precipitation Information **2018**
Journal of Hydrology, 563, 123–142.

Tiantian Yang, Ata Akbari Asanjan, Mohammad Faridzad, Negin Hayatbini, Kuolin Hsu, Soroosh Sorooshian, An enhanced artificial neural network with a shuffled complex evolutionary global optimization with principal component analysis **2017**
Information Sciences, 418, 302–316.

CONFERENCE PRESENTATIONS(ORAL)

Mohammad Faridzad, Tiantian Yang, Kuolin Hsu, Soroosh Sorooshian, Spatial Extreme Precipitation Modeling for The Pacific Northwest United States Using Satellite Information and Max-Stable Processes — **Dec 2019**
American Geophysical Union(AGU) Fall Meeting, San Francisco, CA

Mohammad Faridzad, Tiantian Yang, Kuolin Hsu, Soroosh Sorooshian, An Application Framework for the Use of Satellite Precipitation Data for Rainfall Frequency Analysis in Ungauged Regions — **Dec 2018**
American Geophysical Union(AGU) Fall Meeting, Washington D.C.

Mohammad Faridzad, Peyman Saemian, Trend Analysis of Chlorophyll Concentration Changes in Caspian Sea, Using MODIS Satellite Data — **Feb 2013**
1st International Conference on Environmental Crises and Solution, Kish, Iran

CONFERENCE PRESENTATIONS(POSTER)

Mohammad Faridzad, Tiantian Yang, Kuolin Hsu, Soroosh Sorooshian, Spatial Extreme Precipitation Modeling Using Satellite Information and Bayesian Hierarchical Models — **June 2019**
12th International Precipitation Conference (IPC12), Irvine, CA

Mohammad Faridzad, Tiantian Yang, Kuolin Hsu, Soroosh Sorooshian, Bias-correction of PERSIANN-CDR Extreme Precipitation Estimates Over the United States — **Dec 2017**
American Geophysical Union(AGU) Fall Meeting, New Orleans, LA

Negin Hayatbini, Mohammad Faridzad, Tiantian Yang, Ata Akbari Asanjan, Xiaogang Gao, Soroosh Sorooshian, A New Artificial Neural Network Enhanced by the Shuffled Complex Evolution Optimization with Principal Component Analysis (SP-UCI) for Water Resources Management — **Dec 2016**
American Geophysical Union(AGU) Fall Meeting, San Francisco, CA

HONORS & AWARDS

Outstanding Engineering Student of the Year **2018**
Orange County Engineering Council(OCEC)

Travel Grant for the 2017 AGU Fall Meeting, New Orleans, LA **2018**
Henry Samueli School of Engineering, University of California, Irvine

Travel Grant for the 2016 AGU Fall Meeting, San Francisco, CA **2017**
Department of Civil and Environmental Eng., University of California, Irvine

Maseeh Fellowship **2015–2016**
Massiah Foundation, Irvine California

TECHNICAL SKILLS

Programming: Proficient in R and MATLAB. Familiar with Python and FORTRAN
Modeling Tools: HEC-HMS, HEC-RAS, EPA–SWMM, GeoHMS, and ArcHydro

GIS Tools: ArcGIS, ENVI, and ILWIS

Text Editors: Proficient in Microsoft Office and LATEX

OS: Worked with Windows and Unix

PROFESSIONAL AFFILIATIONS

American Geophysical Union (AGU) **2015 – Present**

American Meteorological Society (AMS) **2015 – Present**

American Society of Civil Engineers (ASCE) **2015 – Present**

ABSTRACT OF THE DISSERTATION

Extreme Precipitation Modeling Using Remotely-Sensed Information and Advanced Statistical Techniques

By

Mohammad Faridzad

Doctor of Philosophy in Civil Engineering

University of California, Irvine, 2019

Distinguished Professor Soroosh Sorooshian, Co-Chair
Professor Kuolin Hsu, Co-Chair

Extreme precipitation models are crucial for understanding the characteristics of extreme weather, ensuring the risk of extreme events, and designing flood protection structures. Analytical relationships that link the risk of extreme precipitation with a specific duration at a given location (i.e. intensity-duration-frequency(IDF) relationships) are commonly used to characterize the extreme events. If homogeneous rainfall data with long records are available, reliable analytical relationships can be developed. Yet, this is often not the case and the gauge networks in many parts of the world are either short or sparse. As a result, uncertainties of the gauge-based analyses tend to be high. To alleviate these uncertainties, regional frequency analysis methods which pool the precipitation data from multiple sites with a homogeneous precipitation pattern are used for modeling extreme precipitations. Yet, defining these homogeneous regions requires making additional assumptions that in many cases are not met.

In this dissertation, I try to address the limitations of the conventional extreme precipitation modeling approaches by: 1) Employing remotely-sensed precipitation information, instead of gauge observations, to capture the spatiotemporal variability of extreme precipitation; and 2) Applying advanced statistical techniques that do not have the limitations of the

conventional regional approaches and can accommodate additional information to enhance model's performance.

In the first part of this dissertation, suitability of remotely-sensed precipitation information for extreme precipitation modeling is explored. A bias-correction framework is introduced to adjust the biases in the satellite-based extreme precipitation estimates. It is shown that the proposed method can effectively reduce the biases in the remotely-sensed extreme rainfall data, especially at high elevation regions where ground-based observations are poor and satellite-based estimates are highly biased. Also, it is demonstrated that the satellite-based extreme precipitation estimates that are bias-adjusted with limited ground-based observations using the proposed method outperform the gauge interpolation estimates even at some densely-gauged regions. Results also demonstrate that the high quantile estimates from the bias-adjusted dataset are in agreement with the Frequency Atlas of the United States(NOAA Atlas 14) estimates across various durations and return periods.

In the next step of this dissertation, advanced statistical techniques are employed to model spatial and temporal characteristics of extreme precipitation from remotely-sensed information. A hierarchical Bayesian approach is used to model extreme precipitation and to generate spatially consistent quantile estimates with low estimation uncertainties. In addition to the Bayesian framework, Max-stable processes, as the generalization of the extreme value theory, are used to capture the marginal properties and tail dependence structure of the extreme precipitation data. The performances of the applied methods in modeling extreme precipitations are evaluated using various validation metrics. A comprehensive evaluation of the models' performances shows that the applied methods are capable of generating extreme return levels that are consistent with gauge-based observations.

Results of this dissertation demonstrate that the satellite-based precipitation information can be used for extreme precipitation modeling, especially at poorly instrumented regions. Also, this study serves as an introduction to the application of advanced statistical techniques for

extreme precipitation modeling using remotely-sensed information. The applied methods resulted in outstanding performances in characterizing extreme precipitation from remotely-sensed information.

Chapter 1

Introduction

Extreme precipitation events have large impacts on societies and can take many lives and may result in considerable financial damages by causing hazards such as floods and landslides. Therefore, probabilities and return levels associated with such events must be considered in floodplain management and designing flood control infrastructure such as dams, dikes, canals, and bridges. Extreme precipitation models are used to model heavy rainfall events and characteristics of extreme rainfalls are often reflected in intensity-duration-frequency (IDF) curves or depth-duration-frequency (DDF) curves. IDF and DDF curves demonstrate probabilities of extreme events with various intensities (or depths) and durations (Mazdiyasni et al., 2019). Extreme events are often defined by their return periods. For instance, an extreme precipitation event with 24-hour duration and a probability of 1% is referred to as a daily 100-year event. Figure 1.1 demonstrates the map of the 100-year extreme precipitation events with 24 hour duration over the United States (Hershfield, 1961). Statistical modeling is used to characterize the relationship between intensity (or depth), duration, and frequency of extreme precipitation events. Typically, certain probability distributions are fitted to the extreme rainfall data with various durations and the return levels associated with each return period are extracted by solving the equation for the inverse distribution. Generalized

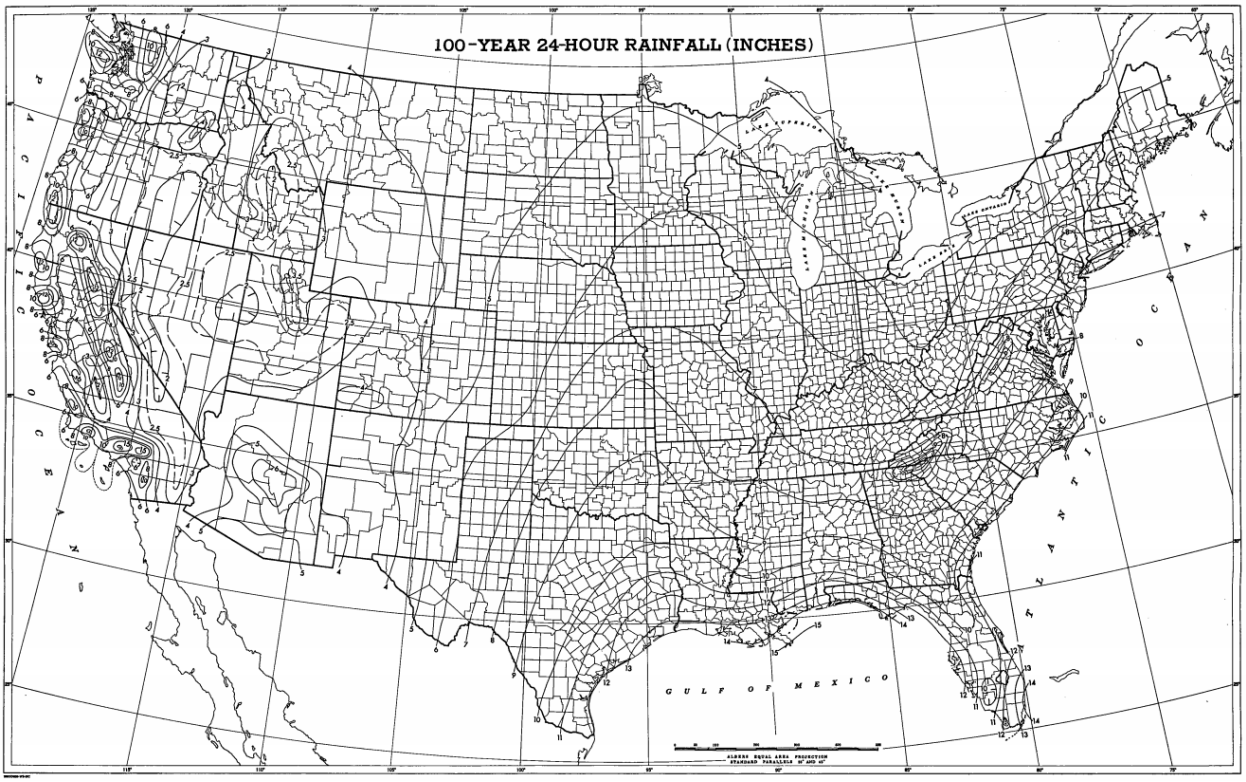

Figure 1.1: Map of rainfall depth(inches) with 24 hour duration and 100 year return period in the United States. Adapted from Hershfield (1961)

Extreme Value (GEV) distribution is commonly used as the limiting distribution for the annual maximum extremes and the Generalized Pareto (GP) distribution is often used for the peak-over-threshold (POT) extremes. Information derived from IDF or DDF curves are used to generate design storms that are further provided as inputs for various engineering designs. Selection of return period for a specific design depends on the importance of the structure under study and design standards.

1.1 The conventional RFA approach

Point measurements by rain gauges are often used to derive statistics of extreme rainfalls at a certain location. Rain gauges provide relatively long, but sparse record of precipitation and are considered as point observations. Given the interest in the extreme rainfall statistics for

larger spatial domains, areal reduction factors (ARF) are used to extend point measurements to larger areas. There is a tendency in environmental applications to analyze all of the data samples from a number of measuring sites rather than using only one sample. This approach is known as regional frequency analysis (RFA). RFA tries to minimize the effects of limited temporal coverage and reduce the uncertainties associated with quantile estimation from individual sites. In RFA approach, the analyzed data samples are measurements of the same variable from a group of sites that are located within a suitably defined region (Hosking and Wallis, 2005). This region is typically referred to as "homogeneous" region which within this region, all of the measuring sites demonstrate identical frequency distributions. In practice, this is not possible and the sites within a region are not exactly identical and the frequency distributions and event magnitudes are different at various sites (Hosking and Wallis, 2005). Delineating homogeneous region was traditionally performed by considering geographical, administrative, and political situation. Nowadays, more advanced techniques such as cluster analysis (Wiltshire, 1986), discordancy measure (Hosking and Wallis, 2005), and region of influence (Burn, 1990) are applied to delineate homogeneous regions.

Various RFA approaches such as the Index-Flood(IF), probability index flood (PIF), and regional shape (RS) methods, have been introduced and applied for numerous hydrological applications. These methods pool the data from a set of sites within a homogeneous region and try to estimate the three parameters of the GEV distribution, namely location, scale, and shape parameters in a regional manner. The main difference between these methods is in the number of distribution parameters estimated regionally. For instance, in the IF method, which is one of the most widely used RFA approaches, the three GEV parameters are estimated regionally (Dalrymple, 1960). Estimating the parameters of the frequency distribution is usually performed by applying the method of linear moments(L-moments) (Hosking and Wallis, 2005). L-moments, similar to probability weighted moments (Greenwood et al., 1979), describe the shape of a probability distribution. Each of the L-moments describe a specific characteristic of a probability distribution. For instance, the first to fifth

L-moments are L-location, L-scale, L-CV, L-skewness, and L-kurtosis and explain mean, scale, coefficient of variation (CV), skewness, and kurtosis of a distribution, respectively.

National Oceanic and Atmospheric Administration (NOAA) Atlas is the source of rainfall frequency estimates for the United States and its territories. NOAA Atlas 14 provides intensity-duration frequency (IDF) and depth-duration-frequency (DDF) curves for different regions based on the regional frequency analysis approach (Bonnin et al., 2006). NOAA Atlas 14 IDF and DDF curves were developed using the best fit among different probability distributions, including the 3-parameter Generalized Extreme Value (GEV), the Generalized Normal, the Generalized Pareto, the Generalized logistic, the Pearson Type III distributions, the 4-parameter Kappa distribution; and the 5-parameter Wakeby distribution. At 80 % of gauges and for sub-daily and daily durations, the GEV gave the best statistics among the 3-parameter distributions and its performance was comparable to that of 4 and 5 parameter distributions. Thus, the GEV was adopted across all gauges and durations (Bonnin et al., 2006). Figure 1.2 shows DDF curves from NOAA Atlas 14 for a location near the campus of the University of California, Irvine.

1.2 Limitations of Conventional RFA Approaches

While the conventional RFA approach is currently the most widely used approach for modeling extreme precipitation, there are certain limitations that tend to undermine its performance in poorly instrumented regions. Based on the steps taken in RFA approach, these limitations can be divided into two main parts. The first limitation is regarding the input precipitation data which is often observations from sparse gauge networks, and the second limitation is the statistical analysis approaches (RFA techniques) often used to characterize extreme rainfalls and to construct IDF or DDF relationships. These two limitations are discussed in the following sections.

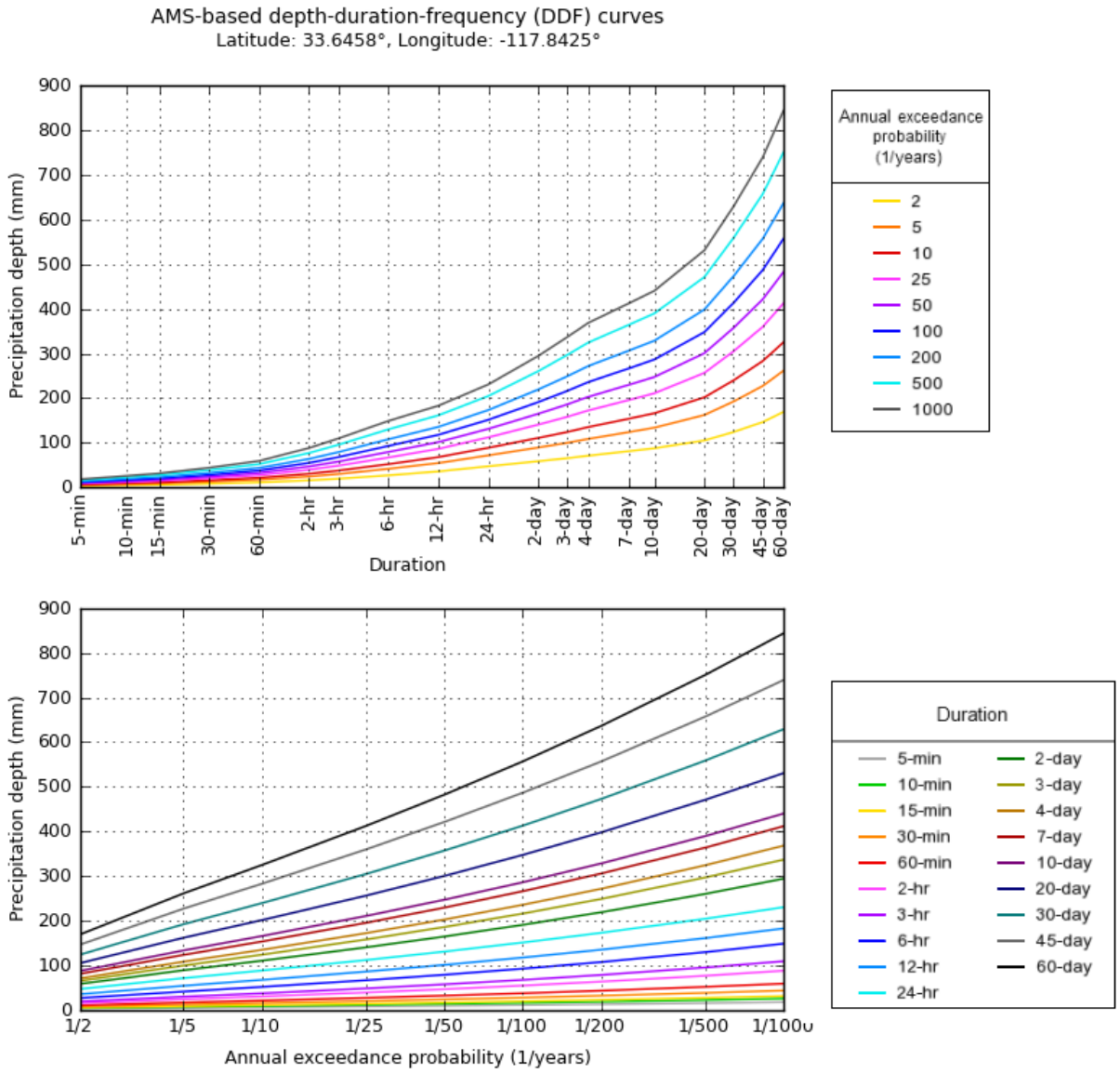

Figure 1.2: Sample Depth-duration-frequency curves for a location in Irvine, California, based on NOAA Atlas 14. Adapted from https://hdsc.nws.noaa.gov/hdsc/pfds/

1.2.1 Deficiencies of Gauge-based Analyses

Rain gauges with long records are the primary source of rainfall information for extreme precipitation modeling. While the United States and parts of Europe have sufficient gauge networks, many parts of the world including developing countries suffer from short and sparsely distributed gauge networks. Figure 1.3 shows the coverage of gauge data organized at Global Precipitation Climatology Centre (GPCC) through Global Precipitation Climatology Project (GPCP, (Adler et al., 2018)) (Kidd et al., 2017). Distance to nearest GPCC gauge in many parts of the world is more than 50 km and in some areas it exceeds 100 km. Extreme precipitation events are substantially variable in space and time and sparse gauge networks cannot represent the spatial and temporal characteristics of these events. Therefore, gauge-based analysis of extremes using sparsely distributed gauge information is prone to considerable uncertainties. Also, it is believed that the maximum intensity of extreme rainfall events will not be captured due to the sparsity of rain gauges and this adds to the uncertainties of gauge-based analyses (Marra et al., 2019).

1.2.2 Methodological Deficiencies

The conventional RFA approaches commonly make various limiting assumptions. For instance, the IF method has the following assumptions: 1) observations at any site are assumed to be identically distributed; 2) observations are also assumed to be serially independent; 3) observations are assumed to be independent at various sites; 4) frequency distributions at different sites are identical apart from a scaling factor; and 5) the regional growth curve is assumed to be correctly specified. While the first two assumptions could be made for various kinds of data, the last three are unlikely for the environmental data (Hosking and Wallis, 2005). Extreme events typically hit areas large enough to affect multiple observation sites and the observations at those sites are likely to be correlated. Also, the last two assumptions

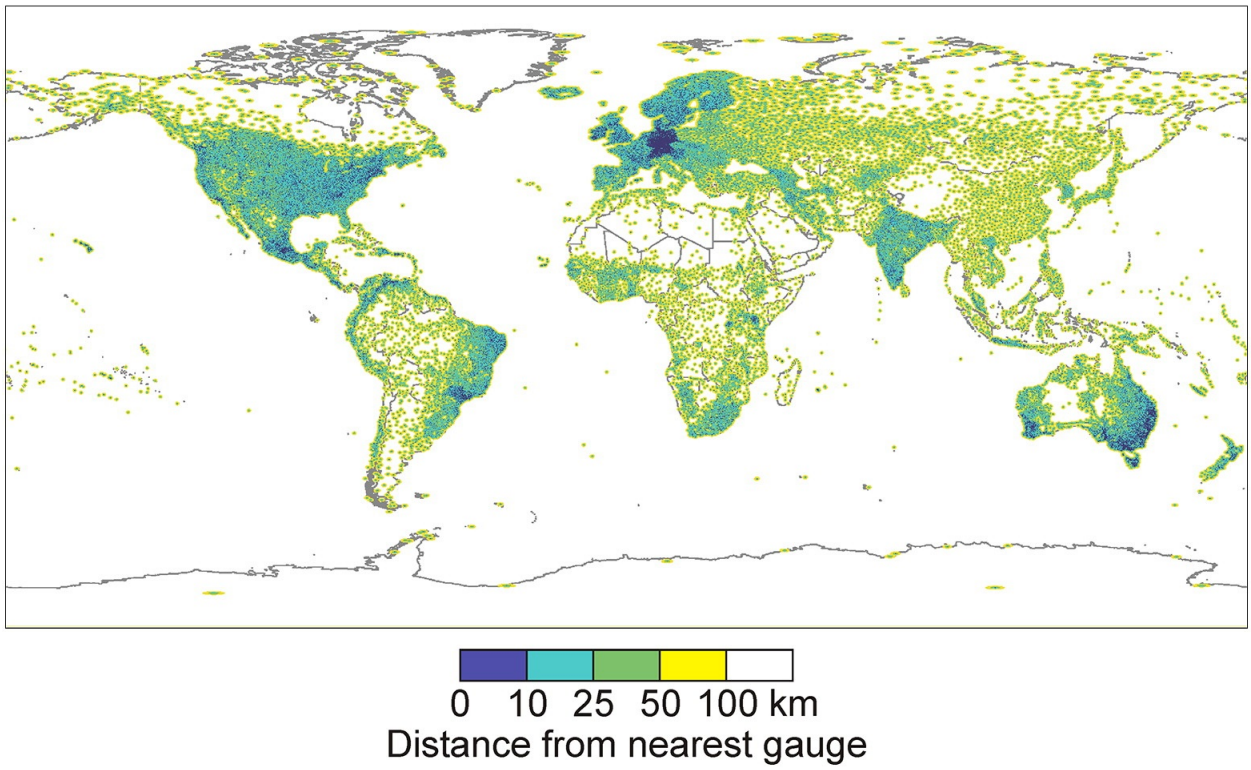

Figure 1.3: Map displaying the distance to the nearest GPCP rain gauge. Adapted from Kidd et al. (2017)

can rarely be fulfilled in environmental applications (Hosking and Wallis, 2005). Furthermore, there are additional limitations in the IF method that tend to limit its application. For instance, delineating homogeneous regions where the scale invariance assumption holds, requires in some instances to shrink the size of the region dramatically. Also, the IF in most cases is defined as the mean or median of the at-site data, which there is no physical explanation for it. These limitations tend to make the uncertainty quantification of IF method challenging (Renard, 2011).

1.3 Potentials for Using Remotely-Sensed Information

In recent years, several efforts have been made to develop DDF curves by employing remotely sensed precipitation information from weather radars and earth observing satellites

(Overeem et al., 2008; Wright et al., 2013; Eldardiry et al., 2015; Marra and Morin, 2015). For instance, Overeem et al. (2009) used an 11-year gauge-adjusted radar-rainfall dataset and performed a regional frequency analysis to extract DDF curves for the Netherlands. They found that radar data, despite being useful for real-time rainfall analysis, still suffer from serious limitations, such as significant errors in extreme rainfall estimates and shortness of data, that limit their usefulness for RFA. Thus, the application of radar data for rainfall frequency analysis is hampered by: (1) its relatively short length of record which leads to sampling issues during distribution fitting process and results in larger uncertainties of the frequency estimates especially for longer durations (Durrans et al., 2002; Eldardiry et al., 2015; Marra et al., 2017b); and, (2) estimation uncertainties and heterogeneities due to the continuous development of radar quantitative precipitation estimation (QPE) instruments and methods (Allen and DeGaetano, 2005; Lombardo et al., 2006). Eldardiry et al. (2015) quantified the effects of each of these sources of uncertainty and attributed much of the quantile estimation uncertainty to the length of the dataset. However, the conditional bias intrinsic to the radar dataset was the main reason for the observed systematic underestimations in the rainfall frequency estimates. As compared to rain gauges and radar network, satellite QPE is able to provide global coverage and has been employed in a number of studies for rainfall frequency analysis (Endreny and Imbeah, 2009; Awadallah et al., 2011; Zhou et al., 2015; Marra et al., 2017b). Yet, similar to radars, the application satellite QPEs for RFA is undermined by the data length issues and estimation uncertainties associated with each of the precipitation estimation products.

Given the relative shortness of the remotely-sensed precipitation datasets, estimating high quantiles which are often needed for engineering design applications is a challenging task. Therefore, a POT approach would be more appropriate than the AMS approach for the RS-based rainfall information. Yet, selecting a threshold for each grid box would a challenge given the need to an automatic threshold selection scheme that could preserve the spatial consistency (Langousis et al., 2016). Most of the studies conducted so far rely on the AMS

approach (Endreny and Imbeah, 2009; Faridzad et al., 2018) and the POT approach has been rarely used (Goudenhoofdt et al., 2017; Demirdjian et al., 2018).

1.3.1 Modeling Extremes Using PERSIANN-CDR

With advances in tools and techniques for precipitation measurement using remotely sensed information, investigation of rainfall characteristics over remote and mountainous regions with limited gauge observations has become possible. In an effort to produce long and consistent climate records based on satellite observations, National Oceanic and Atmospheric Association (NOAA) under the Climate Data Record (CDR) program, in cooperation with the University of California, Irvine, developed a satellite precipitation product named the Precipitation Estimation from Remotely Sensed Information and Artificial Neural Networks-Climate Data Record (PERSIANN-CDR) (Ashouri et al., 2015). PERSIANN-CDR provides near-global (60°N to 60°S latitude and 0° to 360° longitude) precipitation information with 0.25° spatial and daily temporal resolution from 1983 to the present. Given its relatively high spatial resolution and long record, PERSIANN-CDR is a unique dataset for studying extreme precipitations and performing rainfall frequency analysis. The length of the PERSIANN-CDR dataset (35+ years) is particularly valuable for parts of the world that lack the gauge information for rainfall frequency analysis.

Among different remotely sensed precipitation datasets, PERSIANN-CDR is a viable candidate for extreme precipitation analysis given: (1) its high spatial and temporal resolution: when compared with the long-term Global Precipitation Climatology Project (GPCP) (Huffman et al., 1997) product which is monthly and 2.5° by 2.5°, PERSIANN-CDR has a higher temporal (daily) and spatial resolution (0.25° by 0.25°). The 2.5° spatial and monthly temporal resolution is not capable of capturing the spatial and temporal variability of the extreme precipitations especially over regions with complex topographic conditions, and (2) its long

record: PERSIANN-CDR has relatively longer data record (34+ years and continually expanding) in comparison to TRMM 3b42 V7 (Huffman et al., 2007) with 20+ years of data, or CMORPH (Joyce et al., 2004) with 16+ years of record. Based on these strengths, Gado et al. (2017) employed the PERSIANN-CDR dataset to estimate extreme rainfall quantiles at two homogenous regions in the Western United States. They combined information from the PERSIANN-CDR pixels and nearby gauges in a homogenous region and used an innovative regional frequency analysis method to derive quantile estimates at ungauged locations.

1.4 Limitations of Current RS-Based Studies

Currently, there are two main issues that tend to undermine the accuracy of RS-based approaches for extreme precipitation modeling. The first problem is biases in radar and satellite estimates of extreme rainfall events and the second problem is the inefficiency of the applied statistical techniques (Marra et al., 2019). Also, given the continuous development of radar and satellite sensors, as well as, methodological improvements, the RS-based QPEs are sometimes heterogeneous sources of information.

1.4.1 Biases in the Extreme Rainfall Estimates

Radar and satellite-based quantitative precipitation estimates (QPE) are indirect sources of rainfall information and are prone to various sources of uncertainties and estimation biases. These biases tend to become more significant as the extreme events are concerned (Overeem et al., 2009; Eldardiry et al., 2015; Faridzad et al., 2018). Estimation biases are mostly in the form of underestimation of the intensity or depth of extreme events which later translates to the underestimation of the extreme quantiles (Faridzad et al., 2018). Also, estimation uncertainties and random errors are other sources of biases in the RS-based QPEs which

often lead to overestimation of the extreme quantiles (Marra et al., 2018, 2019). Therefore, prior to using the RS-based QPEs for practical frequency analysis purposes, the quality of the dataset in terms of agreement with reliable gauge-based estimates and homogeneity of the records must be assured.

In case of biases in the extreme rainfall estimates by the satellite and radar QPEs, bias-adjustment techniques must be used to have estimates that are consistent with gauge-based observations. Various bias-adjustment techniques have been used in the literature for this purpose (Overeem et al., 2009; Faridzad et al., 2018). The quantile matching method is a standard method often used to match the cumulative distribution function (cdf) of the gridded RS-based QPEs with that of gauge-based observations (Gado et al., 2017).Also, in order to minimize the impact of random errors on the quantile estimation, classical regionalization techniques have been used to pool data from nearby pixels and increase the sample size (Eldardiry et al., 2015; Demirdjian et al., 2018).

1.4.2 Inefficiencies of the Applied Statistical Techniques

Give the relative shortness of most of the RS-based QPEs compared to the quantiles often needed in practice, estimating the high quantiles is a challenging task with large uncertainties. Short precipitation record also gives information on a short part of climatology and extrapolations based on this short range of data is likely to have large biases in high quantiles. Most of the studies performed so far on frequency analysis using gridded precipitation information from RS-based QPEs or numerical weather prediction models, used two general approaches: 1) the at-site method which is using the rainfall time series at each pixel for making inference on the parameters and rainfall frequencies (Faridzad et al., 2018; Ragno et al., 2018); and 2) pooling rainfall information from a group of nearby pixels (Eldardiry et al., 2015) or applying the classic regionalization approaches (Overeem et al., 2009; En-

dreny and Imbeah, 2009; Gado et al., 2017). While the at-site method has the uncertainty issues related to the shortness of record, the pooling-based approaches also come with the limiting assumptions underlying the RFA methods and these assumptions are often hard to be fulfilled when using extreme precipitation data. Stochastic storm transposition is also another method used to reduce the biases in the parameter estimation procedure (Wright et al., 2013, 2017).

1.5 Research Motivations and Approaches

The primary motivation of this research is to address the limitations of the gauge-based rainfall frequency analyses in poorly instrumented regions. The limited gauge observations in remote areas and high elevation regions cannot demonstrate the spatial and temporal variability of extreme events that are highly variable in space and time. Therefore, the extreme rainfall models based on the limited gauge information are highly uncertain and not reliable. Also, the conventional statistical tools applied for extreme precipitation modeling have certain limitations that tend to undermine their effectiveness, especially in poorly gauged regions. Additionally, we aim to construct models that can generate spatially consistent return level maps. Such maps are useful in designing hydraulic and hydrologic infrastructures, in mapping hazards, and performing risk assessment. Specifically, precipitation return level maps are provided to the hydrologic and hydraulic models to map the flood hazards at large catchments. This is of paramount importance for the regions that have complex topographies where a single IDF curve for a specific location cannot represent the extreme precipitation characteristics in those regions. Knowledge on the spatial distribution and magnitude of extreme events is also important in land-use development for identifying the regions that are most prone to intense hydrological events. Subsequently, the overarching objective of this research is to introduce frameworks by which remotely-sensed precipitation

information could be reliably used for extreme precipitation modeling and developing IDF or DDF curves for regions with limited gauge observations. A systematic approach is taken to accomplish this objective in a step-wise manner. The main objectives and approaches of this dissertation are as follows:

- **Objective 1:**

  The first objective of this dissertation is to investigate the suitability of remotely-sensed precipitation information for extreme precipitation modeling and generating DDF curves. To accomplish this objective and to justify the use of remotely-sensed information, comparisons with gauge-based observations at densely gauged regions are made. For this purpose, PERSIANN-CDR dataset which is one of the longest satellite-based precipitation datasets and has high spatial and temporal resolutions is used.

- **Approach 1:**

  My approach to this objective is to perform an extensive evaluation of the extreme rainfall estimates from remotely-sensed information. As it is the case for the RS-based QPEs, there are biases in the extreme precipitation estimates that need to be adjusted prior to using these datasets. A bias-adjustment approach is introduced and its performance is verified with respect to the gauge-based observations. Also, the bias-adjusted extreme precipitation estimates are evaluated with respect to the gauge-based observations. Then, the bias-adjusted extreme precipitation estimates for various durations are used to construct DDF curves. For this purpose, GEV distribution is fitted to the pixel-wise information from the satellite-based observations. Finally, the goal is to show that the bias-adjusted satellite-based dataset is capable of producing consistent frequency estimates with gauges-based analyses with much longer records at some well-sampled watersheds in the United States.

- **Objective 2:**

  The second objective of this dissertation, is to construct a model that can capture the

marginal distribution of extreme precipitation data from satellite pixels and generate frequency estimates with low uncertainties while accounting for the spatial structure of the data. As opposed to the previous objective which involved modeling marginal distribution of the data using pixel-wise information, here we take into account neighborhood information to generate spatially consistent return levels with lower uncertainties. The goal is to apply newly developed statistical techniques that do not have the limitations of the conventional regional frequency analysis approaches and can make marginal extrapolations with lower uncertainties.

- **Approach 2:**

  The approach for this objective is apply a hierarchical Bayesian approach. The applied approach can generate spatially consistent return level estimates, while reducing the estimation uncertainties by bringing information from neighboring sites. This approach has a few advantages compared to the RFA approach. It allows to provide expert knowledge to the model through the use of priors. Besides, additional physical and geographical information can be provided to the model to enhance parameter estimation. Also, unlike the common ad-hoc uncertainty assessment techniques (e.g. bootstrapping technique), this approach offers an explicit way of accounting for the uncertainties in the model parameters and quantile estimates. The proposed approach is applied to model extreme precipitation in Washington state. The precipitation data used in this part is the bias-adjusted extreme precipitation information from PERSIANN-CDR dataset using the method proposed for objective 1.

- **Objective 3:**

  The third objective of this dissertation, is to model the spatial dependence in extreme precipitation data in a consistent way with the extreme value theory. The goal is to apply methodologies that beside modeling the marginal properties of the extreme precipitation information from the gridded rainfall data, can model the spatial de-

pendence structure of extremes by simulating the residual dependence in the data. Modeling dependence structure of extreme precipitation is important when studying the joint probabilities of extreme events at multiple locations.

- **Approach 3:**

  The modeling approach that is best suited for this objective is Max-stable process. Max-stable processes are generalization of the extreme value theory to infinite dimensional scale. Max-stable processes can model the tail dependence structure of the extreme precipitation data, after capturing the marginal properties. Various types of max-stable processes are applied and their performances are evaluated in terms of modeling marginal properties and tail dependence structure of the extreme rainfall data. The precipitation data used in this part is the bias-adjusted extreme precipitation information from PERSIANN-CDR dataset using the method proposed for objective 1. Finally, the quantile estimates from the outperforming model fed with the RS-based data is validated against an extensive number point observations from ground-based rain gauges. The proposed approach is applied to model extreme precipitation in the Pacific Northwest United States.

1.6 Scope of the Dissertation

The rest of this dissertation is organized as follows: Chapter 2 presents the bias-correction framework proposed for adjusting the RS-based precipitation estimates from PERSIANN-CDR dataset. Application of this framework for precipitation frequency analysis across the United States is also explored in this chapter. Chapter 3 presents the application of hierarchical Bayesian framework for extreme precipitation modeling using satellite-based precipitation estimates from PERSIANN-CDR dataset. The latent variable model is used in this chapter for modeling extreme rainfalls and Washington state is selected as the study

area. Chapter 4 demonstrates the application of Max-stable processes for modeling extreme precipitation from remotely-sensed information. Various parametric max-stable models are applied in this chapter to model extreme precipitation over the Pacific Northwest region of the United States. Finally, chapter 5 summarizes the findings of this dissertation, limitations, and the directions for future research in this area.

Chapter 2

Rainfall Frequency Analysis for Ungauged Regions Using Remotely Sensed Precipitation Information

2.1 Introduction

Rainfall Frequency Analysis (RFA) is an important tool in hydrologic engineering (Stedinger, 1993; Hosking and Wallis, 2005; Bonnin et al., 2006). Depth-Duration-Frequency (DDF) curves, which link extreme rainfall depths to their probability of occurrence, are based on time series of extreme rainfall with different durations fitted with probability distribution functions. RFA has been traditionally performed using information from rain gauges. This approach has proven to be a useful tool in planning and design for regions where observational data is relatively abundant such as the United States or Europe. However, many parts of the world, particularly the developing countries, do not have that advantage. In many developing countries, gauge observation networks over remote and mountainous regions are still sparse

and limited in terms of duration.

With advances in tools and techniques for precipitation measurement using remotely sensed information, investigation of rainfall characteristics over remote and mountainous regions with limited gauge observations has become possible. In an effort to produce long and consistent climate records based on satellite observations, National Oceanic and Atmospheric Association (NOAA) under the Climate Data Record (CDR) program, in cooperation with the University of California, Irvine, developed a satellite precipitation product named the Precipitation Estimation from Remotely Sensed Information and Artificial Neural Networks-Climate Data Record (PERSIANN-CDR) (Ashouri et al., 2015). PERSIANN-CDR provides near-global (60°N to 60°S latitude and 0° to 360° longitude) precipitation information with 0.25° spatial and daily temporal resolution from 1983 to the present. Given its relatively high spatial resolution and long record, PERSIANN-CDR is a unique dataset for studying extreme precipitations and performing rainfall frequency analysis. The length of the PERSIANN-CDR dataset (35+ years) is particularly valuable for parts of the world that lack the gauge information for rainfall frequency analysis.

In recent years, several efforts have been made to develop DDF curves by employing remotely sensed precipitation information from weather radars and earth observing satellites (Overeem et al., 2008; Wright et al., 2013; Eldardiry et al., 2015; Marra and Morin, 2015). For instance, Overeem et al. (2009) used an 11-year gauge-adjusted radar-rainfall dataset and performed a regional frequency analysis to extract DDF curves for the Netherlands. They found that radar data, despite being useful for real-time rainfall analysis, still suffer from serious limitations, such as significant errors in extreme rainfall estimates and shortness of data, that limit their usefulness for RFA. Thus, the application of radar data for rainfall frequency analysis is hampered by: (1) its relatively short length of record which leads to sampling issues during distribution fitting process and results in larger uncertainties of the frequency estimates especially for longer durations (Durrans et al., 2002; Eldardiry et al.,

2015; Marra et al., 2017b); and, (2) estimation uncertainties and heterogeneities due to the continuous development of radar quantitative precipitation estimation (QPE) instruments and methods (Allen and DeGaetano, 2005; Lombardo et al., 2006). Eldardiry et al. (2015) quantified the effects of each of these sources of uncertainty and attributed much of the quantile estimation uncertainty to the length of the dataset. However, the conditional bias intrinsic to the radar dataset was the main reason for the observed systematic underestimations in the rainfall frequency estimates. As compared to rain gauges and radar network, satellite QPE is able to provide global coverage and has been employed in a number of studies for rainfall frequency analysis (Endreny and Imbeah, 2009; Awadallah et al., 2011; Zhou et al., 2015; Marra et al., 2017b). Yet, similar to radars, the application satellite QPEs for RFA is undermined by the data length issues and estimation uncertainties associated with each of the precipitation estimation products.

Among different remotely sensed precipitation datasets, PERSIANN-CDR is a viable candidate for extreme precipitation analysis given: (1) its high spatial and temporal resolution: when compared with the long-term Global Precipitation Climatology Project (GPCP) (Huffman et al., 1997) product which is monthly and 2.5° by 2.5°, PERSIANN-CDR has a higher temporal (daily) and spatial resolution (0.25° by 0.25°). The 2.5° spatial and monthly temporal resolution is not capable of capturing the spatial and temporal variability of the extreme precipitations especially over regions with complex topographic conditions, and (2) its long record: PERSIANN-CDR has relatively longer data record (34+ years and continually expanding) in comparison to TRMM 3b42 V7 (Huffman et al., 2007) with 20+ years of data, or CMORPH (Joyce et al., 2004) with 16+ years of record. Based on these strengths, Gado et al. (2017) employed the PERSIANN-CDR dataset to estimate extreme rainfall quantiles at two homogenous regions in the Western United States. They combined information from the PERSIANN-CDR pixels and nearby gauges in a homogenous region and used an innovative regional frequency analysis method to derive quantile estimates at ungauged locations.

The primary goal of this chapter is to evaluate the feasibility of using the PERSIANN-CDR dataset for rainfall frequency analysis by constructing the required DDF curves over regions with limited gauge information or mountainous areas. As a proof of concept, this study has been conducted over the United States, where longer gauge observations with sufficient spatial coverage exist. As some studies have reported, there are biases in the PERSIANN-CDR estimates which necessitate the application of bias-adjustment techniques to improve the accuracy of the PERSIANN-CDR estimates of extreme precipitations (Miao et al., 2015; Duan et al., 2016; Shah and Mishra, 2016; Yang et al., 2016; Liu et al., 2017). This study was designed with the following objectives: (1) to propose an elevation-based bias correction model applicable to the PERSIANN-CDR dataset and test over a large number of river basins in the continental United States, and, (2) to demonstrate the usefulness of satellite-based precipitation data in rainfall frequency analysis and use the derived frequency estimates to further verify the effectiveness of the proposed bias-correction model. In the proposed frequency analysis framework, only the PERSIANN-CDR information is used to estimate extreme precipitation quantiles and no information from nearby gauges is incorporated in the development of DDF curves (Gado et al., 2017).

The rest of this chapter is organized as follows: in section 2, a detailed description of gauge and PERSIANN-CDR datasets used in the study is presented, followed by the specifications of the studied basins. The bias-adjustment approach, cross-validation techniques and the frequency analysis procedures pursued in the study are introduced in section 3. Section 4 presents the results and discussion. The main findings and conclusions are summarized in Section 5.

2.2 Data

2.2.1 Gauge Data

Global Historical Climatology Network (GHCN)-Daily is a quality controlled dataset that is used in this study. This dataset contains comprehensive information of daily summaries of more than 40 meteorological variables, including precipitation, temperature, snow depth, wind information, evaporation, etc. recorded by 100,000 land surface stations operated by 20 agencies around the world.

In this chapter, I select 20 basins located in the Eastern and Western United States (Figure 2.1). The daily rainfall data from rain gauges with 34+ years of observation (1/1/1983-12/31/2015) were downloaded from National Oceanic and Atmospheric Association-National Climatic Data Center (NOAA-NCDC) database (https://www.ncdc.noaa.gov/ghcnd-data-access). A brief description of the selected basins with their hydrologic unit codes (HUC) and the number of gauges with 34+ years of data selected for this study are presented in Table 2.1. The selected basins incorporate a wide range of elevations, from 0 to 3700 m mean sea level, and diverse climatic conditions.

2.2.2 PERSIANN-CDR data

PERSIANN-CDR is a retrospective multi-satellite precipitation dataset that provides near-global precipitation information, 60°N-60°S latitude and 0°-360° longitude, at 0.25° spatial resolution (around 25 km) and daily temporal resolution from 1 January 1983 to near present (Ashouri et al., 2015). The PERSIANN-CDR dataset was developed by the following steps. In the first step, the PERSIANN algorithm (Hsu et al., 1997) is implemented on the archive of Gridded Satellite (GridSat-B1) Infrared Data (Knapp et al., 2011) from Geostationary

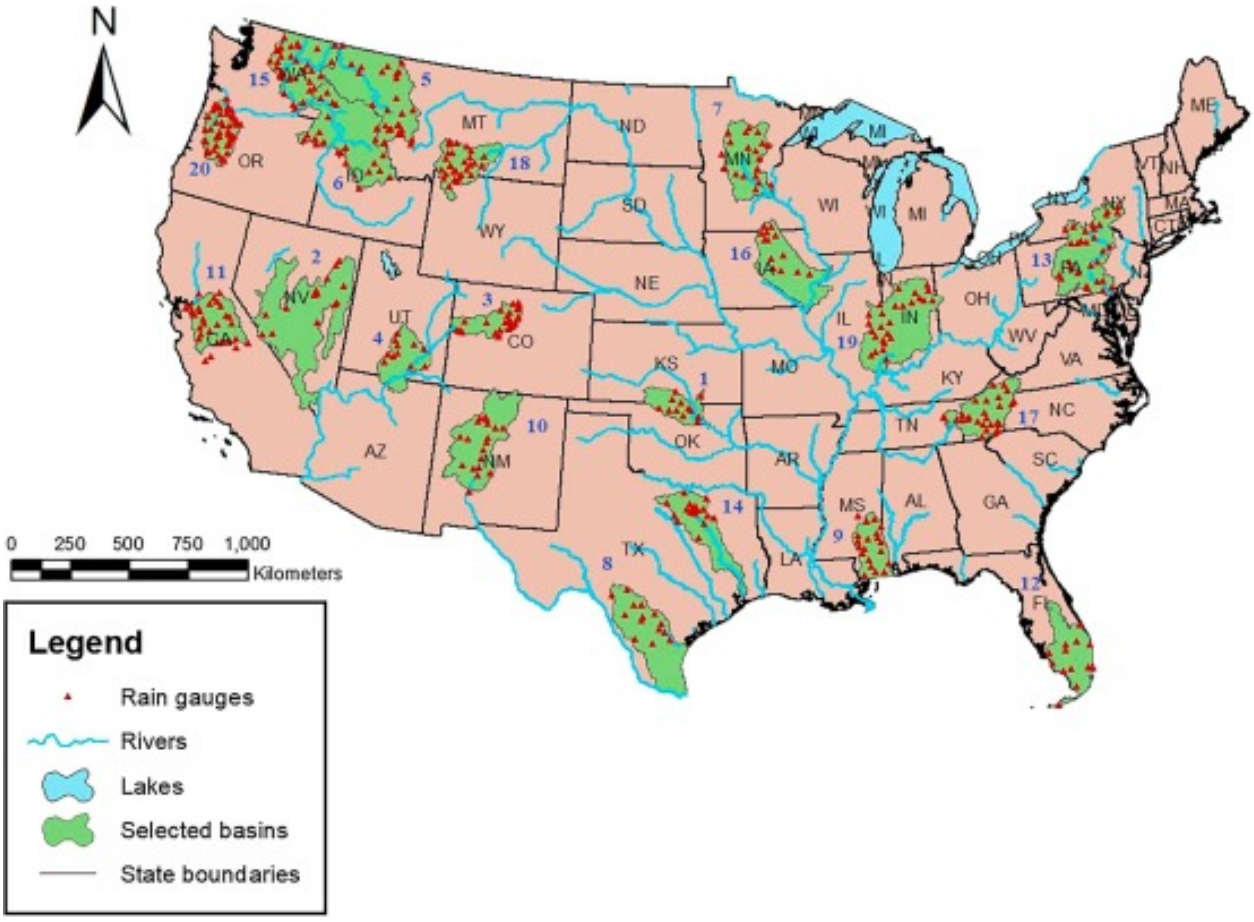

Figure 2.1: The geographic location of the selected basins and gauges

Earth Orbiting satellites (GEOs). The model is pre-trained using the National Center for Environmental Prediction (NCEP) Stage IV hourly precipitation data. Then the parameters of the model are kept fixed, and the model is run on the entire historical records of GridSat-B1 to estimate the historical precipitation at 3-hourly resolution. In the next step, the estimated rain-rates are resampled to 2.5° spatial resolution and bias-adjusted with GPCP product v2.2 (Adler et al., 2003) to keep it consistent with the GPCP monthly product. Finally, the PERSIANN-CDR dataset is obtained by accumulating the 3-hourly bias adjusted data. In this research, daily PERSIANN-CDR data for the selected basins for the time period of 1/1/1983 to 12/31/2015 was used.

Table 2.1: Summary of the features of the selected basins and gauges

Basin No.	Basin Name	HUC	State(s)	Area (sq. mi.)	No. of gauges	Gauge elevations (m)			KÃ¶ppen-Geiger climate class	Climate Description
						Min	Max	Mean		
1	Arkansas-Keystone	1106	KS, OK	9750	12	253	454.2	347.7	Dfa, Cfa	Continental, temperate
2	Central Nevada Desert	1606	NV	47100	14	1299.1	2448.5	1818.6	BSk, BWk, BWh, Dfb	Dry, continental
3	Colorado Headwaters	1401	CO	9730	25	1450.8	3474.7	2646.2	BSk, Dfb, Dfc	Dry, continental
4	Dirty Devil	1407	UT, AZ	13500	11	1164.9	2987	2093.1	BSk,Bwk, Dfb	Dry, continental
5	Kootenai-Pend Oreille-Spokane	1701	MT, ID, WA	36600	30	548.6	2514.6	1691.5	Dsb, Dfb	Continental
6	Lower Snake	1706	ID, WA, OR	11800	23	328	2788.9	1523.3	Dfb, Dsb	Continental
7	Mississippi Headwaters	701	MN	20200	19	278	454.2	372.2	Dfb	Continental
8	Nueces-Southwestern Texas Coastal	1211	TX	29000	15	43	625.4	217.8	Cfa	Temperate
9	Pascagoula	317	MS	12100	20	2.4	164.9	72.3	Cfa	Temperate
10	Rio Grande - Elephant Butte	1302	NM	26900	19	1378.9	2621.3	1843.8	Dfb, BSk	Continental, dry
11	San Joaquin	1804	CA	15600	30	3.7	2920	537.2	Csa, BSk	Temperate, dry
12	Southern Florida	309	FL	18700	14	0.9	10.7	4.3	Cfa, Aw	Temperate, tropical
13	Susquehanna	205	PA, NY, MD	27200	30	78.9	566.9	313.5	Dfa, Dfb	Continental
14	Trinity	1203	TX	18000	24	103.9	339.9	208.7	Cfa	Temperate
15	Upper Columbia	1702	WA	22600	32	113.1	1978.2	689.3	Dfb, Dsb, BSk	Continental, dry
16	Upper Mississippi-Iowa	708	IA, IL, MN	22800	25	195.1	390.1	319	Dfa, Dfb	Continental
17	Upper Tennessee	601	TN, NC, GA,VA	17200	28	230.1	1143.9	555.5	Cfa	Temperate
18	Upper Yellowstone	1007	MT, WY	14400	30	944.3	2865.1	1906.2	Dfb, Dfc, BSk	Continental, dry
19	Wabash	512	IN,IL, OH	32600	26	134.7	284.1	202.2	Dfa	Continental
20	Willamette	1709	OR	11400	46	6.4	1554.5	434.7	Csb, Dsb, Dsc	Temperate, continental

2.3 Methodology

2.3.1 Model Description

In the proposed bias correction model, I first correct the PERSIANN-CDR estimates of Annual Maxima with gauge data at pixels with available gauge records for the study period. The time series of annual maximum precipitation from both gauge network and PERSIANN-CDR for the corresponding pixels are extracted and sorted in an ascending order. For simplicity, I denote the gauge-based annual maximum series as "GM", and the PERSIANN-CDR annual maximum series as "PM" hereafter. A zero-intercept regression line is fitted to the scatterplot of GM and PM time series, with the corresponding PM values in the Y-axis and GM values in the X-axis (Figure 2.2a). The slope of this regression line (called "Correction Factor" or CF hereafter) shows the deviation of PM with respect to ground truth (GM), and it indicates the level of correction required for correcting PM to GM. A CF value larger than one indicates an overestimation of the extreme precipitation by PERSIANN-CDR, and a CF smaller than one implies the underestimation. The larger the deviation of a CF value from the one to one case, the greater the correction required for the PM (Figure 2.2a).

To investigate the orographic characteristics of bias at each basin, the CF values at individual gauges are plotted against the corresponding gauge elevations (Figure 2.2b). The basin-scale plots are further merged to provide a more comprehensive view of the CF-elevation relationship (Figure 2.2c). Following the approach mentioned above, an exponential function is fitted to the derived CF-elevation relationship at both individual basin and multi-basins scale as shown in Figure 2.2c. I construct a correction function based on the CF-elevation relationship derived from 4 Western US basins and test its performance with different cross-validation and validation methods on other basins. The selected basins are San Joaquin River Basin (California), the Willamette River Basin (Oregon), the Upper Columbia River Basin

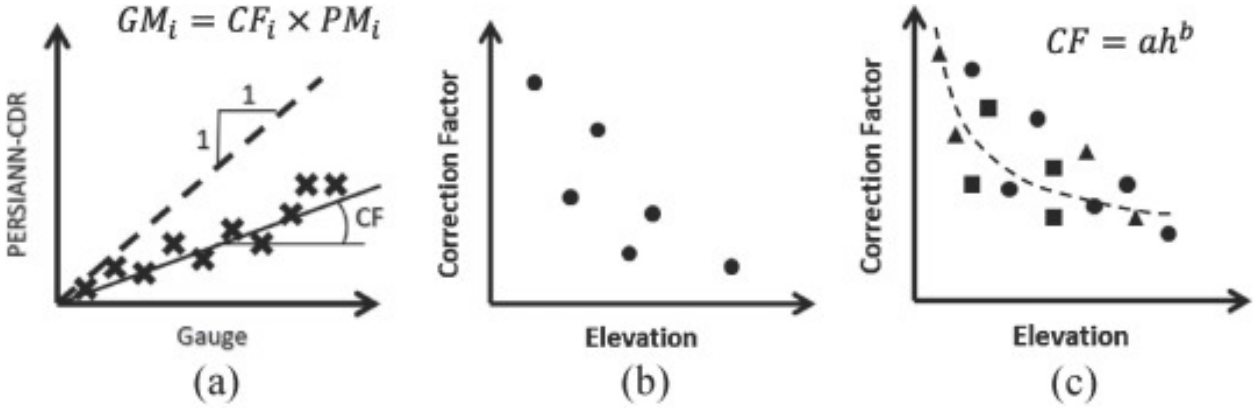

Figure 2.2: Figure 2. Schematic view of the bias adjustment approach. (a) Estimation of correction factor at a single gauge with annual maximum series (AMS) of gauge and collocated PERSIANN-CDR pixel (b) Correction factor - elevation relationship at single basin scale (each point showing the CF for at a gauge) (c) Correction factor-elevation relationship for multiple basins and the schematic of the fitted exponential function (similar markers showing gauges from the same basin)

(Washington) and the Colorado Headwaters (Colorado). These basins are selected since they provided bias-elevation information at different elevations and encompassed different climatic conditions, which are representative for building a robust and effective bias correction model applicable to other river bases in the United States. Finally, the correction model based on these four selected river basins is tested on the other 16 basins with different elevation ranges and climatic conditions in the Western and Eastern U.S.

2.3.2 Hold-out Cross-Validation

Hold-out cross-validation is implemented to examine how the performance of the correction model is influenced by the number of basins incorporated in the model calibration, and to investigate whether incorporating information from fewer basins could improve the CDR estimates of AMS. The four basins used for training the correction function are divided into two groups. The basins are grouped in a way that information from different elevations and climates are included for each case. A correction function based on the gauge and the PERSIANN-CDR information from the basins in the first group is used to adjust the PM

for the basins of the other group, and vice versa. In other words, an exponential regression function is fitted to the CF-elevation relationship from the two basins in the first group and is then used to adjust the AMS from the PERSIANN-CDR dataset for the basins in the second. The effectiveness of the bias-correction functions is assessed using the root mean squared error (RMSE) of the sorted AMS from the adjusted CDR and that of gauge observations, at each of the gauge locations and basins.

2.3.3 Comparison with Gauge Interpolation

Besides comparing the original and corrected PERSIANN-CDR using the approaches mentioned above, I also include a commonly used basin-scale interpolation method for analyzing extreme precipitation over remote and mountainous areas where the gauge network is insufficient or even non-existent (Chen et al., 2008; Doumounia et al., 2014).

2.3.4 Leave-One-Out Cross-Validation

Precipitation intensity at an ungauged location is commonly estimated by interpolating observations from nearby gauges. Performance of the bias-adjusted PERSIANN-CDR dataset in estimating the annual maximum time series at an ungauged location is compared with the estimates from the interpolation method and the original PERSIANN-CDR dataset. At each of the calibration basins, I leave one gauge out of the training phase, and the entire time series of precipitation at this particular gauge location is constructed with the linear interpolation of observations from the remaining gauges. Then, the annual maximum series at the location of the held out gauge is extracted from the interpolated time series. The CF-elevation relationship for the selected calibration basins is derived, and the CF corresponding to the elevation of the removed gauge is used to correct the PM time series at the PERSIANN-CDR pixel over the left-out gauge location. Finally, the interpolation-based

annual maximum time series and the corrected PM are compared with the original GM. RMSE is used as the measure of the difference between the calculated time series and the GM. It is worth mentioning that I repeat this procedure for all the gauges at each calibration basin to investigate the robustness of our proposed correction method.

2.3.5 K-fold Cross-Validation

The leave-one-out cross-validation approach described in section 3.3 evaluates the performance of the suggested bias-correction approach at a single gauge level. When there is a dense gauge network in a basin, interpolation of available gauge observations may result in better estimates of the AMS at an ungauged site. However, the gauge interpolated estimates could be less reliable when the region has limited or sparse gauge observations. Therefore, to find the breaking point where the corrected PERSIAN-CDR dataset starts to outperform the interpolation-based results, I carry out the k-fold cross-validation. At each of the four basins used in the calibration process, different percentages (i.e., 10, 20, 30, 40, 50, 60, 70, and 80%) of gauges are randomly selected and left out. Then, the entire time series of precipitation for the locations of the removed gauges are constructed using the linear interpolation of the daily observations from the remaining gauges. The annual maximum series for the locations of the removed gauges are then extracted from the interpolated time series. Finally, I compare the corrected PM and the interpolation-based annual maximum time series at each gauge location with the GM for that location. Since various combinations of gauges could be selected as test samples, results depend on the distribution of the remaining gauges and the distances between the held out and nearby gauges. To reduce the sensitivity of the results to the selection of gauges, I carry out 30 random selections of the hold-out gauges and consider each selection an independent test. RMSE of the interpolation-based AMS is then compared with RMSE of the corrected PM for the selected gauges in each independent run. The average RMSE of the 30 independent runs is also calculated to have the overall

error estimate for different hold-out scenarios (i.e. 10, 20, 30, 40, 50, 60, 70, and 80% of gauges being held out).

2.3.6 Satellite-based Rainfall Frequency Analysis

National Oceanic and Atmospheric Administration (NOAA) Atlas 14 is a source of rainfall frequency estimates for the United States and its territories. NOAA Atlas 14 provides intensity-duration-frequency (IDF) and depth-duration-frequency (DDF) curves for different regions based on the regional frequency analysis approach (Bonnin et al., 2006). NOAA Atlas 14 IDF and DDF curves were developed using the best fit among different probability distributions, including the 3-parameter Generalized Extreme Value (GEV), the Generalized Normal, the Generalized Pareto, the Generalized logistic, the Pearson Type III distributions, the 4-parameter Kappa distribution; and the 5-parameter Wakeby distribution. At 80% of gauges and for sub-daily and daily durations, the GEV gave the best statistics among the 3-parameter distributions and its performance was comparable to that of 4 and 5 parameter distributions. Thus, the GEV was adopted across all gauges and durations (Bonnin et al., 2006). The GEV distribution was firstly introduced by Jenkinson (1955), and it has been widely used for frequency analysis of extreme precipitation and was demonstrated superior over other probability distribution functions in terms of fitting the annual maxima time series (AMS) (Ben-Zvi, 2009; Bougadis and Adamowski, 2006; Fowler and Kilsby, 2003; Gellens, 2002; Norbiato et al., 2007; Villarini et al., 2011). The GEV distribution is a 3-parameter probability distribution that combines three extreme value distributions. The type of the distribution is characterized by the value of the shape parameter ξ. Negative, zero, and positive values of the shape parameter determines the tail behavior of the distribution as short-tailed (Weibull), light-tailed (Gumbel) and heavy-tailed (Fréchet), respectively. The

GEV cumulative distribution function is given by:

$$F(x) = \exp\left\{-\exp\left[-\frac{x-\mu}{\sigma}\right]^{-\frac{1}{\xi}}\right\} \qquad \text{for } \xi \neq 0 \tag{2.1}$$

$$F(x) = \exp\left\{-\left[1+\xi\frac{x-\mu}{\sigma}\right]\right\} \qquad \text{for } \xi = 0 \tag{2.2}$$

where ξ, μ, and σ are the shape, location, and scale parameters, respectively.

To fit the GEV distribution with the PERSIANN-CDR daily precipitation, I first adjust the data samples, in which the block maximum series of PERSIANN-CDR for 2-day, 3-day, 4-day, 7-day, 10-day, 20-day, 30-day, 45-day and 60-day durations are corrected with gauge data using the same approach used for daily precipitation.

The GEV distribution is fitted to the annual maxima series of corrected CDR for different durations using gevfit function from the Matlab Statistics and Machine Learning Toolbox (https://www.mathworks.com/help/stats/gevfit.html). Maximum likelihood estimation is used to estimate the parameters of the GEV distribution and the corresponding confidence intervals (Kotz and Nadarajah, 2000; Embrechts et al., 2013). The return level for each return period and duration is estimated using the inverse GEV function as in equations 2.3 and 2.4:

$$X_T = \mu - \frac{\sigma}{\xi}\left\{1-\left[-ln\left(1-\frac{1}{T}\right)\right]\right\} \qquad \text{for } \xi \neq 0 \tag{2.3}$$

$$X_T = \mu - \sigma ln\left[-ln\left(1-\frac{1}{T}\right)\right] \qquad \text{for } \xi = 0 \tag{2.4}$$

where X_T is the return level (i.e., the rainfall depth that on average is exceeded once in T years), and $T = 1/(1-F)$ is the return period. Using the return levels at different return periods and annual exceedance probabilities, the DDF curves are generated. NOAA Atlas 14 (Bonnin et al., 2006) provides DDF curves with sub-daily, daily and multi-day durations. The DDFs can be downloaded from the NOAA precipitation frequency data server (https://hdsc.nws.noaa.gov/hdsc/pfds/). Since the PERSIANN-CDR dataset gives precipitation estimates at daily time scale, the daily and multi-day durations were considered in generating the DDF curves. To remain consistent with NOAA frequency estimates, precipitation durations considered in this study are 1-day, 2-day, 3-day, 4-day, 7-day, 10-day, 20-day, 30-day, 45-day, and 60-day. It should be noted that the durations considered here do not mean precipitation occurred during the entire period, but the sliding window gives the highest value of precipitation accumulation over the selected period. Lastly, I compare the return levels based on the corrected CDR estimates with that of NOAA Atlas 14 at each duration and return period.

2.3.7 Uncertainty assessment

The confidence intervals of the return levels from the original and the adjusted PERSIANN-CDR datasets are estimated using a bootstrapping technique. I generate 1000 random samples with replacements from the original and adjust AMS at the target gauge locations. Then, the Maximum Likelihood estimation is used to calculate the parameters of the GEV distributions fitted to each of these random samples. Return levels for different durations are calculated using the inverse GEV function evaluated at different return periods. Finally,

the 5th and 95th percentiles of the bootstrapped return levels at each duration and return period are taken as the 90 percent confidence intervals.

2.4 Results and Discussion

2.4.1 Training Basins

Figure 3 shows the scatterplots of the CDR and gauge AMS and the regression line equation at a number of gauges in the Willamette River Basin in the state of Oregon. In some of the gauge locations (Figures 2.3a-d, and g-i), the original PERSIANN-CDR has a certain degree of underestimation or overestimation, while in some other gauge locations the PERSIANN-CDR estimates are in good agreement with gauge observations (Figures 2.3e and 2.3f).

An important note here is that a PERSIANN-CDR pixel has an area about 625 km2 which is much larger than the sampling area of a rain gauge. The value of a PERSIANN-CDR pixel represents the average precipitation within that pixel's spatial domain. In fact, even if the PERSIANN-CDR estimate at a pixel is completely accurate, its value tends to be smaller than the sub-pixel point measurements. In other words, by comparing a PERSIANN-CDR pixel with a point measurement, we are carrying out a "point-area" comparison. Therefore, by adjusting the PERSIANN-CDR pixels with point measurements, we are down-scaling PERSIANN-CDR to point resolution. This implies that the adjusted dataset should be regarded as a point estimate, rather than an area estimate. Furthermore, there would be time discrepancies between the PERSIANN-CDR's daily interval, and the gauges' 24-hour intervals. Thus, the correction factor accounts for the influence of both "point-area" and time discrepancy issues.

At each of the four basins selected to build the correction model (i.e., the San Joaquin River

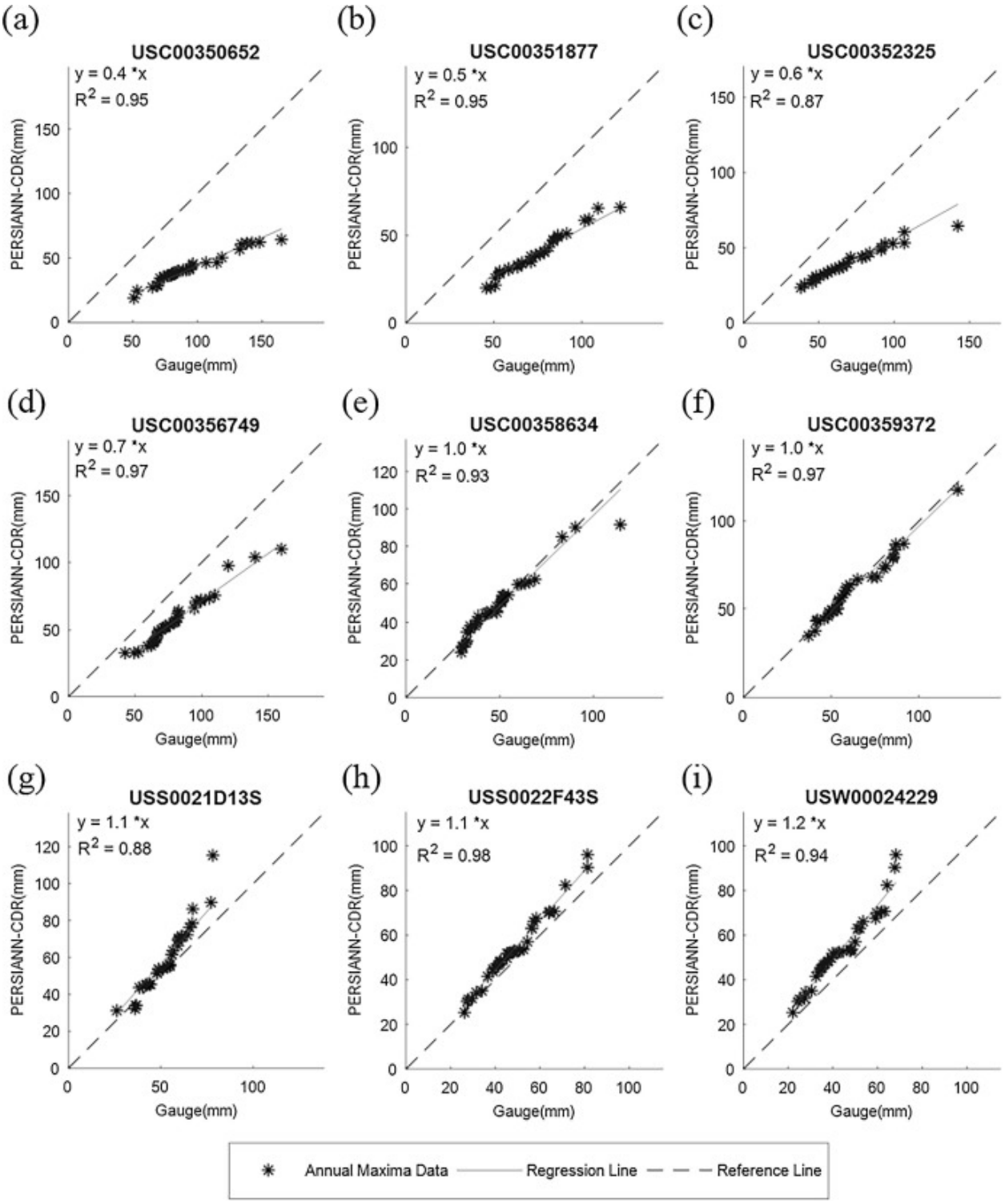

Figure 2.3: Scatterplots of gauge and PERSIANN-CDR AMS and the zero intercept regression lines at sample gauge locations in Willamette River Basin. Station names are written above the scatterplots

Basin, the Willamette River Basin, the Upper Columbia River Basin, and the Colorado Headwaters), the CF at the basin scale is computed by fitting a zero-intercept regression line to the sorted AMS of all the available gauges and that of collocated CDR pixels(Figure 2.4). In general, the PERSIANN-CDR estimates of AMS tend to be lower than the AMS from gauge observation, with different levels of underestimation in the different basins. The AMS estimates from the original PERSIANN-CDR dataset show considerable underestimation at Colorado Headwaters and Upper Columbia River Basins with CFs equal to 0.46 and 0.57, respectively.

The scatterplots of CF and gauge elevation for different basins are shown in Figures 2.5(a-d). In general, an exponential relationship exists between CFs and elevations at each of the four basins. Furthermore, when merging all the available gauge information from the selected river basins together, a comprehensive view of this relationship is demonstrated (Figure 2.5e). As shown in Figure 2.5e, the CFs become smaller with increasing elevation of the gauges. This reduction in the CFs implies the underestimation of AMS at higher elevations.

Both IR-based (such as PERSIANN family) and Passive Microwave based (such as TMPA (Huffman et al., 2007)) precipitation products have been reported to underestimate precipitation in high elevations (Hashemi et al., 2017). This underestimation has been related to several factors. Satellite-based precipitation products have difficulties in retrieving the solid form of precipitation (snow), which is the prevailing type of precipitation at high elevation regions and in the winter season (Hashemi et al., 2017). Moreover, since IR-based precipitation algorithms rely on the cloud top temperatures, they cannot fully detect the orographic enhancements in the liquid phase of precipitation in regions characterized by complex topographic conditions (Shige et al., 2013). In addition to the technical and methodological issues inherent to the satellite precipitation estimation methods, the spatial and temporal inconsistencies between the satellite precipitation estimates and gauge observations at high elevation regions can be related to the poor sampling of gauges (Gebregiorgis and Hossain,

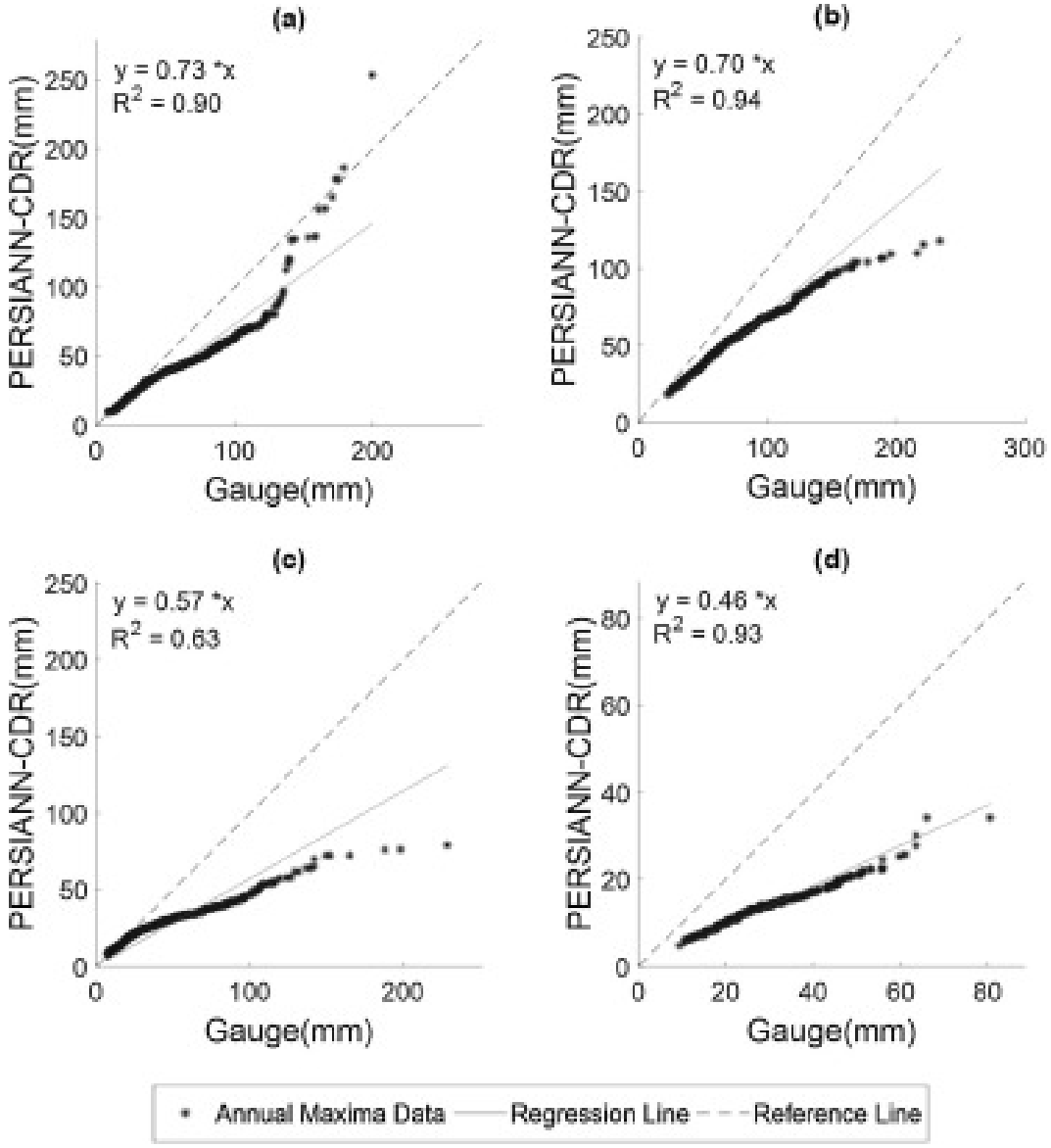

Figure 2.4: CF at basin scale for the selected river basins in the Western United States, including (a) San Joaquin River Basin, (b) Willamette River Basin, (c) Upper Columbia River Basin, and (d) Colorado Headwaters River Basin.

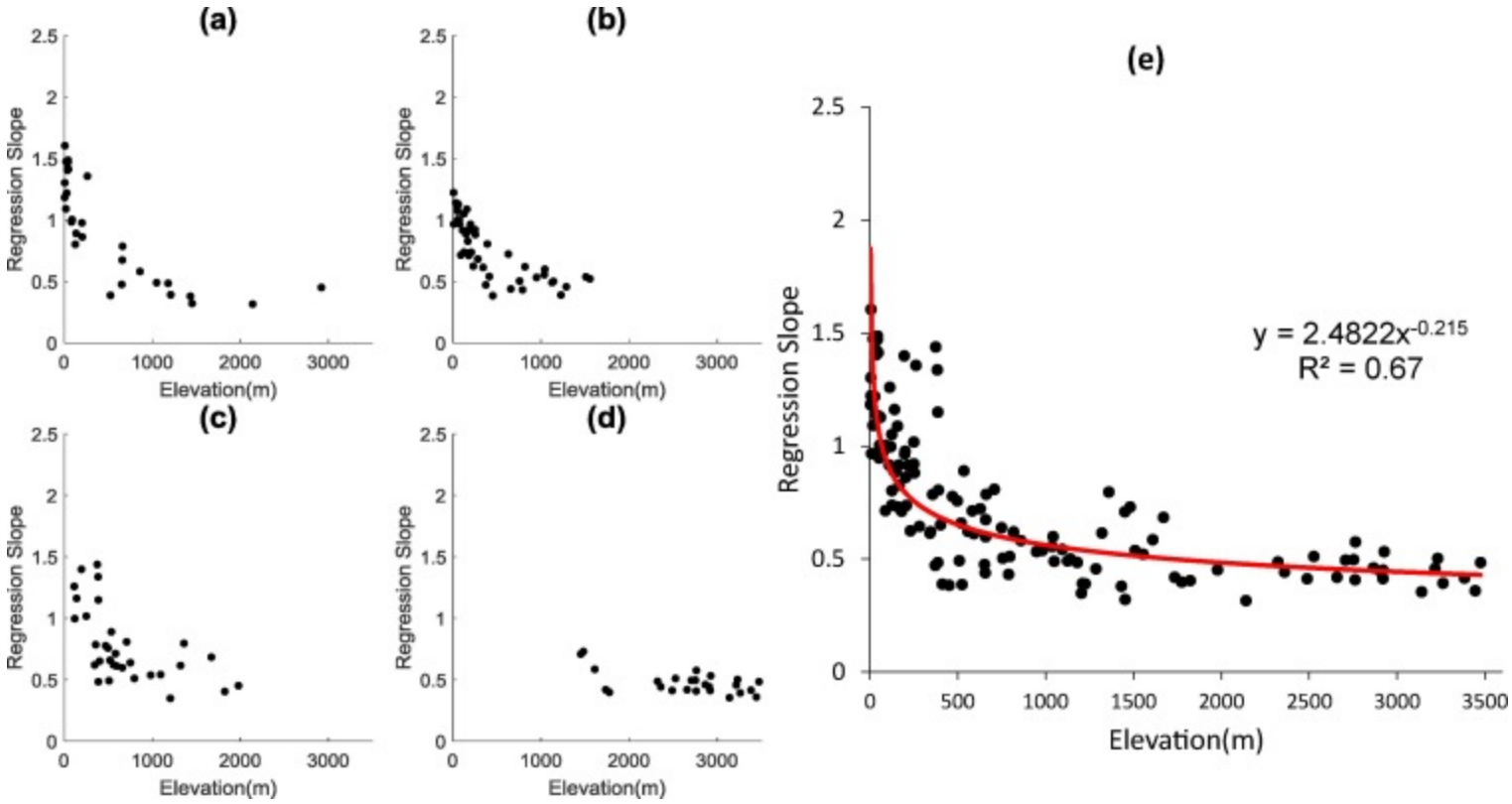

Figure 2.5: CF and elevation relationship at basin and multi-basin scale for (a) San Joaquin River Basin, (b) Willamette River Basin, (c) Upper Columbia River Basin, (d) Colorado Headwaters River Basin, and (e) merging all gauge information for all the basins

2014). For instance, Libertino et al. (2016) observed the lowest agreement in the timing of extreme events recorded by TRMM and gauge observations in sparsely gauged regions. Miao et al. (2015) also reported low spatial and temporal agreement in terms of extreme precipitation statistics between the PERSIANN-CDR estimates and gauge observations in regions with low density of gauges.

As shown in Figure 2.5, we fit an exponential function to the scatterplots of CF for each gauge and its corresponding elevation. This function is used to correct the CDR-based AMS at different basins in the Eastern and Western United States. However, since this correction model is based on only a few selected basins, it is necessary to be validated using different cross-validation techniques and then be tested on different basins over the continental United States.

2.4.2 Hold-out Cross-validation Results

We first carry out hold-out cross-validation on the four selected river basins, in which a correction function based on CF-elevation relationship is built using the information from two of the river basins, Willamette and Upper Columbia river basins. The model is tested on the other two river basins (the San Joaquin and the Colorado Headwater River Basins), and vice versa. The goal is to examine the effect of limited gauge information and basin selection on the overall performance of the bias-correction approach.

The effect of bias-correction on the empirical CDF of the PERSIANN-CDR estimates at each of the calibration basins is shown in Figure 2.6. At basin scale, the correction method shifts the empirical CDF of the AMS from the original CDR towards the gauge-based empirical CDF. In the Willamette River Basin and the Colorado headwaters River Basin, the corrected CDF is close to that of the observation. In the San Joaquin River Basin, the extreme quantiles from the corrected data are closer to the observation. In the Upper Columbia

River basin, the corrected PERSIANN-CDR gives better estimates of the largest extreme values compared to the original PERSIANN-CDR. However, it results in an overestimation of the lower quantiles. This is consistent with the results shown in Figure reffig:Fig2-4, where the regression-based estimates gave some overestimation for values lower than 55 mm.

The statistics of the hold-out cross-validation results at gauge scale are presented in Table 2. In most of the gauge locations (111 out of 127 gauges in different basins), the RMSE of the corrected PERSIANN-CDR is lower than that of the original PERSIANN-CDR. This implies the effectiveness of the proposed bias-adjustment approach in correcting the PM at pixel level even in basins with dense gauge networks. At 16 gauges, however, the correction method tends to deteriorate the original PERSIANN-CDR estimates. Among these gauges, 12 are located in low elevation regions (¡550 meters from mean sea level), and more than half of them are associated with elevations less than 200 meters from mean sea level. The Upper Columbia and the Willamette River Basins have a larger portion of these gauges with 7 and 5 unsuccessful corrections, respectively. The poor performance of the corrected CDR at those gauge locations could be partly attributed to the complex topographic conditions of those basins, which pose some challenges for the PERSIANN algorithm to estimate precipitation accurately. However, as compared to the original PERSIANN-CDR, the proposed correction approach works well for the majority of gauges in the hold-out cross-validation cases as shown with the lower RMSE values in Table 2.2.

In addition, the lower variability of CF at different elevations (Figure 2.5-e) also implies that the correction model has a lower uncertainty at gauges with higher elevation. Having accurate information about extreme precipitation at high elevation regions is very critical since these regions typically account for a considerable fraction of water resources. However, these regions are often poorly gauged and the gauge networks are not often capable of capturing the spatiotemporal variability of extreme precipitations.

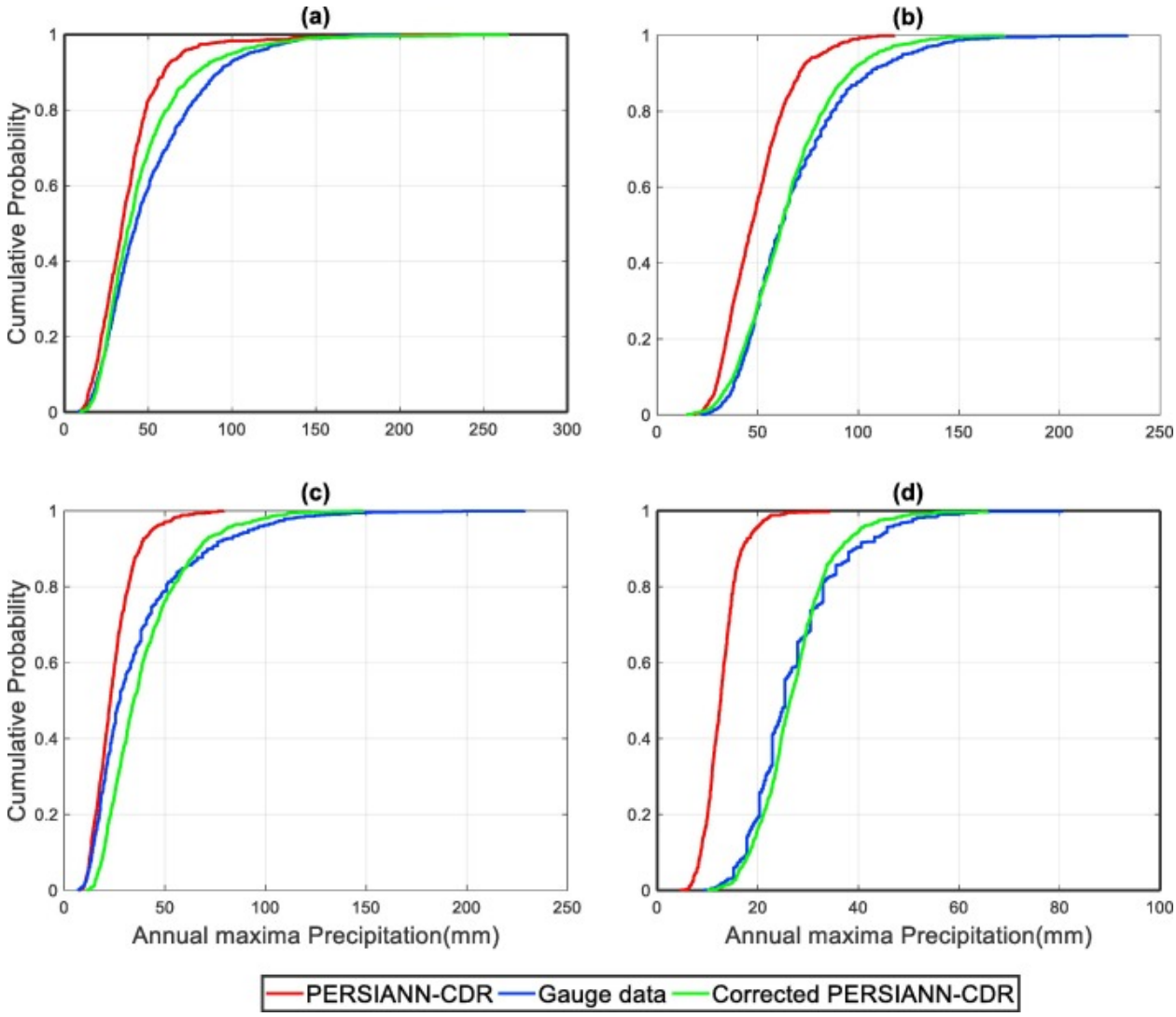

Figure 2.6: Empirical CDF of the AMS from the gauge observations, the original and the corrected PERSIANN-CDR data at basin scale. (a) San Joaquin River Basin, (b) Willamette River Basin, (c) Upper Columbia River Basin, and (d) Colorado Headwaters River Basin

Table 2.2: The RMSE(mm) of the original and corrected PERSIANN-CDR data during hold-out cross-validation at different gauge locations and basins

San Joaquin		Willamette		Upper Columbia		Colorado Headwaters	
Corrected	Original	Corrected	Original	Corrected	Original	Corrected	Original
14.76	16.74	27.6	54.73	13.3	19.68	6.16	18.2
19.13	34.44	5.78	5.78	3.76	3.09	4.71	18.73
32.66	47.61	11.26	24.65	4.12	8.66	5.44	18.29
31.41	69.29	15.46	11.15	1.32	8.61	5.25	10.88
12.96	**4.26**	16.73	19.15	2.93	8.02	7.02	9.76
43.12	71.64	30.79	50.9	7.38	31.3	6.43	19.97
9.42	8.59	6.51	9.53	3.61	**1.91**	8.98	**6.5**
10.03	10.1	7.42	20.92	15.25	20.72	6.21	17.25
19.79	25.71	11.85	18.53	1.69	4.71	4.12	12.42
6.11	5.49	10.43	11.36	4.97	8.45	4.8	16.22
19.16	36.62	4.99	**4.21**	6.2	10.88	5.09	12.83
30.47	59.5	6.65	11.81	0.96	4.25	3.74	18.69
8.86	13.73	20.38	37.86	9.12	21.9	4.74	12.75
23.12	**10.42**	9.43	**7.62**	3.17	4.97	4.03	19.37
6.57	6.29	14.5	21.04	11.72	**6.27**	2.61	18.97
16.38	19.47	9.79	19.52	7.36	15.71	5.66	23.01
30.53	20.49	13.75	**8.71**	0.92	4.3	1.98	15.97
3.25	9.45	13.34	40.6	5.08	9.13	4.12	13.03
22.05	50.93	45.06	65.65	26.64	34.04	5.98	14.1
8.12	26.77	11.12	11.52	8.59	9.39	4.32	13.81
13.91	18.23	2.94	4.9	3.58	10.14	2.73	15.47
13.69	23.67	2.36	6.02	8.59	**4.84**	3.01	15.38
10.34	15.72	17.35	7.06	19.52	**8.05**	6.2	12.17
17.74	36.22	4.41	8.65	7.33	40.04	7.29	23.12
24.67	47.21	24.83	44.44	14.55	53.51	9.89	**5.98**
19.9	31.57	11.39	**4.63**	9.88	19.4	-	-
12.03	27.9	9.58	27.84	8.47	28.97	-	-
16.77	20.93	3.29	3.55	19.66	**14.44**	-	-
-	-	6.39	33.06	43.31	77.52	-	-
-	-	7.81	27.53	13.28	**7.61**	-	-
-	-	25.35	54.1	17.14	**10.74**	-	-
-	-	8.42	39.02	-	-	-	-
-	-	9.66	44.36	-	-	-	-
-	-	29.91	66.88	-	-	-	-
-	-	11.66	37.27	-	-	-	-
-	-	13.56	48.13	-	-	-	-
-	-	7.22	24.98	-	-	-	-
-	-	6.97	34.96	-	-	-	-
-	-	13.64	56.23	-	-	-	-
-	-	16.4	24.77	-	-	-	-
-	-	4.53	6.53	-	-	-	-
-	-	12.97	**10.91**	-	-	-	-
-	-	5.74	7.32	-	-	-	-

* Note: Bold values show the cases where RMSE of the original PERSIANN-CDR is lower than the corrected PERSIANN-CDR.

Table 2.3: he RMSE (mm) from leave one out cross validation using gauge interpolation, original and corrected PERSIANN-CDR data

Method	Basin Name			
	San Joaquin	Willamette	Upper Columbia	Colorado Headwaters
Interpolation	21.61	16.06	7.87	6.84
Corrected CDR	17.34	12.77	9.79	5.22
Original CDR	26.45	23.95	16.22	15.31

* Note: The bold value shows the case where the corrected PERSIANN-CDR method gave a higher RMSE value at basin scale than the interpolation method.

2.4.3 Leave-one-out Cross-validation

In each basin, one gauge is left out at a time, and the time series of precipitation at that gauge location is constructed using linear interpolation. The annual maximum time series from the gauge interpolation and the corrected PERSIANN-CDR are compared with the gauge observations at the corresponding location (Table 3). As shown in Table 2.3, the RMSE values from the corrected PERSIANN-CDR are consistently lower than those of the original PERSIANN-CDR for all basins. When compared to the interpolation method, corrected PERSIANN-CDR gives lower RMSE values at the San Joaquin, the Willamette, and the Colorado Headwaters River Basins. At the Upper Columbia River Basin, however, the leave-one-out cross-validation results suggest that gauge interpolation performs better than the corrected PERSIANN-CDR data.

It is inferable from the gauge scale results that the correction model outperforms the interpolation method in most cases, even if only one of the gauges at a densely gauged basin is removed from the sample. The interpolation method also produces substantial errors at some gauge locations, particularly those locations where the interpolated gauge is relatively far from its surrounding gauges. It is possible that complex topography leads to different precipitation characteristics between nearby gauges and results in uncertainties in the interpolated precipitation estimates.

2.4.4 K-fold Cross-validation

The leave-one-out cross-validation results in the previous section demonstrate that the interpolation-based estimates of AMS achieved by removing one of the gauges may outperform the PERSIANN-CDR estimates at some gauges in a densely-gauged region (e.g., the Upper Columbia River Basin). In order to find the breakpoint where the corrected PERSIANN-CDR will outperform interpolation-based estimates at a basin scale, the k-fold cross validation is implemented. We randomly separate different fractions of all available gauges (0.1, 0.2, ..., 0.8 of the gauges) in a basin, and remove the selected gauges from the model training phase. This random selection and removal process is repeated 30 times for each fraction level. Then, the entire precipitation time series at those locations are constructed by the linear interpolation of observations from the remaining gauges in that basin. Then RMSE of AMS estimates from both corrected PERSIANN-CDR and gauge interpolation are computed at the removed gauges.

Figure 2.7 shows the average RMSE values of AMS estimates from the interpolation method (blue line) and the corrected PERSIANN-CDR (red line) for different exclusion ratios in each river basin. The horizontal axis defines the number of the iteration, and the vertical axis presents the average RMSE value of the AMS estimates on the excluded gauge locations using the corrected PERSIANN-CDR and gauge interpolation. As the fraction of gauges being removed from the entire samples increases, the errors associated with the interpolation method become larger. In contrast, the errors produced with our proposed correction method remain consistently low for different basins over most of the test scenarios (i.e., different percentages of the gauge being removed). Moreover, the interpolation-based estimates result in large errors in some test scenarios and basins. For example, in the San Joaquin River Basin (Figure 2.7a), substantial errors are observed in different scenarios and over several independent runs.

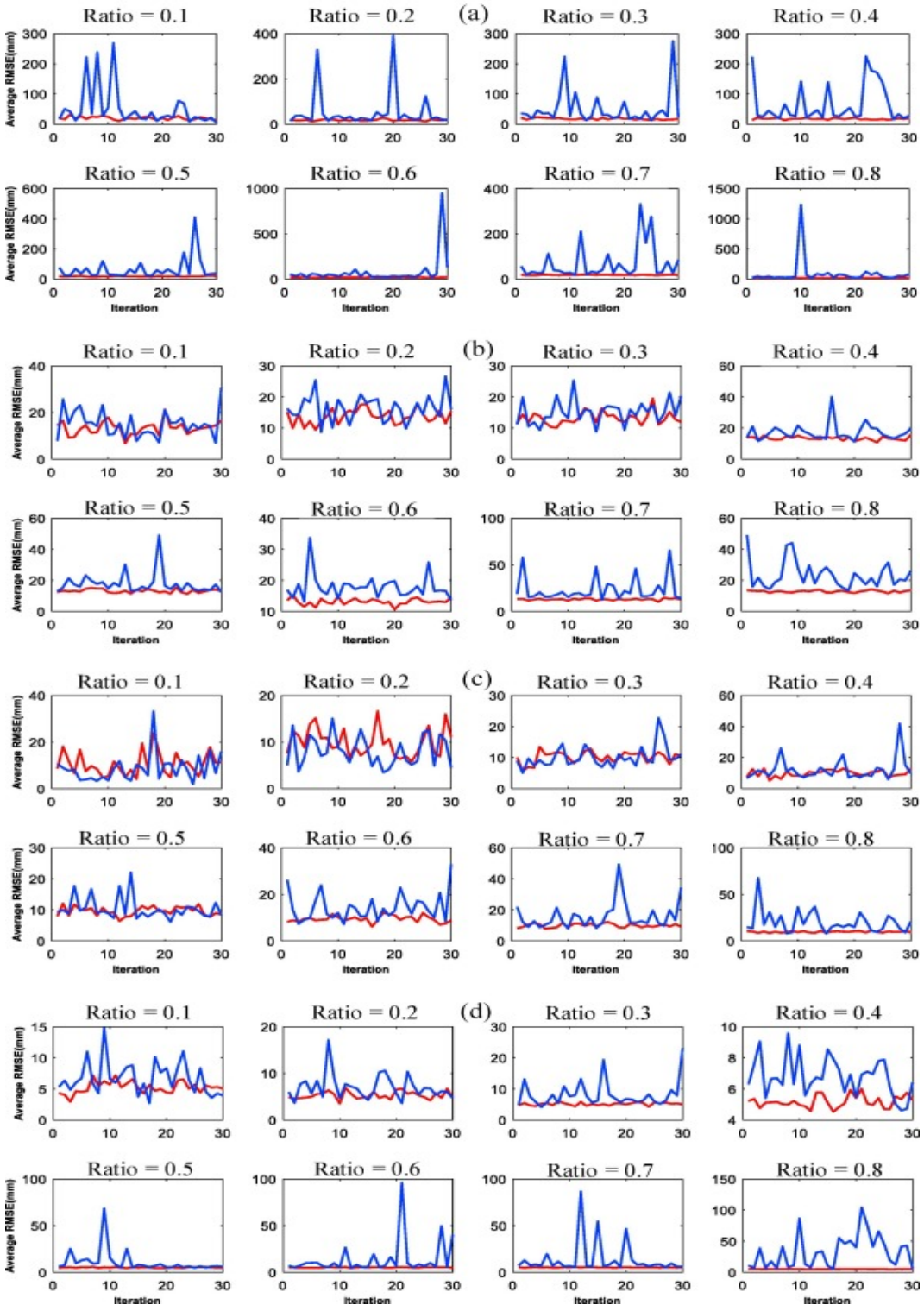

Figure 2.7: Average RMSE of AMS estimates from corrected PERSIANN-CDR (red lines) and interpolation by k-fold cross-validation (blue lines) for different exclusion ratios at: (a) the San Joaquin River Basin, (b) the Willamette River Basin, (c) the Upper Columbia River Basin, and (d) the Colorado Headwaters River Basin

There are several reasons why errors from the interpolation method have large values in some of the iterations. Extreme precipitation events vary substantially in space and time. The annual maximum precipitation at different points of a basin could be results of various extreme events occurring in different times of the year. When interpolating the daily gauge observations in a region for constructing precipitation time series at an ungauged site, heavy precipitation observed at one or more gauge locations could be falsely extended to the locations that were less impacted by the storm. Similarly, by removing some of the gauges from the population, the extreme events impacting those locations may not be represented in the interpolated time series from the remaining sample and as a result the extreme event at that location would be missed. Both of these cases may result in considerable errors in the annual maximum series estimated from the interpolation method. Other factors that contribute to the significant interpolation errors include long distance of sample gauges from the target locations, substantial elevation differences between the target locations and sample gauges, and the inability of the sample gauges to demonstrate the spatiotemporal variability of rainfall at target locations.

The overall errors from the corrected PERSIANN-CDR and the interpolation method at different exclusion ratios and basins are shown in Figure 2.8. As the portion of gauges being left out increases, the RMSE produced by the interpolation method increases for all the basins, while the proposed correction method for PERSIANN-CDR shows stable errors over different ratios and basins with respect to the AMS results. In the San Joaquin River Basin (Figure 8a), the Willamette River Basin (Figure 2.8b), and the Colorado Headwaters River Basin (Figure 2.8d), the corrected PERSIANN-CDR yields lower RMSE values than the gauge interpolation method throughout different ratios, suggesting the effectiveness of the proposed correction approach. In the Upper Columbia River Basin, the gauge interpolation method results in better estimates of the AMS at the ratios up to 30%. However, beyond the 30% threshold, the corrected PERSIANN-CDR produces more accurate estimates of the AMS. Therefore, 30% of total gauges is the breakpoint for the Upper Columbia River Basin

in the context of interpolating point gauge information to spatial estimates. By comparing the statistics of corrected PERSIANN-CDR and the traditional interpolation method, it is observed that the proposed correction model generates more accurate estimates of the AMS than does the linear interpolation method. The superiority of the proposed bias-correction method becomes increasingly evident as the gauges become sparser.

2.4.5 Validation on the Continental U.S.

In previous sections, I demonstrated the effectiveness and robustness of the proposed correction model on the four representative river basins in the western U.S. In this section, I extensively validate the correction model on 16 additional river basins with different climates and topographic conditions across the continental United States (Table 2.1). The selected basins for validation cover all the climate classes available in the United States based on the Köppen-Geiger climate classification system. In addition, these basins cover a broad range of elevations, from low-lying regions in the state of Florida to high elevation regions in the state of Utah. These basins are also associated with various dominant precipitation mechanisms (such as convective, orographic, and cyclonic) which could influence the performance of the satellite-based precipitation products (Hong et al., 2007; Liu and Zipser, 2009).

Table 2.4 presents the errors in AMS estimates from the original and the corrected PERSIANN-CDR data on the tested river basins. According to Table 4, in 15 out of the 16 basins, the correction model results in lower RMSE values compared to the original PERSIANN-CDR data. Significant improvements are observed at high elevation regions such as Dirty Devil, Rio Grande, and Upper Yellowstone river basins with 78.7 %, 72.3 %, 71.6% reduction in the RMSE of AMS, respectively. Also, the correction model considerably decreases the errors in the AMS estimates at mid-elevation regions, such as Mississippi headwaters, Upper Mississippi-Iowa, and Upper Tennessee River basins (Table 2.4). Among the low elevation

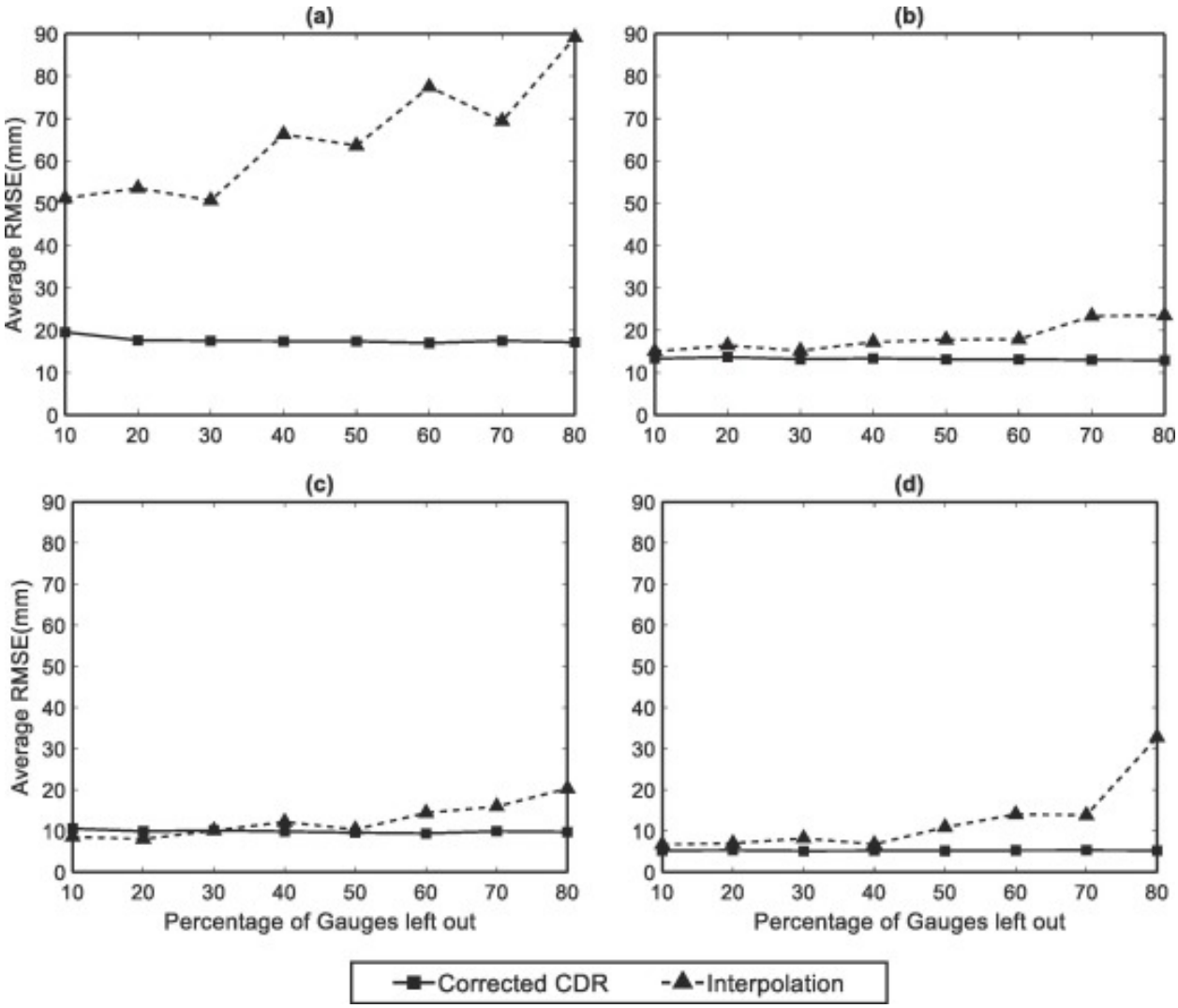

Figure 2.8: Overall RMSE of AMS estimates from corrected PERSIANN-CDR (solid line) and interpolation (dashed line) at different basins, including (a) the San Joaquin River Basin, (b) the Willamette River Basin, (c) the Upper Columbia River Basin, and (d) the Colorado Headwaters River Basin.

regions, Nueces-Southwestern Texas Coastal and Trinity River basins were quite successful with respect to the error reduction by the correction model. However, Pascagoula River Basin is less successful (7.3% decrease in RMSE) and South Florida River Basin fails to improve (29.7% increase in RMSE). Both of these basins are located in the South Atlantic Gulf region, which is characterized by warm convective precipitation mechanisms. As a result of these convective systems, satellite precipitation products often fail to provide accurate estimates at these regions, as we see from the performance of raw data shown in Table 2.4. Both the Pascagoula and the South Florida river basins have high initial errors compared to the other river basins. Since the model is trained using the information from four river basins in the western United States with different hydroclimatic conditions, it is reasonable for it to not perform as well under temperate and tropical climatic conditions and for extremes caused by warm convective systems.

Generally, satellite precipitation estimation algorithms perform poorly in estimating precipitation from shallow and warm convective clouds (Hong et al., 2007; Kubota et al., 2009; Liu and Zipser, 2009; Sorooshian et al., 2002). One reason behind this poor performance is that these algorithms relate heavy precipitations to deep convective clouds and subsequently underestimate heavy precipitations associated with shallow warm clouds (Hong et al., 2007; Liu and Zipser, 2009). Moreover, IR-based methods such as PERSIANN are based on cloud top temperature thresholds that are sometimes too cold for warm orographic clouds (Adler et al., 2003; Dinku et al., 2008). Finally, due to the contamination by the cold anvil cirrus clouds, IR-based precipitation estimates typically display 1-3 hr phase shift compared to the maximum diurnal precipitation. These phase shifts influence the performance of IR-based methods in regions dominated by warm convective clouds (Sorooshian et al., 2002).

Table 2.4: Bias-correction results in selected basins over the United States

Basin No.	Basin Name	Average RMSE(mm)		Change (%)
		Original PERSIANN-CDR	Bias-Corrected PERSIANN-CDR	
1	Arkansas-Keystone	30.9	12.02	-61.1
2	Central Nevada Desert	14.16	6.91	-51.2
4	Dirty Devil	15.35	3.27	-78.7
5	Kootenai-Pend Oreille-Spokane	24.23	9.67	-60.1
6	Lower Snake	17.36	4.94	-71.6
7	Mississippi Headwaters	19.12	3.42	-82.1
8	Nueces-Southwestern Texas Coastal	28.68	17.43	-39.2
9	Pascagoula	39.2	36.32	-7.3
10	Rio Grande - Elephant Butte	15.67	4.34	-72.3
12	Southern Florida	35.4	45.92	**29.7**
13	Susquehanna	22.61	10.64	-52.9
14	Trinity	35.62	21.87	-38.6
16	Upper Mississippi-Iowa	23.83	7.24	-69.6
17	Upper Tennessee	27.14	10.15	-62.6
18	Upper Yellowstone	18.68	5.31	-71.6
19	Wabash	23.36	11.46	-51

* Note: The underlined value shows the case where the adjustment of PERSIANN-CDR data failed to improve the errors in the annual maximum series estimates.

2.4.6 Multi-day Annual Maximum Series

In Figure 2.9, the scatterplots of the CF-elevation for multi-day duration AMS at Colorado Headwaters (Figures 2.9 a-j) are presented as an illustrative example. Figures 2.9 (a)-(j) suggest there is a similar CF-elevation behavior in multi-day AMS analysis for different durations. Figure 2.9(k) presents the exponential regression functions fitted to each of the N-day maximum scatterplots. According to Figure 2.9 (k), as durations increase from 1 day to 60 days, the original PERSIANN-CDR estimates of the AMS become more accurate (i.e., closer to the CF=1 line). This is because the PERSIANN-CDR dataset is bias-adjusted with GPCP dataset (Huffman et al., 2007) at a monthly scale and the values from the two datasets become closer to each other at longer durations. Therefore, at 30-days or 60-days analysis, the AMS estimates should be close to gauge observation. Although PERSIANN-CDR and gauge information are adjusted at a monthly scale, the monthly coefficients are applied to daily estimates (Ashouri et al., 2015). Therefore, the sub-monthly or daily estimates may not be compatible with gauge observations at the corresponding scale. Furthermore, the GPCP is a gauge interpolated dataset which its pixel values are essentially the average values of gauge observations within the large grid boundary. However, here we compare the PERSIANN-CDR estimates in pixel scale with the collocated gauge values which could differ substantially from the corresponding GPCP pixel values.

2.4.7 Depth-Duration-Frequency Curves

Figure 2.10 shows the DDF curves derived from the adjusted CDR data, the frequency estimates from NOAA Atlas 14, and the 90% confidence intervals for a gauge location in Dirty Devil basin in the state of Utah (USC00420849). We present return levels for daily and multi-day durations given the daily resolution of the PERSIANN-CDR dataset. As shown in Figure 10, the frequency estimates from the original PERSIANN-CDR data are

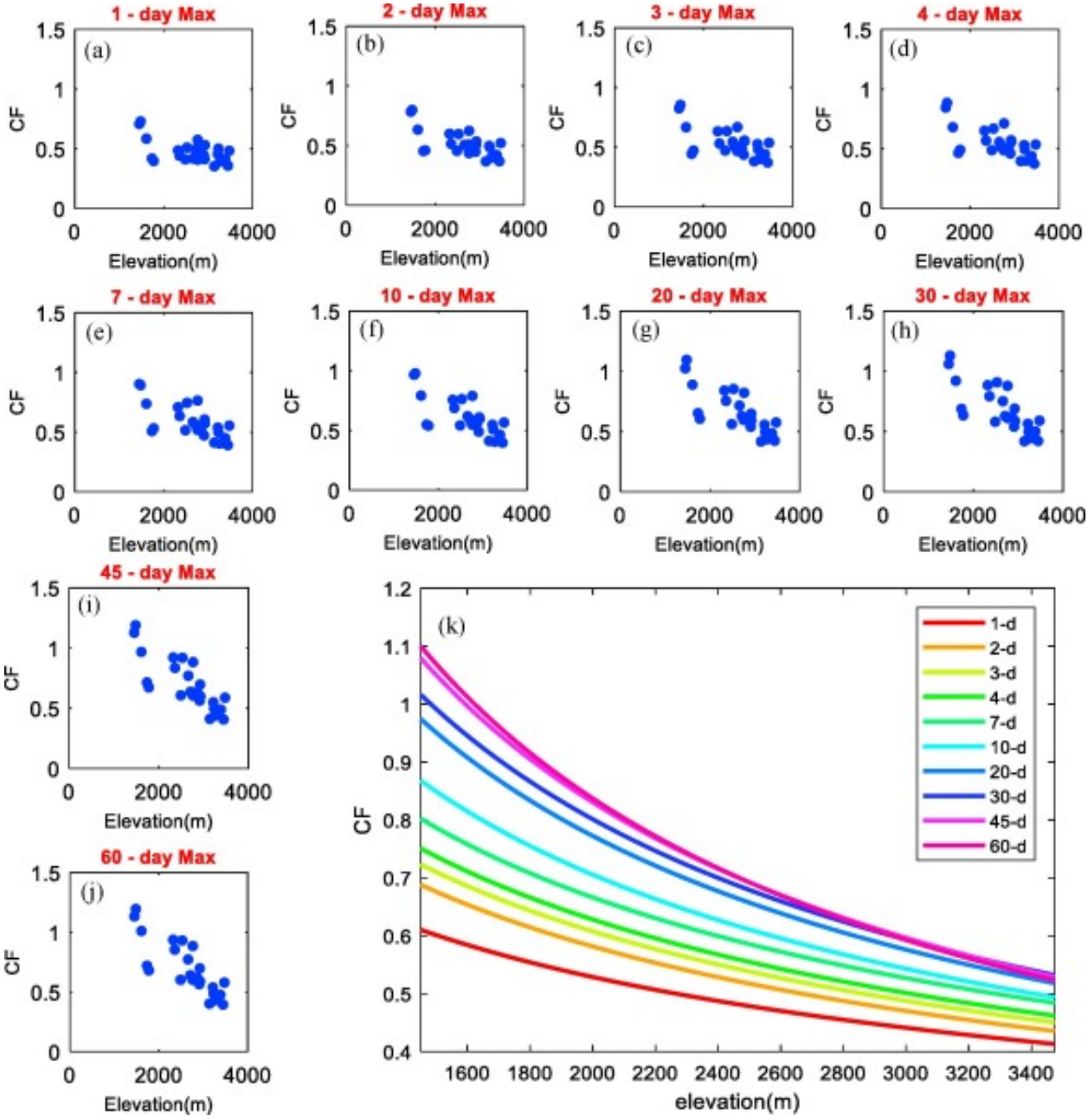

Figure 2.9: Scatterplots of CF-elevation for different durations(a-f) and the exponential regression fitted to the CF-elevation data for different durations(k) at Colorado Headwaters Basin

outside the 90% confidence intervals of the NOAA Atlas 14 which suggests the necessity of bias adjustment prior to employing the data for frequency analysis. On the other hand, DDFs from the adjusted PERSIANN-CDR data are well within the 90% confidence intervals of the NOAA Atlas 14 DDFs. In most cases, the frequency estimates from the adjusted PERSIANN-CDR are very close to the NOAA Atlas 14 estimates which are calculated by incorporating a larger number of gauges and longer records of data for frequency estimation. Larger deviations from the gauge-based estimates are observed at longer return periods, and there is no clear trend in terms of overestimation or underestimation with respect to duration.

As shown in Figure 2.10, the confidence intervals from the gauge-based and satellite-based DDFs become larger as the return periods increase. This higher uncertainty is because of the lower sample size at the tails of the distributions. Furthermore, the confidence intervals from the original and the adjusted PERSIANN-CDR datasets are relatively comparable given the similar lengths of the two datasets. However, the uncertainty bounds from the satellite-based DDFs are larger than those from the NOAA Atlas 14. One reason behind these larger confidence intervals is the shortness of the PERSIANN-CDR dataset when compared to the gauge information used for the development of NOAA Atlas 14 DDFs. Another reason is the difference between the frequency analysis method implemented here and the method employed in the development of NOAA Atlas 14. NOAA uses the regional frequency analysis based on L-moments to estimate the frequency and intensity of extremes (Hosking and Wallis, 2005). The regional frequency analysis method is used in Atlas 14 in order to relieve the uncertainties arising from a low sample size (limited years of observations) during the GEV parameter estimation process. Although the regional frequency analysis method gives frequency estimates with lower uncertainties, it comes with the assumption of regional homogeneity in extreme rainfall characteristics which is not always a valid assumption. Here, the frequency analysis methods and uncertainties of the frequency estimates are outside of the scope of this study, and the DDF curves and their error analyses are the proof of concept.

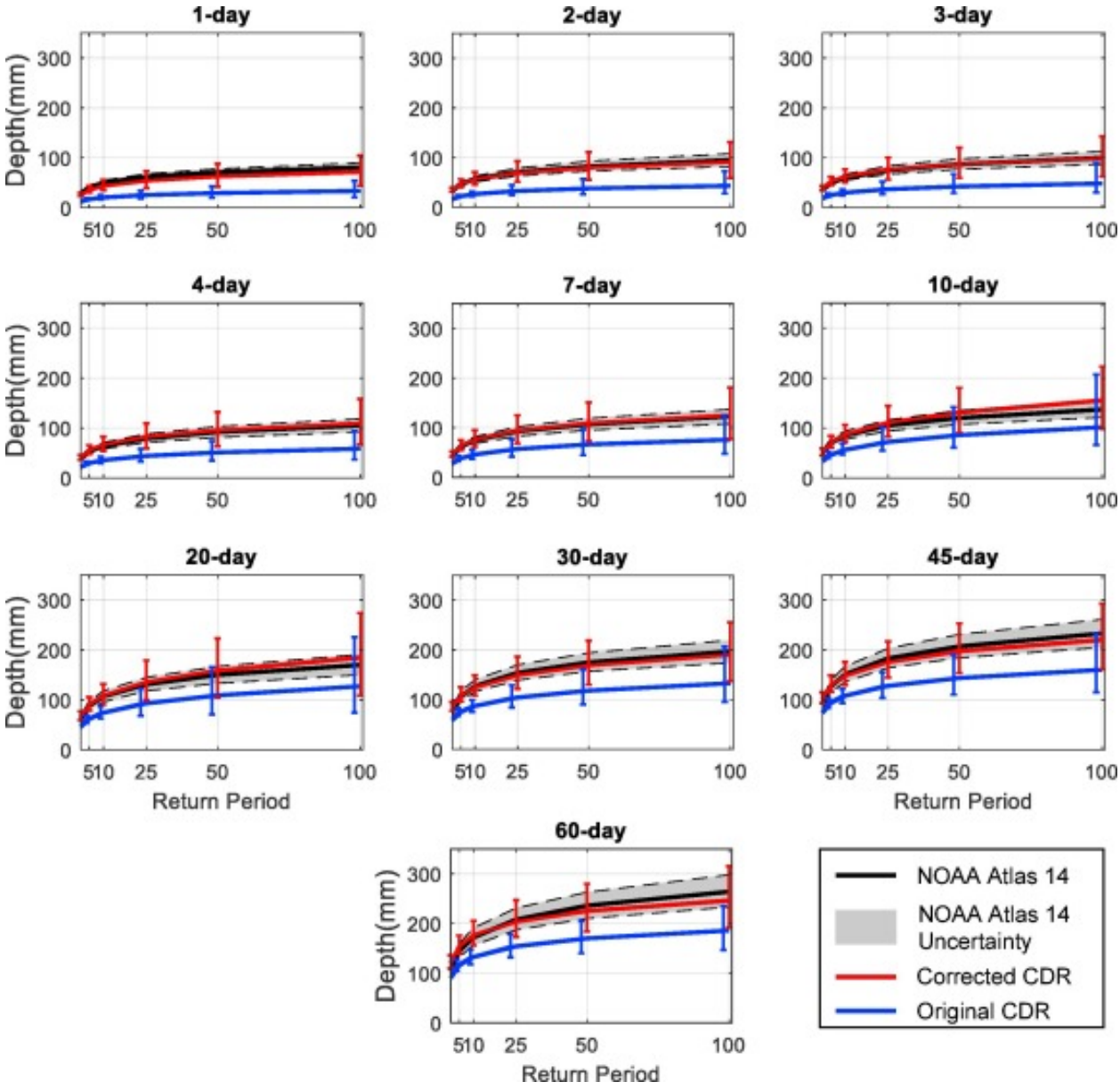

Figure 2.10: Frequency estimates from corrected PERSIANN-CDR, original PERSIANN-CDR and NOAA Atlas 14 with 90% Confidence intervals at gauge USC00420849 in Dirty Devil basin, UT. The red vertical bars, blue vertical bars, and gray shaded area show the 90% Confidence intervals from corrected PERSIANN-CDR, original PERSIANN-CDR and NOAA Atlas 14, respectively.

As seen in Figure 2.10, DDFs from the original PERSIANN-CDR suggest underestimation of the extreme precipitation quantiles for different durations. This is expected given the spatial resolution of this dataset. In fact, when considering the remotely sensed precipitation information, we should be aware that the pixel value represents a spatial average of precipitation within the extent of a pixel. In other words, the pixel value disregards the subpixel variability and even if the PERSIANN-CDR estimate at a pixel is completely accurate, its value tends to be smaller than the collocated point measurements. As a result, the extracted DDFs from a satellite pixel tend to demonstrate lower return intervals (Peleg et al., 2018), as observed in Figure 2.10.

It is worth noting that the estimated DDF curves are not necessarily based on the liquid-phase precipitations and the extracted AMS may comprise snowfalls as well. This is because PERSIANN-CDR and many other satellite-based precipitation estimation algorithms do not distinguish between precipitation phases. In other words, the annual maximum time series extracted and used here may contain solid-phase precipitation extremes due to snowfalls. Although this study does not differentiate between solid and liquid phases of precipitation in order to obtain purely rain-based DDFs, the current framework can be further modified to incorporate additional observations on solid precipitations. There are two approaches to achieve this goal. One approach for this would be to limit the analysis to warm seasons, but the definitions of warm season vary among various geographic locations. Another approach would be to distinguish snowfall from rainfall, but this would require snowfall and air temperature data that are not available everywhere. Future independent research may improve upon the current study by including such additional information.

Figure 2.11 displays the box plots of RMSE of the return level estimates from the original and corrected CDR for different durations and return periods at collocated PERSIANN-CDR pixels and gauges for different basins in the continental US. The corrected PERSIANN-CDR data was used to obtain frequency estimates at different gauge locations in the selected

basins, and the results were compared with those from NOAA Atlas 14. Note that three out of the 16 basins (basins 5, 6 and 15) were located in the Pacific Northwest region and two basins (basins 8 and 14) were located in the state of Texas, all of which were not covered by or were being updated in the recent volumes of NOAA Atlas 14. Thus, the frequency estimates were only validated at the remaining 11 basins as shown in Figure 2.11.

According to Figure 2.11, the RMSE values for return level estimates corresponding to longer return periods are generally higher for both datasets. This is expected as the PERSIANN-CDR dataset is relatively shorter than the gauge information used for the development of NOAA Atlas 14. The shorter record will result in smaller samples, higher uncertainties, and larger deviations at the tails of the distribution. Over the tested basins, the frequency estimates from the corrected PERSIANN-CDR data have consistently lower median RMSE values than those from the original PERSIANN-CDR at different return periods. The RMSE values at the basins with higher elevations (such as Central Nevada, or Dirty Devil basins) were relatively lower than these at basins with lower elevations (such as Mississippi Headwaters, or Upper Mississippi-Iowa basins), which implies the suitability of the correction approach for high elevation regions. Furthermore, in most of the basins and at different return periods, the corrected dataset shows lower variability in RMSE of the frequency estimates. Corrected PERSIANN-CDR data also demonstrate superior performance in terms of median RMSE and variability of RMSE values at the gauges within the basins. The only case for which the corrected PERSIANN-CDR results in higher RMSE values at different return periods and durations is the South Florida basin, where it was previously shown that the correction model does not improve the AMS estimates due to the climate and the precipitation mechanism.

The relative errors of the frequency estimates are calculated to show the relative magnitude of the return level errors compared to the return levels from NOAA Atlas 14. The relative error here is the difference between the frequency estimates from PERSIANN-CDR (original and

bias-adjusted) and NOAA Atlas 14, divided by the value from NOAA Atlas 14. Figure 2.12 demonstrates the absolute value of the relative error for the frequency estimates at different durations and return periods from the corrected and original PERSIANN-CDR data. As shown, the relative errors from the corrected PERSIANN-CDR data have consistently lower median values, as well as, lower variability at different return periods in the tested basins. The median relative errors from the corrected data are less than 20% different from the return levels estimated by NOAA Atlas 14. Similar performance is observed when the relative errors of frequency estimates from the two datasets are compared with respect to the extreme precipitation duration. It is also noted that the corrected PERSIANN-CDR dataset does not show a systematic increase or decrease in the relative errors of the frequency estimates, with respect to the duration. The relative errors of the return level estimates from the original PERSIANN-CDR data tend to decrease with increasing duration. This finding is consistent with our observations in Figure 2.9 that revealed lower errors of the original PERSIANN-CDR data for longer duration extreme events. As with Figure 2.11, the only case in which the corrected data resulted in higher RMSE values was the South Florida basin where the correction model did not improve the AMS estimates.

2.5 Summary and Conclusions

In this study, the application of the PERSIANN-CDR dataset for rainfall frequency analysis was investigated. A bias correction model was developed to further correct the PERSIANN-CDR estimates of annual maximum time series at the pixel scale. The proposed correction approach was implemented in two steps: (1) Bias correction factors at limited gauge locations were estimated using linear regression analysis between annual maximum series (AMS) of gauges and collocated pixels; and (2) The correction factors from the limited gauge locations were extended to other regions where gauge data were not available. The correction model

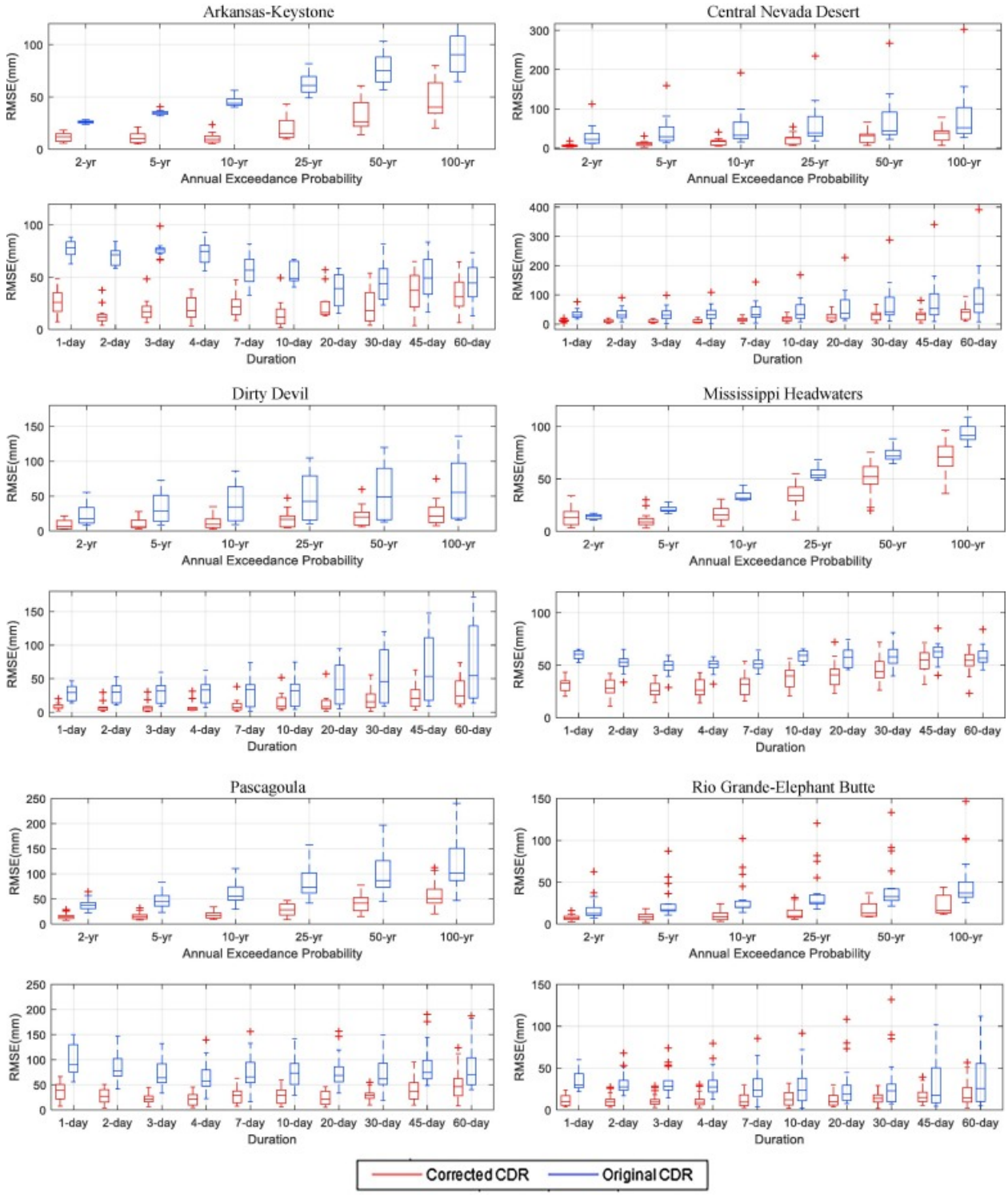

Figure 2.11: RMSE of corrected(red) and original(blue) PERSIANN-CDR frequency estimates for the selected basins in the continental United States.

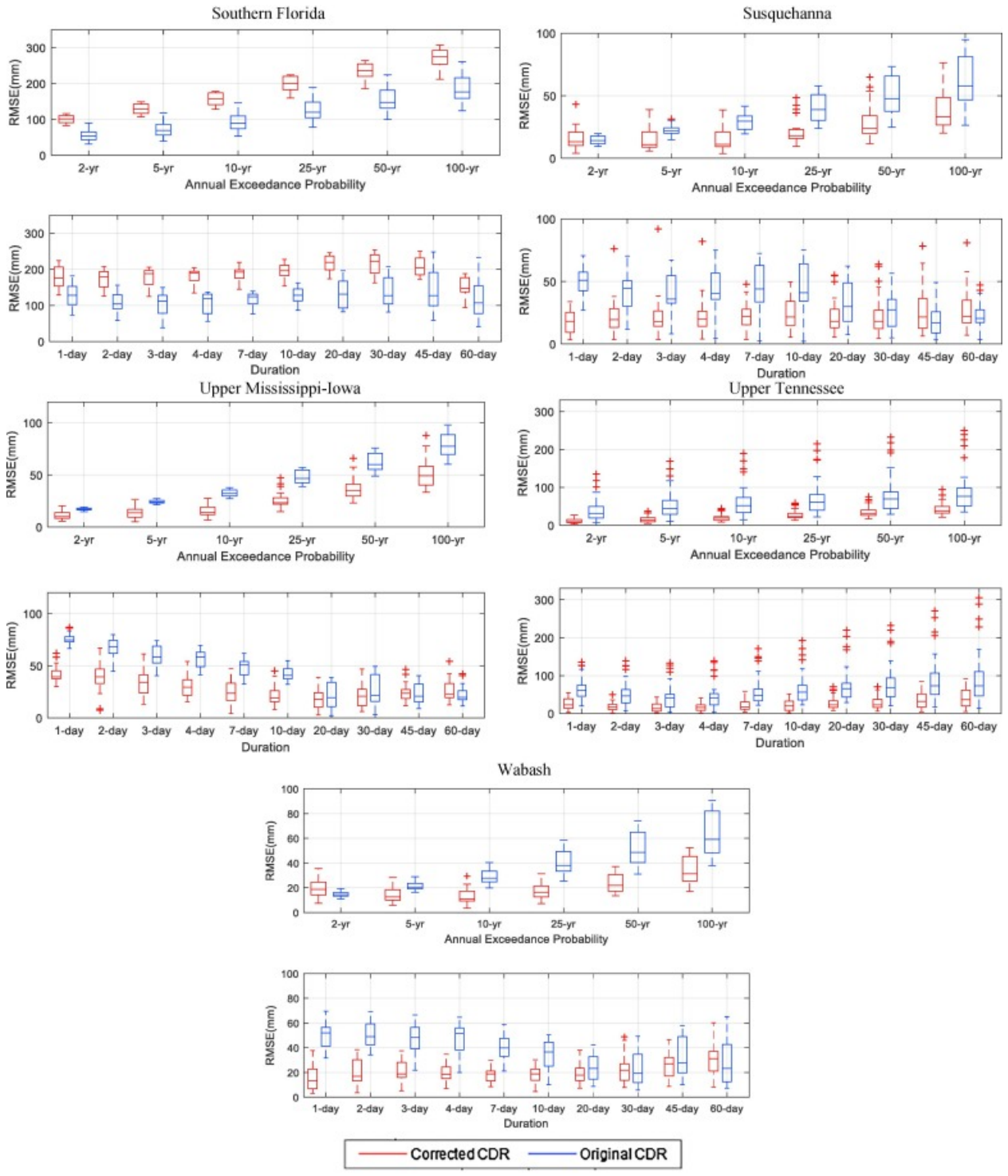

Figure 2.11: Continued

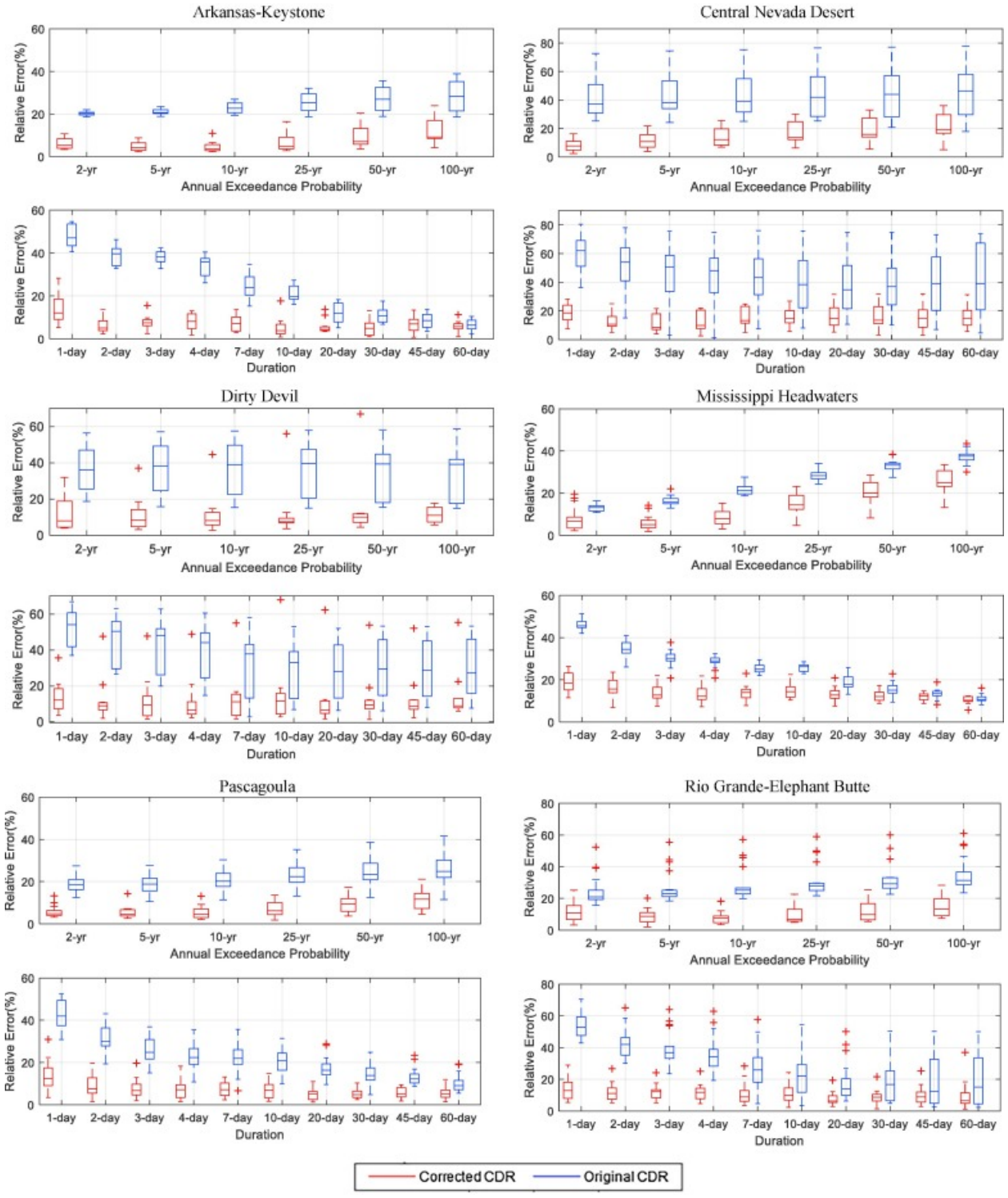

Figure 2.12: Absolute relative error (%) of return level estimates for different durations from corrected(red) and original(blue) PERSIANN-CDR for the selected basins in the United States.

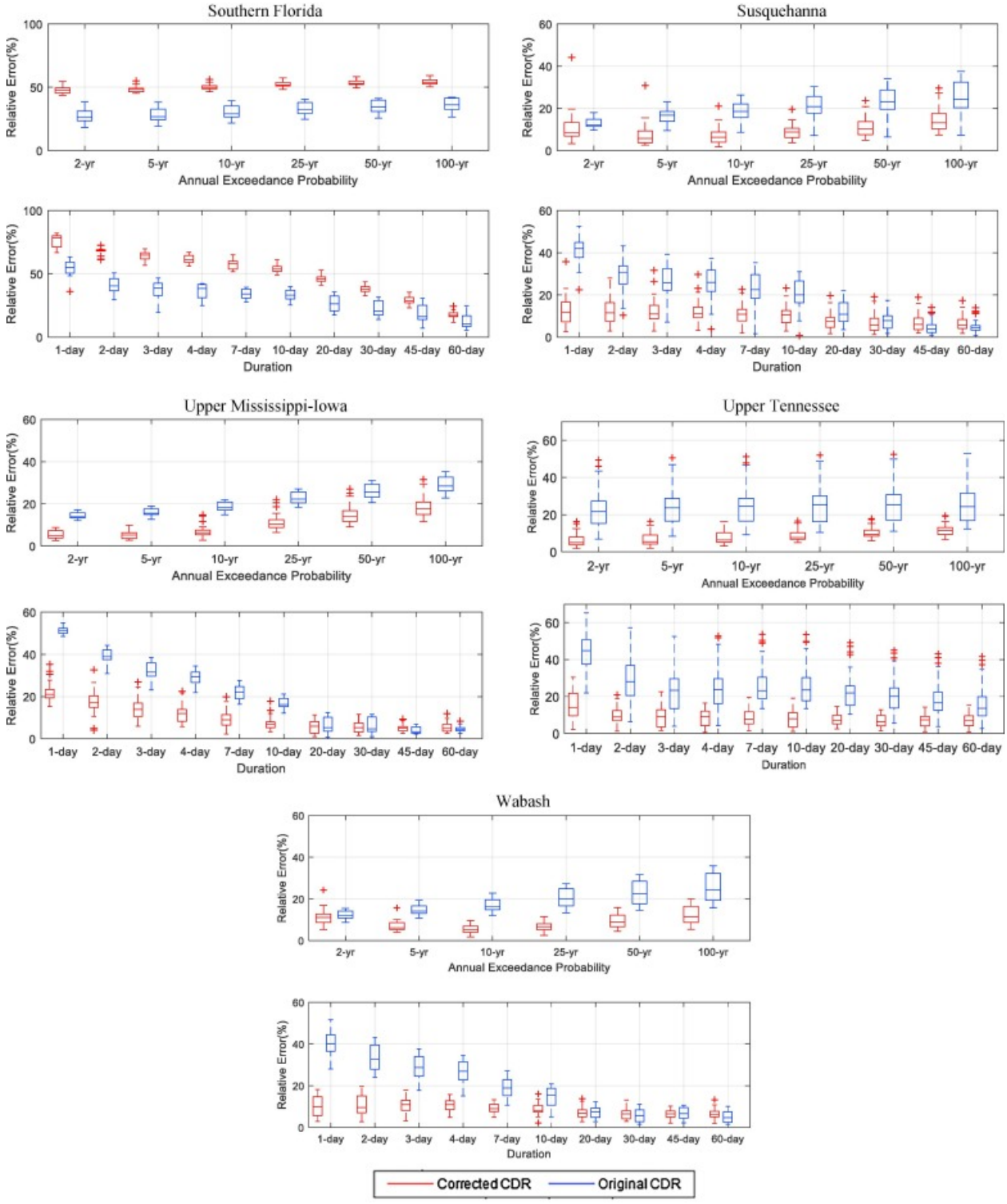

Figure 2.12: Continued

was validated at 16 basins in the continental United States, covering various climates and elevations. Finally, depth-duration-frequency (DDF) curves were constructed by fitting the Generalized Extreme Value distribution to the AMS from the corrected data and estimating the quantiles of extreme precipitations. Below is a summary of our main findings:

1. The proposed bias correction approach has been demonstrated effective and robust in improving the accuracy of a remote sensing precipitation estimation product (i.e., PERSIANN-CDR), especially in high-elevation river basins where gauge or radar networks are either limited or non-existent.

2. The hold-out cross-validation results indicated that the proposed bias correction model is capable of improving the AMS estimated by the PERSIANN-CDR dataset even in the case that limited gauge information was provided for the model calibration and the approach is generalizable to other locations with similar climates and elevations.

3. As shown by the leave-one-out cross-validation, the bias adjusted PERSIANN-CDR gave better estimates of the AMS for the ungauged sites at a majority of the basins even though these basins had dense gauge networks.

4. Results from the k-fold cross-validation method suggested the proposed correction approach performs consistently better than the gauge interpolation method in estimating the AMS at a majority of regions with limited gauge observations. It was observed that the gauge interpolation may sometimes result in significant errors in AMS estimates, especially in regions with complex topography.

5. The validation results over 16 basins across different climates and elevations indicated that the proposed correction method improves the PERSIANN-CDR estimates of AMS, especially in high elevation regions.

6. The bias-adjusted PERSIANN-CDR is further applied to derive the return levels for different return periods and durations. The frequency estimates from the corrected

PERSIANN-CDR data are compared with those from the original PERSIANN-CDR and NOAA Atlas 14. Results revealed that the frequency estimates from the corrected dataset are consistently closer to the estimates from NOAA Atlas 14. They also lie within the uncertainty bounds of NOAA Atlas 14.

Thus, the PERSIANN-CDR dataset has the potential for being used in rainfall frequency analysis for the regions with limited ground-based observations. However, despite the promising results, there are still some limitations in this dataset and the proposed correction method for the application of frequency analysis. One of these limitations is the temporal resolution of the PERSIANN-CDR dataset. The daily temporal resolution limits the investigation of extreme events with shorter durations (e.g. 3-hourly or hourly). Another limitation is that the frequency analysis here is conducted at the pixel scale using relatively limited samples. A sample of 33 annual maximum values is relatively limited for fitting a 3-parameter distribution. This would result in high uncertainties in estimating the parameters of the distribution and the return levels. One remedy to the sample size problem could be the application of regional frequency analysis methods to increase the sample size by incorporating information from the nearby locations with the same climatic conditions.

It is also important to note that given the rising global temperatures, rainfall intensities especially at shorter durations are expected to increase. Therefore, the increase in the global temperature could be used as an added factor to adjust historical design rainfall intensities for the warmer temperatures that lie ahead (Peleg et al., 2018). This work is part of an ongoing research and the presented approaches and results are intended as a proof of concept. Future research in this area may involve, bringing non-stationarities into the bias-adjustment framework (Tao et al., 2018), including covariates into the bias-adjustment framework which requires advanced optimization techniques (Yang et al., 2017; Naeini et al., 2018), investigating the hydrological modeling applications of the corrected-PERSIANN-CDR data, and developing DDF curves for ungauged regions or areas not included in the

current NOAA Atlas 14.

Chapter 3

Spatial Modeling of Extreme Precipitation Using Satellite Information and a Bayesian Hierarchical Framework

3.1 Introduction

Extreme precipitation are often the main cause of flooding and associated risks. Given the societal and economic impacts of floods, extreme precipitation needs to be modeled in fine spatial and temporal resolutions with high accuracy. Appropriate extreme precipitation models are also useful for infrastructure design and management. Due to the sparsity of gauge networks in remote regions, and the limited appearance of extreme events as compared to low or normal intensity precipitations, statistical modeling of hydrological extremes has been a challenging task. In many developing countries, gauge networks are limited in terms

of its lengths, and spatial distribution. This results in high uncertainties in the extreme value models. The model uncertainty will significantly increase as one moves further in the tail of distributions, and it is hard to make inference on the return levels beyond the length of observation records. In recent years, remotely-sensed precipitation information from weather radars and earth-observing satellites have been used for modeling extreme precipitation (Eldardiry et al., 2015; Gado et al., 2017; Marra et al., 2017a; Faridzad et al., 2018; Ombadi et al., 2018; Marra et al., 2019). Such approach has been shown to be effective especially at poorly instrumented regions. However, the remotely sensed precipitation information often suffers from the shortness of data length, which is not desirable for extreme value analysis. A long-term satellite-based precipitation dataset, such as the Precipitation Estimation from Remotely Sensed Information Using Artificial Neural Networks-Climate Data Record(PERSIANN-CDR), is especially of interest for extreme rainfall modeling, given (1) its relatively long record (from 1983 to present), and (2) the high spatial resolution (around 25 km). Yet, the length of the dataset is still limited compared to the return levels often needed to be extrapolated for hydrological applications. Therefore, statistical tools are especially useful to address this issue. However, these statistical tools have to have an adequate flexibility and mathematical foundation to make the extrapolations more reliable (Davison et al., 2012)

A simple approach to model hydrological extremes, is to analyze the tail of distribution at each location independently. That means considering no spatial structure in the model and allowing the data to reveal any spatial similarity through the marginal distributions. This approach has been less desirable for spatial analysis because: (1) the goal of many spatial models is to make inference at ungauged locations, using techniques such as spatial interpolation, which is not easily implemented using an unconnected model; and (2) it is intuitively expected that the precipitation systems affect a cluster of neighboring sites simultaneously and therefore, the adjacent sites are likely to have similar probabilities for extreme events compared to the sites located at far distances from each other. Analyzing individual sites

independently leads to substantially different estimates of probability distributions at adjacent sites, especially when the data length is short. Furthermore, while the point-based analysis could successfully be applied in estimating the mean of the marginal distributions, large uncertainties remain at the tail quantities. Therefore, incorporating spatial dependence structures in the extreme value modeling seems to be a natural choice (Sharkey and Winter, 2017).

Drawing spatial structures in the modeling framework is not a new concept in hydrology. Regional frequency analysis(RFA) is a widely used approach for analyzing spatial extremes (Cunnane, 1988; Sveinsson et al., 2001; Hailegeorgis et al., 2013). RFA aims at pooling information from the sites with a homogeneous statistical behaviour, in order to increase the confidence in parameter estimation (Hosking, 1990; Katz et al., 2002; Hosking and Wallis, 2005). While the RFA approach successfully reduces the uncertainties in the frequency estimates, it adds some restrictive assumptions into the model by defining artificial boundaries for the so-called homogeneous regions. As a result, different parameters and quantiles might be estimated at neighboring sites, and a virtual boundary will be created over the study sites (Sharkey and Winter, 2017). Additionally, RFA does not construct an explicit spatial model for the marginal parameters and also does not model the residual dependence in the data after capturing the marginal behaviour (Cooley et al., 2012).

Bayesian hierarchical approaches are developed and applied with a similar aim to RFA approaches, which are to (1) use information from neighboring sites to generate spatially consistent return level estimates; and (2) reduce uncertainties in the frequency estimates according to Banerjee et al. (2004). The Bayesian hierarchical approaches offer several advantages to the conventional frequency analysis methods. Frequency analyses are often hampered by data scarcity issue; therefore, parameter estimation methods, such as maximum likelihood estimation(MLE), often cannot fully capture the tail behavior of the data. Bayesian methods have the advantage incorporating expert knowledge to enhance the con-

vergence of the model through the use of prior information. Additionally, these methods are inclusive to additional spatial and temporal information (i.e., covariates), such as geographical and meteorological information. Furthermore, unlike the other ad-hoc uncertainty estimation methods (e.g., bootstrapping technique) (Tao et al., 2018) used in the conventional approaches, the Bayesian paradigm explicitly quantifies the uncertainties in the model parameters and predictions (Cooley et al., 2007). In recent years, various Bayesian hierarchical approaches have been proposed for modeling extreme values and used in hydrological applications (Cooley et al., 2007; Renard, 2011; Shaby and Reich, 2012; Ribatet et al., 2012; Sharkey and Winter, 2017). For instance, Reich and Shaby (2012) proposed a random effect model with a Gaussian extreme value process(GEVP) as a limiting case and used this model to analyze the annual maximum precipitation from a regional climate model. Cooley and Sain (2010) used a multivariate intrinsic autoregressive (IAR) model to analyze extreme precipitation from a regional climate model. Among the hierarchical approaches, the latent variable model (LVM) proposed by Davison et al. (2012) has been shown to be an effective method for capturing the marginal behavior of the extreme rainfall data. Sebille et al. (2017) compared various methods for modeling spatial extremes and observed that the LVM has the best robustness and reliability in extrapolating the return levels.

In this study, the PERSIANN-CDR dataset has been used in a Bayesian hierarchical modeling framework, to spatially model extreme precipitation in the state of Washington in the Unites States. The state of Washington was chosen since it is among the few states that its frequency estimates have not been updated in the recent frequency atlas of the United States. The LVM approach was chosen among the hierarchical approaches given its robust performance in extrapolating the return levels. In the first part of this paper, we explore the necessity of the spatial modeling of extreme precipitations over this region. Then, the applied hierarchical model and the performance evaluation criteria will be described in details. Finally, results of the constructed model are presented and evaluated.

The rest of this chapter is organized as follows: in section 2, the applied dataset and the studied region are introduced. The employed methodologies are explained in section 3. Results of the study are presented and discussed in Section 4. Finally, the main findings and conclusions are given in section 5.

3.2 Data and Study Area

3.2.1 Study Area

The study area of this chapter is a rectangular region which includes the state of Washington. The corresponding coordinates of this rectangular region are $124°75'W$ to $116°30'W$, and $45°30'N$ to $49°30'N$ (Figure 4.1).

In this chapter, we use the PERSIANN-CDR data to model the spatial extremes over the study domain. Each PERSIANN-CDR pixel within the study boundary is treated as a rain gauge located at the centroid of the respective grid-box(Figure 4.1b). Also, the altitude of each gauge is calculated in a similar fashion using the DEM layer.

3.2.2 Bias-corrected PERSIANN-CDR data

In this chapter, the input data for the spatial extreme value model is the bias-corrected Annual Maximum time Series (AMS) of precipitation obtained at each pixel of the PERSIANN-CDR dataset. In other words, each of the PERSIANN-CDR pixels over the study region are treated as a rain gauge with 35 years of observation which their estimates are bias-corrected, separately. The biases in the AMS at each pixel were corrected using the method proposed by Faridzad et al. (2018). According to this method, the AMS at each pixel is corrected using a regression function, which gives a correction factor based on the elevation of the lo-

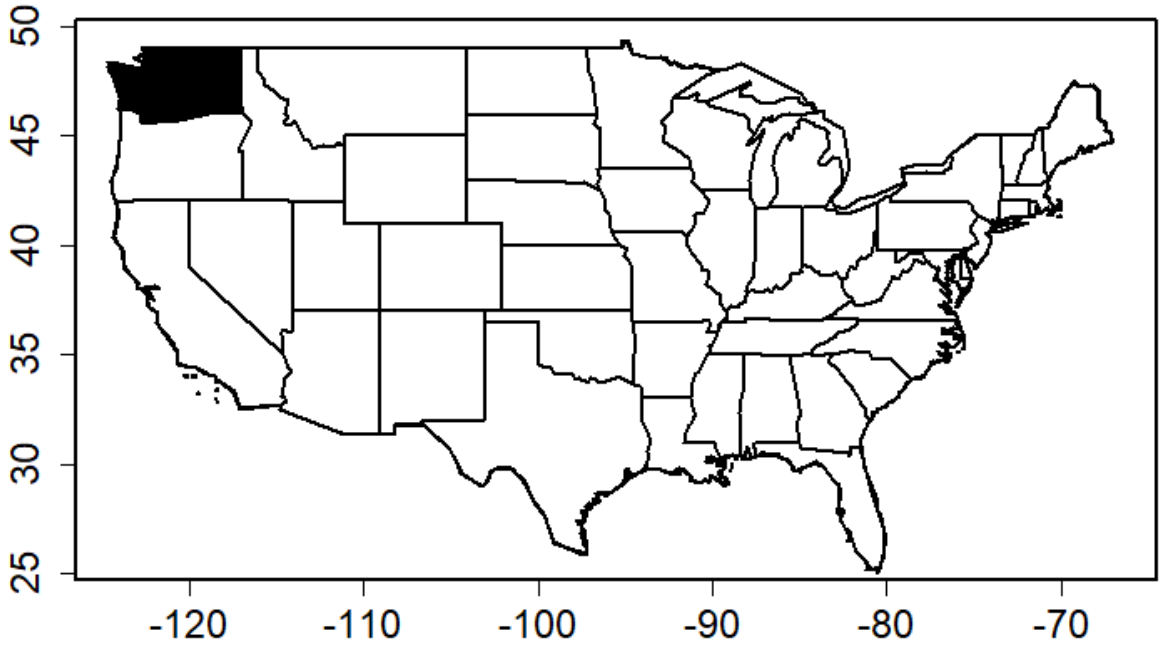

(a)

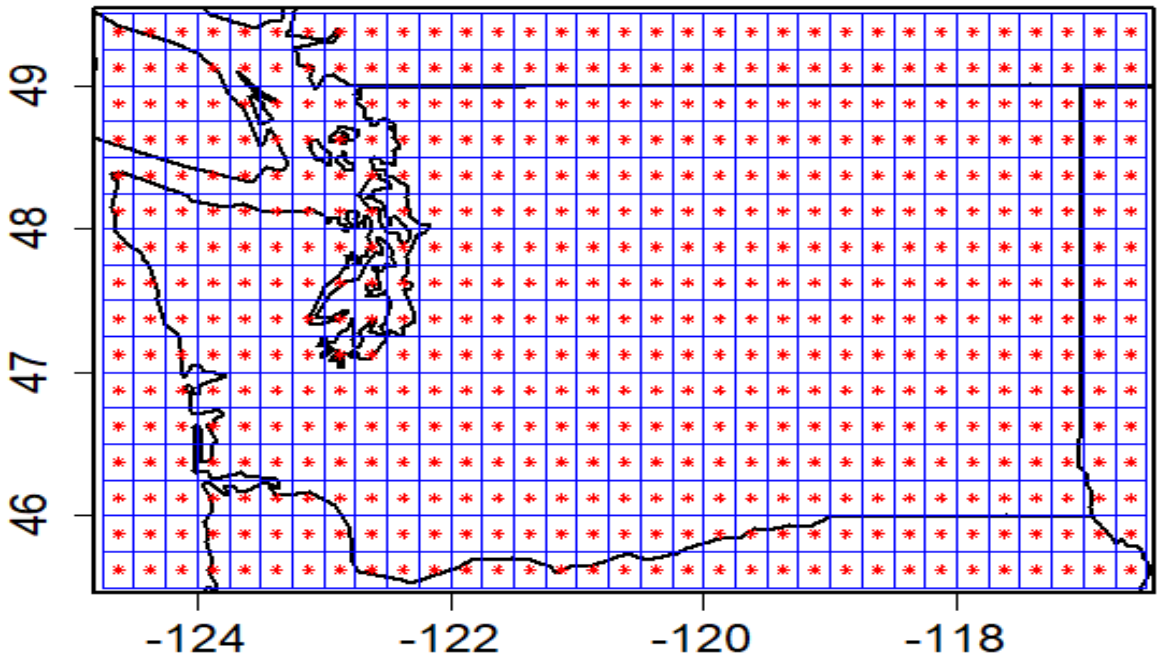

(b)

Figure 3.1: (a) Map of the Contiguous United States and the location of Washington state; and (b) map of the Washington state along with the location of PERSIANN-CDR pixels. The blue grid lines show the boundaries of PERSIANN-CDR and DEM pixels and the red asterisks denote the centroid of each grid box

cation. The applied correction function is $C.F. = 2.4855 \times elevation^{-0.215}$;where, $C.F$ is the correction factor for the AMS at each pixel. This method was shown effective in reducing the biases in the extreme precipitation estimates by the PERSIANN-CDR product and resulted in the similar frequency estimates to that of the gauge-based frequency Atlas of the United States (Faridzad et al., 2018). The elevation data used for the bias-correction procedure is described in the following subsection.

3.2.3 Digital elevation model(DEM)

In this study, the purpose of using elevation information was two fold: (1) it was used in the bias-correction procedure of the PERSIANN-CDR data; and (2) as an additional spatial covariate for the spatial extreme value model. In order to keep the consistency with the precipitation dataset,a digital elevation model(DEM) with spatial resolution of 0.25° (∼ 25 km) developed by NOAA was obtained and used (Figure 4.2a). This dataset can be downloaded from: http://research.jisao.washington. edu/data_sets/elevation/

3.3 Methodology

3.3.1 Extreme Value Theory

Hydrological extremes are often modeled using the 3-parameter Generalized Extreme Value(GEV) distribution (Jenkinson, 1955). Let $\boldsymbol{S}$ represent the spatial domain of interest. The random variable $Y(\cdot) = Y(s)_{s \in S}$ follows a GEV distribution $Y(s) \sim GEV(\mu(s), \sigma(s), \xi(s))$ where the location $\mu(s) \in \mathbb{R}$, the scale $\sigma(s) > 0$, and the shape $\xi(s) \in \mathbb{R}$ parameters are indexed over the spatial domain $\boldsymbol{S}$. The cumulative distribution function(cdf) of a GEV random variable

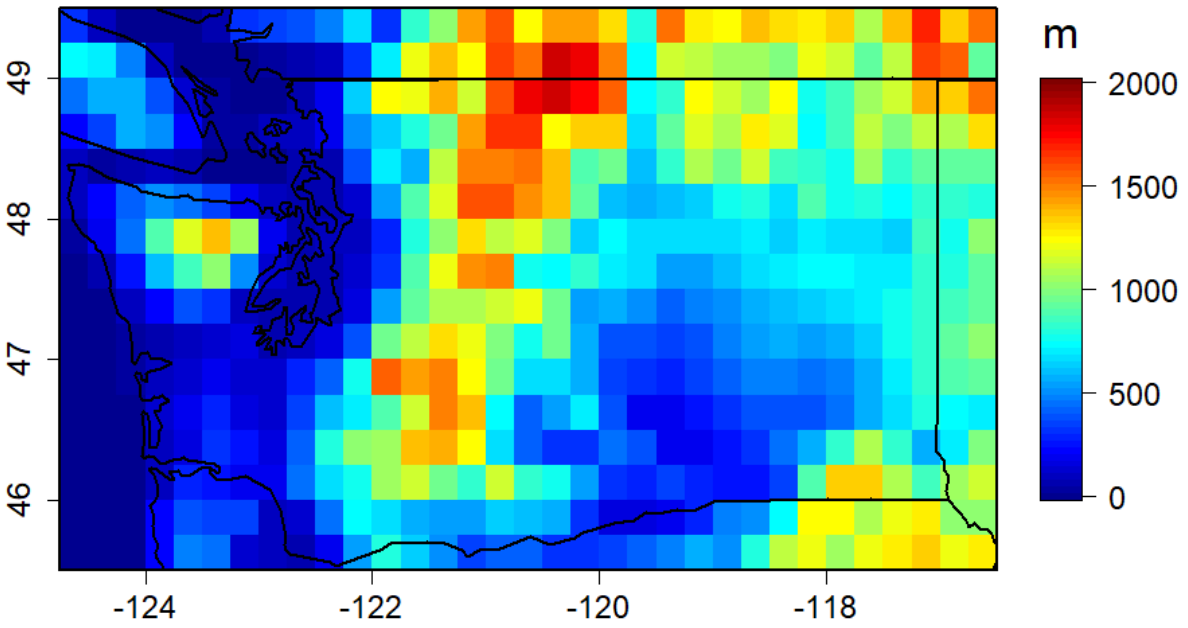

(a)

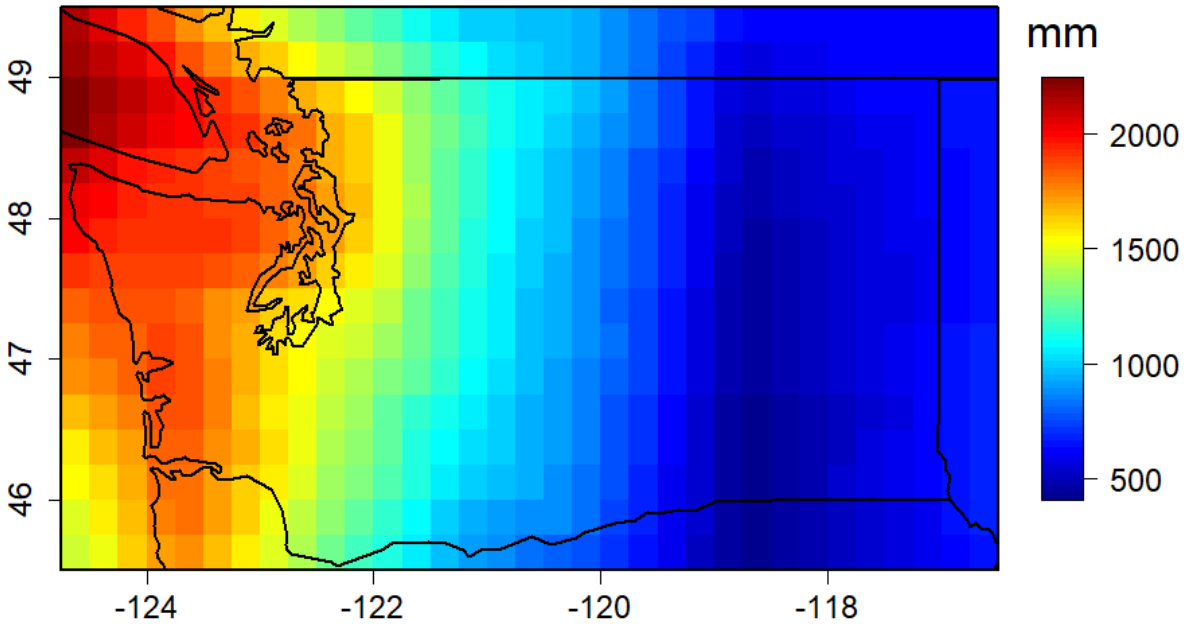

(b)

Figure 3.2: (a) Elevation map of Washington state; and (b) Map of the mean annual precipitation over Washington state from PERSIANN-CDR data

is given by equation (4.12)

$$F(y) = \begin{cases} exp\left(-\left[1+\xi\frac{y-\mu}{\sigma}\right]^{-\frac{1}{\xi}}\right) & \text{if} \quad \xi \neq 0 \\ exp\left(-exp\left[\frac{y-\mu}{\sigma}\right]\right) & \text{if} \quad \xi = 0 \end{cases} \tag{3.1}$$

The shape parameter characterizes the tail behavior of the GEV distribution, with $\xi < 0$ corresponding to the reverse Weibull case with a finite upper bound, $\xi = 0$ corresponding to the light-tailed Gumbel distribution, and $\xi > 0$ corresponding to the heavy-tailed Fréchet distribution.

3.3.2 Hierarchical Modeling and Latent Variable Model (LVM)

Hierarchical Bayesian models generally assume that the spatial process $Y(\cdot)$ is independent conditionally on the latent variables. Different types of hierarchical models are thoroughly discussed by Banerjee et al. (2004). Hierarchical models are typically constructed within the Bayesian paradigm. Markov Chain Monte Carlo (MCMC) algorithm is often used in such modeling framework to make inference on the posterior distribution of the parameters given the data.

Dependence in many statistical applications is considered through integration over underlying processes or variables (Davison et al., 2012). The same idea can be used to allow for spatial variation in the parameters. For instance, we can assume that the response variables $Y(s)_{s\in S}$(which are the maxima data), are independent conditionally on an unobserved latent process. The parameters of the response distributions depend on $\varepsilon(s)$, and $\varepsilon(\cdot)$ follows a Gaussian process. Dependence in the response variables is then introduced by integration

over the latent process (Davison et al., 2012). This framework is common in geostatistics with non-normal random variables (Diggle et al., 1998) and due to the complexity of the related integrations, it is normally implemented using a Bayesian approach with the Markov chain Monte Carlo method being applied for inference (Hastings, 1970; Coles and Casson, 1998; Fawcett and Walshaw, 2006; Turkman et al., 2010; Robert and Casella, 2013).

Based on this idea, Davison et al. (2012) proposed a hierarchical modeling framework for the spatial extremes, called the latent variable model(LVM). In the LVM approach, the random variables(or the response variables) $Y(s)_{s\in S}$ are assumed to be independent, conditionally on the unobserved latent processes underlying the GEV parameters. This model can be formulated as:

$$Y(s)|\left\{\mu,\sigma,\xi\right\} \overset{indep}{\sim} GEV\left(\mu(s),\sigma(s),\xi(s)\right)$$

$$\begin{cases} \mu(s) = \beta_{\mu}^{T} c(s) + \varepsilon_{\mu}(s) \\ \sigma(s) = \beta_{\sigma}^{T} c(s) + \varepsilon_{\sigma}(s) \\ \xi(s) = \beta_{\xi}^{T} c(s) + \varepsilon_{\xi}(s) \end{cases} \tag{3.2}$$

where $\varepsilon(\cdot)$ represents the spatial random processes with independent stationary zero-mean Gaussian processes with covariance function $\alpha \exp(-\|h\|/\lambda)$ with unknown sill(α) and range(λ) parameters, h denotes the Euclidean distance between s_1 and s_2, and $c(\cdot)$ denotes the spatial covariates associated with the location $s \in S$. In our modeling scheme,we considered spatial variability for all of the GEV parameters. In other words, the location $\mu(\cdot)$, the scale $\sigma(\cdot)$, and the shape $\xi(\cdot)$ parameters are assumed to be linear combinations of the covariates with unknown vector of coefficients β_{μ}, β_{σ}, and β_{ξ}, respectively.

Typically, one would prefer covariates that are known at all gauged and ungauged locations. Often, latitude and longitude are the only available options for such covariates. The

covariates we considered in this study are latitude, longitude, and altitude. The values of these covariates were computed for the centroids of the PERSIANN-CDR(resp. DEM) grid boxes(Figure4.1(b)).

3.3.3 Inference Procedure for The Latent Variable Model

Inference for the hierarchical models is usually implemented in a Bayesian framework. MCMC algorithm is employed to draw parameters from their posterior distributions using Metropolis-Hastings steps within a Gibbs sampler.

According to Davison et al. (2012), a joint prior density must be defined for α, λ, and β parameters. Whenever possible, conjugate priors (i.e. priors that give a close-formed expression for the posterior distribution; otherwise numerical integration will be required) were considered to alleviate the computational complexity. Therefore, independent inverse Gamma and multivariate Gaussian distributions were considered for α and β, respectively. For λ, an uninformative Gamma distribution was considered as the prior, given the unavailability of a conjugate prior distribution. Prior distributions for all of the GEV parameters were considered similarly. Then, conditional on the values of the Gaussian processes for each GEV parameter at each site (s_1,...,s_d), the maxima are assumed to be independent.

$$Y_i(s_d)|\left\{\mu(s_d),\sigma(s_d),\xi(s_d)\right\} \sim GEV\left\{\mu(s),\sigma(s),\xi(s)\right\}, i=1,...,n; d=1,...,D \tag{3.3}$$

For the LVM model, the full conditional distribution required for the Markov chain Monte Carlo estimation of the posterior distributions are as follows:

$$
\begin{aligned}
&\pi(\mu|...) \propto \pi(\mu|\alpha_\mu, \lambda_\mu, \beta_\mu)\pi(y|\mu, \sigma, \xi) \\
&\pi(\alpha_\mu|...) \propto \pi(\alpha_\mu|\kappa^*_{\alpha_\mu}, \theta^*_{\alpha_\mu})\pi(\mu|\alpha_\mu, \lambda_\mu, \beta_\mu) \\
&\pi(\lambda_\mu|...) \propto \pi(\lambda_\mu|\kappa^*_{\lambda_\mu}, \theta^*_{\lambda_\mu})\pi(\mu|\alpha_\mu, \lambda_\mu, \beta_\mu) \\
&\pi(\beta_\mu|...) \propto \pi(\beta_\mu|\psi^*_\mu, \Sigma^*_\mu)\pi(\mu|\alpha_\mu, \lambda_\mu, \beta_\mu)
\end{aligned}
\tag{3.4}
$$

where $\propto$ implies the proportionality, κ^*, θ^*, ψ^*, and Σ^* refer to the hyperparameters pf the prior distributions. The full conditional distributions for the other two parameters of the GEV distribution (σ and ξ) are calculated in a similar fashion.

In this work, the fitting procedure of the LVM model has been implemented in some parts using the `hkevp` (Sebille, 2016) package in R environment (R Core Team, 2013). Metropolis within Gibbs algorithm was used to to make inference on the posterior distribution of the GEV parameters as Markov chains. The MCMC algorithm was implemented for 300,000 iterations, with the first 5,000 iterations considered as burn-in samples. In order to minimize the autocorrelation, a thinning interval of 10 was considered. In other words, from each 10 posterior samples generated by the MCMC algorithm, only one sample is retained. Thus, the resulting Markov chains have the length of 29,500. Furthermore, the mean of the relevant chains were considered whenever point-wise estimates were required. It is worthwhile mentioning that we applied the discussed methods on the block maxima data because the available methodologies for the spatial extreme value analysis are mostly developed for the annual maxima data. Working with the peaks over threshold could provide more flexibility

to the Bayesian inference (Coles and Tawn, 1991).

3.4 Results

3.4.1 Exploratory Analysis

An exploratory analysis has been performed to investigate the need for utilizing a spatial model for extreme value analysis for our study domain. The exploratory tool applied here are symbol plots. The symbol plots depict the spatial distribution of each of the GEV parameters in the study region 3.3. The GEV parameter values showed here are point-wise estimates(without considering any spatial structure) based on maximum-likelihood method. The circles coincide with the PERSIANN-CDR pixels. The radius of each circle is proportional to the deviation of the parameter value at that location from the areal mean value computed over the study region. Also, red(blue) color signifies a positive(negative) deviation. As shown in this figure, there is a clear spatial pattern for the location(μ) and the scale(σ) parameters, with larger values in the Western areas and smaller values in the Eastern areas of the study region. This pattern is similar to the annual precipitation pattern over this region(Figure 4.2b) where more intense rainfall events occur over the Western areas as opposed to the Eastern part.

For the shape parameter of the GEV distribution(Figure3.3c), it is difficult to detect any spatial pattern. The shape parameter (ξ) which characterizes the tail behaviour of the GEV distribution, does not usually demonstrate any spatial pattern when dealing with precipitation data.

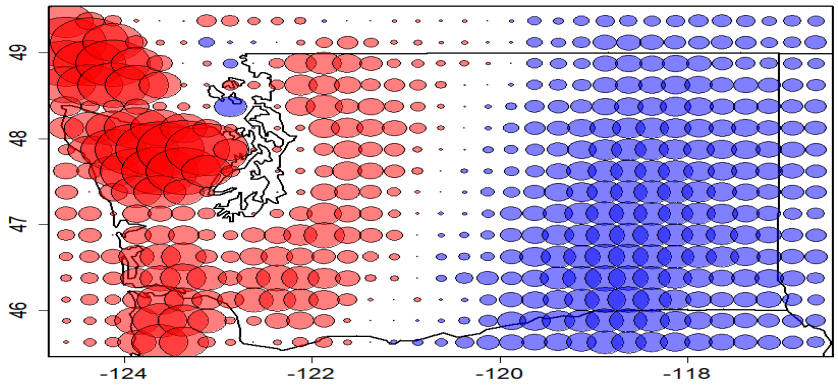

(a) location parameter (μ)

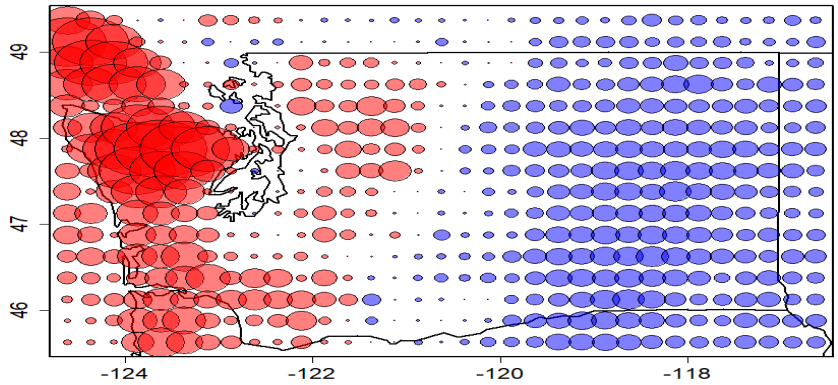

(b) scale parameter (σ)

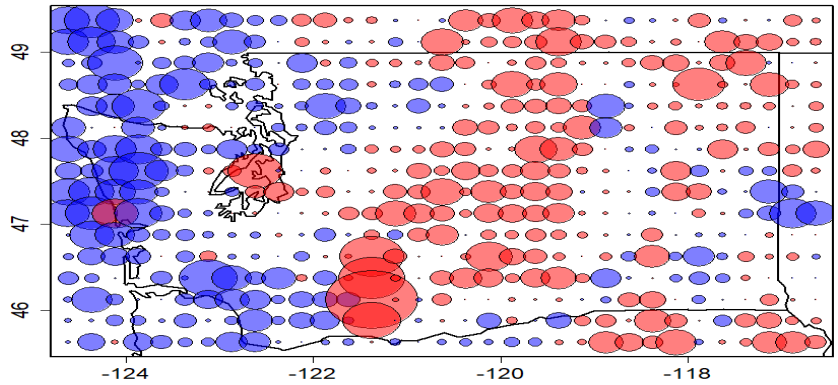

(c) shape parameter (ξ)

Figure 3.3: Symbol plot displaying the spatial pattern of point-wise estimates of GEV parameters: a) location (μ) , b) scale (σ), and c) shape (ξ) over the Washington State. The radius of the circle at each location is proportional to the departure of the parameter value at that location to the areal mean value.

3.4.2 Bayesian Model Diagnostics

Before using the simulated Markov chains to obtain Monte Carlo estimates of the GEV parameters, we need to first assess the convergence of the simulated Markov Chains to their stationary distributions. In this study, two model diagnostics measures are used to evaluate the convergence of the Markov Chains. The applied diagnostics are trace plots and autocorrelation plots.

Traceplots

The first visual tool employed to assess the convergence of the LVM model are the traceplots which show the history of the parameter values across the iterations of the chains. If the average value of a chain has become roughly flat, it shows that the parameter value has converged. Otherwise, if there is a long term trend in the chain values, or the mean value changes across iterations, the chain has to continue running for more iterations until it becomes stationary.

Figure 3.4 shows the traceplots of the location, scale, and shape parameters of the GEV distribution along with the log-likelihood of the LVM model. As shown in this figure, all the parameter chains have converged to their stationary distributions and their mean values have become almost constant. A similar pattern is observed for the log-likelihood of the model. Therefore, based on this diagnostic, the model seems to be converged successfully.

Autocorrelation

Autocorrelation shows how much the current value of a Markov Chain depends linearly on the previous chain values with various amounts of lag. If by going further along the chain, the values become much less correlated, then the chain has most likely converged to its stationary

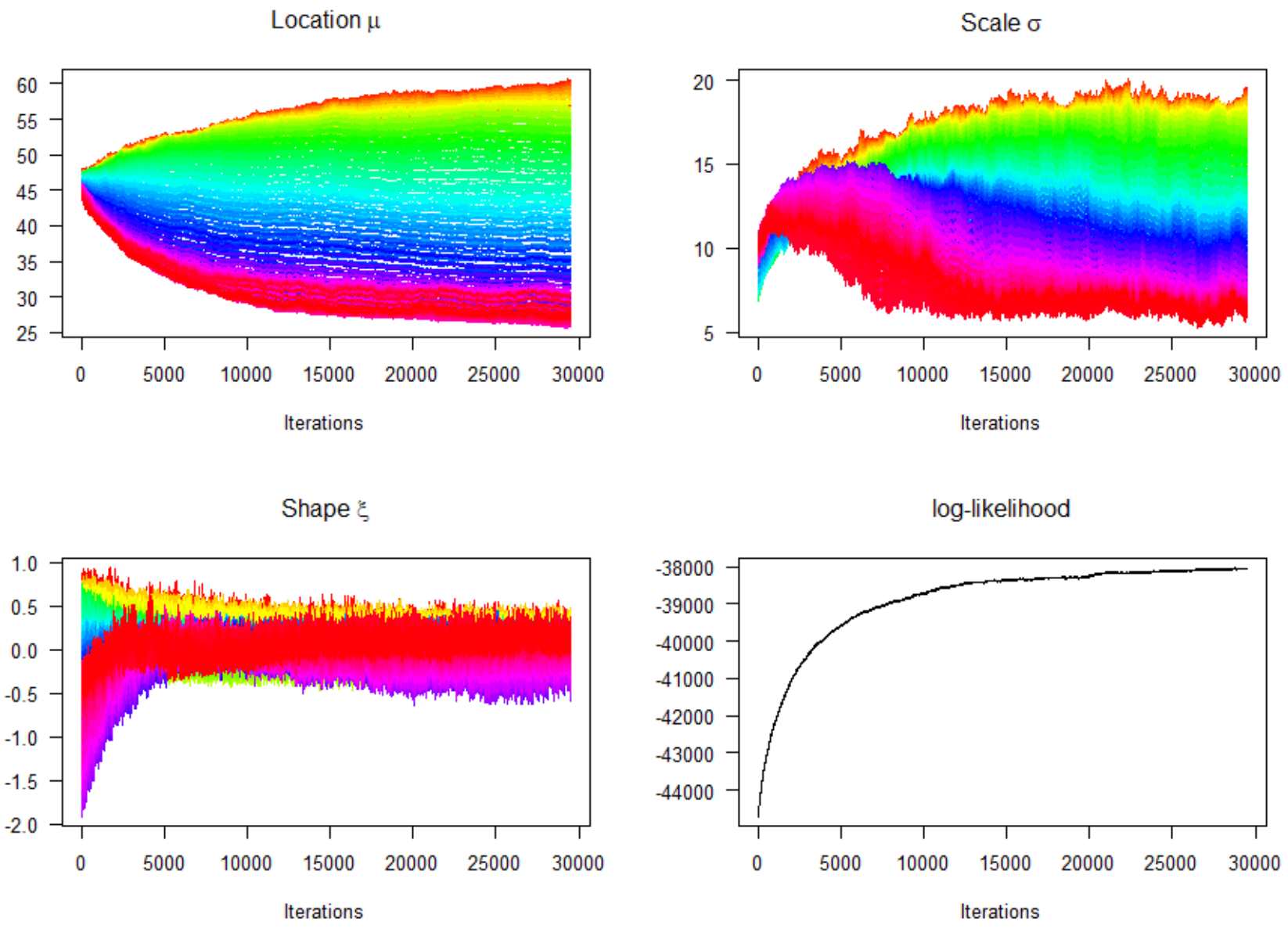

Figure 3.4: Traceplots of the generated Markov chains for the GEV parameters and the log-likelihood values across the model iterations

distribution. But, if after several lags, the chain values are still highly correlated, then the sampling from the posterior distribution should continue for many more iterations so that the posterior distribution of the parameters are fully explored. Therefore, autocorrelation is a measure of the available information in the Markov Chains. An acceptable Markov Chain is a chain that its autocorrelation values converge to zero after a number of lags.

Figure 3.5 demonstrates the autocorrelation plots for the Markov chains of the three parameters of the GEV distribution(μ, σ, ξ) as estimated by the LVM model. According to the results, the autocorrelation converges to near zero after a few lags. Therefore, the thinning interval and the step size considered for the model are reasonable values that result in the suitable simulation of the posterior distribution of the GEV parameters.

3.4.3 GEV Parameters

Spatial distribution of location(μ), scale(σ), and shape(ξ) parameters of GEV distribution estimated by LVM model are depicted in figure 3.6. The spatial pattern of $\mu(x)$ seems reasonable, with decrease in the values as longitude increases, which corresponds to the overall altitude reduction away from the Coastal ranges and also decrease in precipitation (Figure 4.2b). A similar spatial pattern is observed for the scale parameter. This spatial pattern is largely dictated by the moisture regime and the heavy orographic precipitation pattern in this state which is also reflected in the spatial pattern of the annual precipitation. For the shape parameter, a similar East-ward reduction pattern exists. However, this pattern seems to be mostly influenced by altitude, where higher values are observed near the high-elevation areas near the Western parts of the state. The small positive shape parameter values correspond to the heavy-tailed and right-skewed Fréchet distribution with no upper bound which is often the case for the extreme precipitation data.

In order to further explore the behaviour of the shape parameter with respect to the model

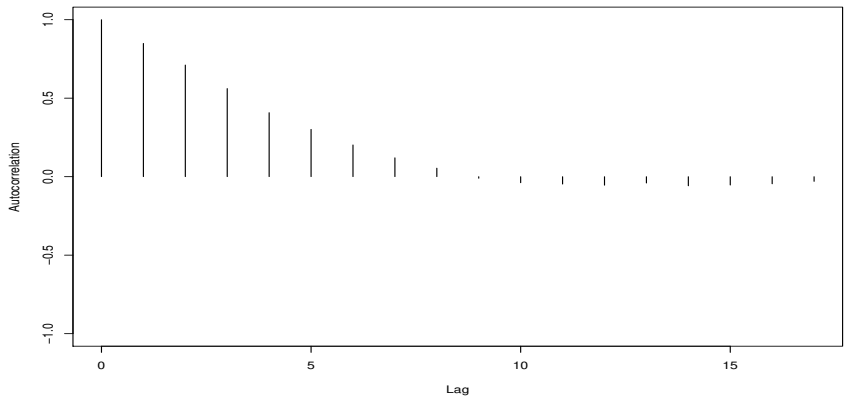

(a) location parameter (μ)

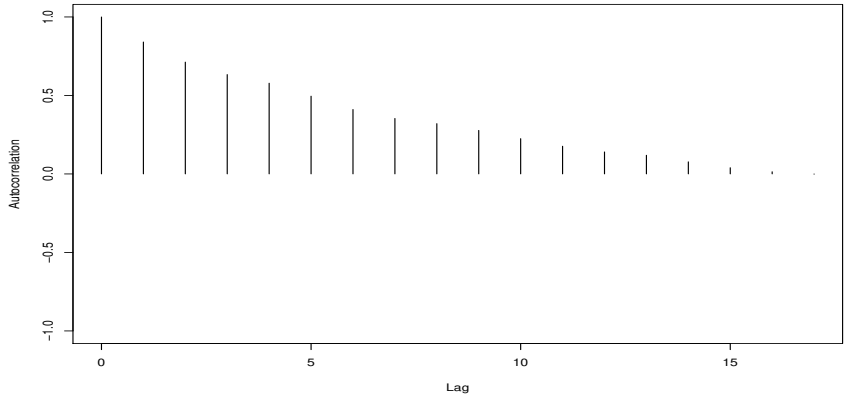

(b) scale parameter (σ)

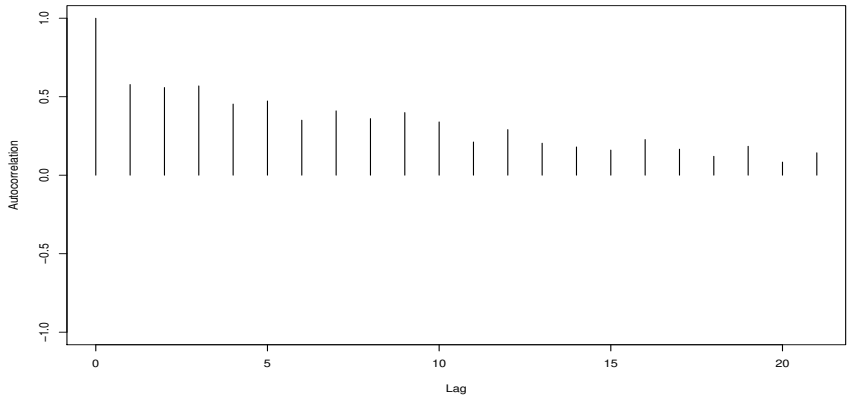

(c) shape parameter (ξ)

Figure 3.5: Autocorrelation plots of the GEV parameters generated across iterations of the Markov chains

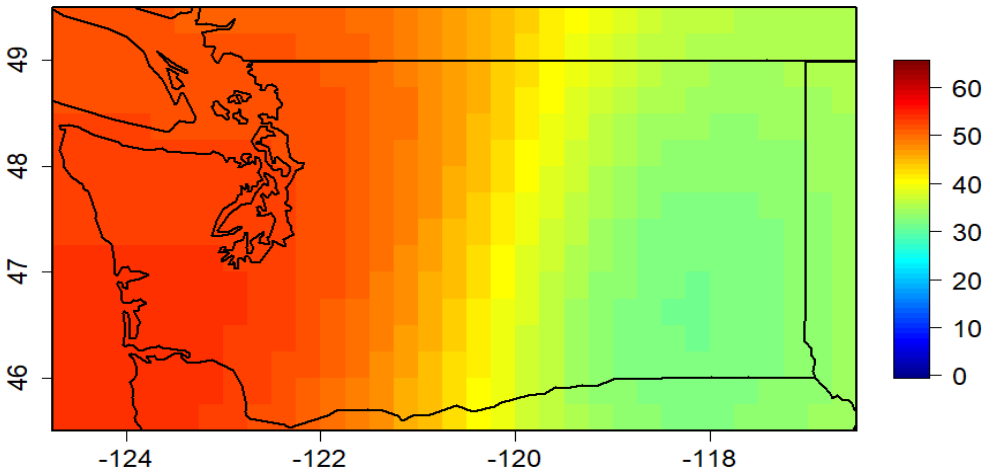

(a) location parameter (μ)

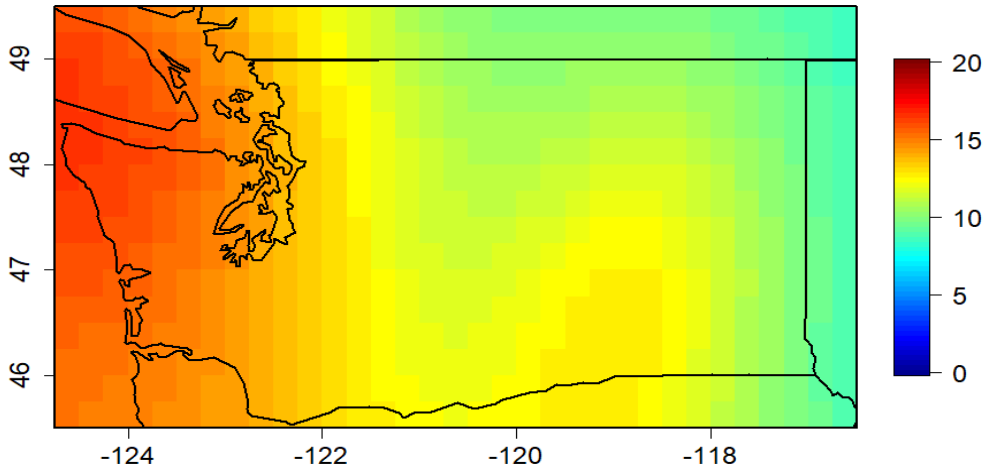

(b) scale parameter (σ)

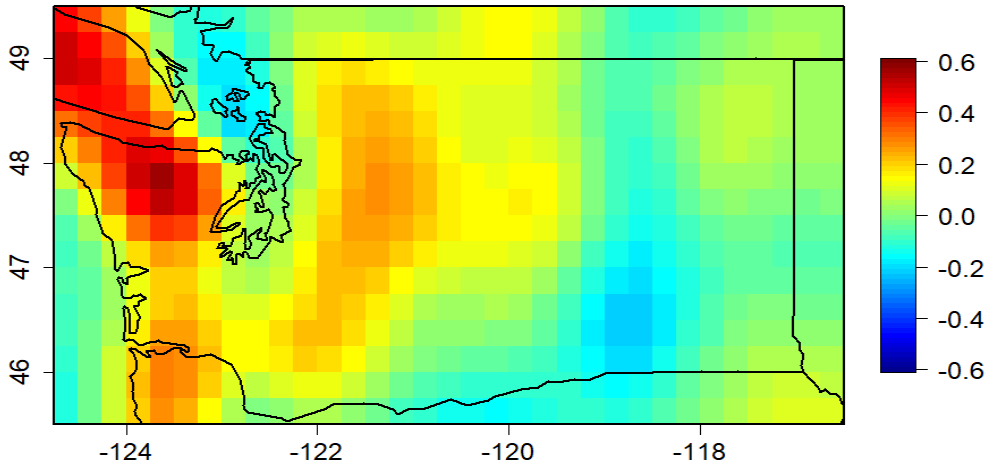

(c) shape parameter (ξ)

Figure 3.6: Spatial distribution of the GEV parameters estimated by the LVM model

covariates, scatterplots of the shape parameter with respect to the model covariates at the corresponding pixels are shown (Figure 3.7). According to this figure, there is no clear relationship between the shape parameter values and latitude over the studied region. With respect to the longitude covariate, there is a general west-east gradient in the shape parameter values with larger values over the west and smaller values over eastern parts of the study domain. This pattern seems to be mostly related to the general precipitation pattern in the state of Washington, where more intense rainfalls occur near the coastal areas in the western parts. Scatterplot of shape parameter and altitude covariate also demonstrate a relative direct relationship between the two variables. In other words, generally larger shape parameter values are observed in high-elevation regions as opposed to low elevation parts. Yet, it is observed that the greatest shape parameter values coincide with the low-elevation regions over the northwest Washington where the mean annual precipitation is the highest (Figure 4.2b).

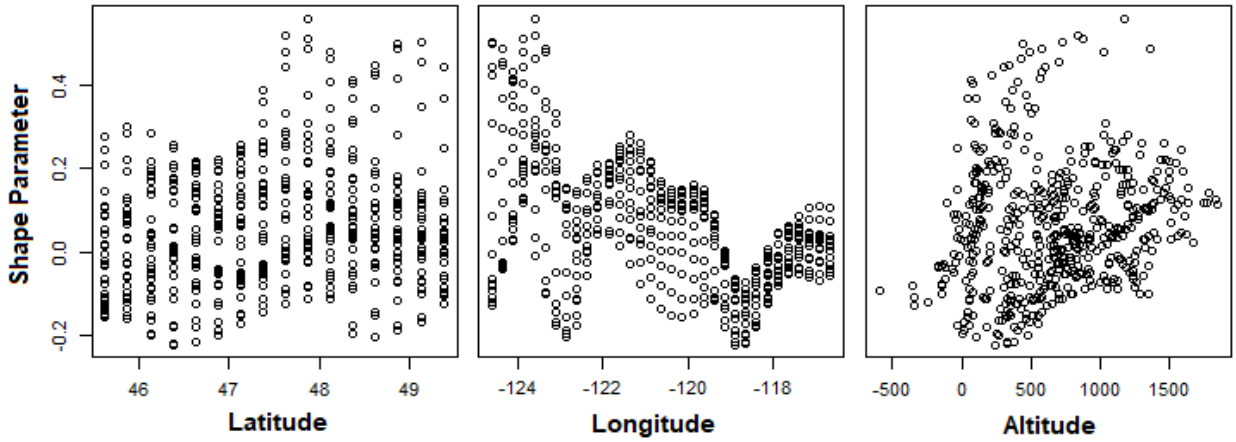

Figure 3.7: Scatterplots of the GEV shape parameter estimated over Washington state versus various model covariates

The observed pattern in the values of the shape parameter with respect to the covariates, are more justifiable when looking at the same plots for the mean daily precipitation (Figure 3.8). As shown in Figure 3.8, there is a clear west-east gradient in the mean daily precipitation values over the study domain. Also, The scatterplot of mean daily precipitation and altitude seems to have two main clusters. One cluster belongs to the low-elevation regions in the

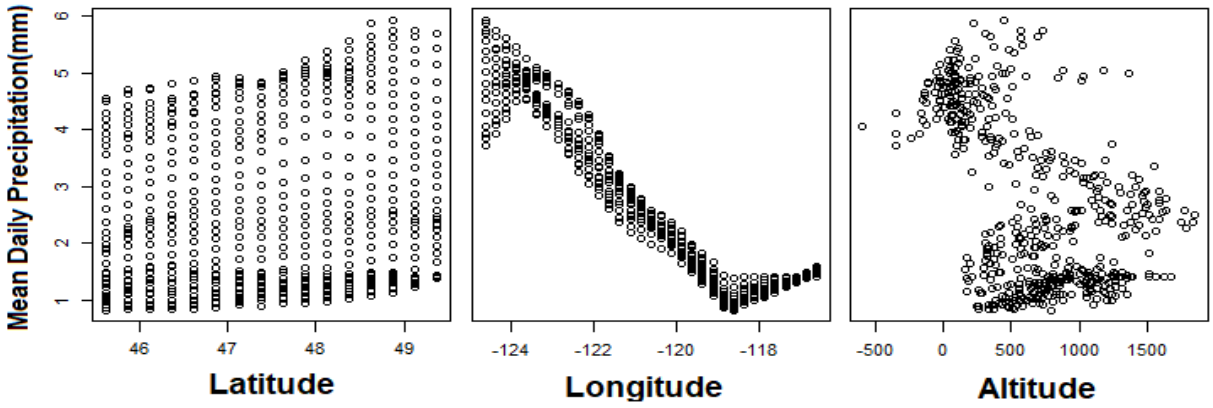

Figure 3.8: Scatterplots of mean daily precipitation over Washington state versus latitude, longitude, and altitude

western areas of Washington with large amounts of precipitation. The second cluster displays a slight direct relationship between mean daily precipitation and altitude, which is reasonable given the orographic precipitation mechanism in the mountainous areas of Washington state.

3.4.4 Extreme Quantiles

Spatial return level maps of the 25-year, 50-year, 75-year, and 100-year extreme events are displayed in Figure 3.9. The presented figures show the predictive point-wise posterior mean values for the mentioned return levels at each of the PERSIANN-CDR pixels. As seen in this figure, the spatial pattern of the estimated extreme quantiles agrees well with each other. There is a clear spatial pattern in the extreme precipitation quantiles with more intense extremes in the western areas and less intense events in the eastern areas of the state. The observed spatial pattern, which is similar to the mean annual precipitation pattern and the topography of the state (figure 4.2) can be largely explained by the moist air regime over this region.

The moist air travelling inland from over the Pacific Ocean is the primary source of moisture required for precipitation occurrence for the state of Washington. Two major releases of

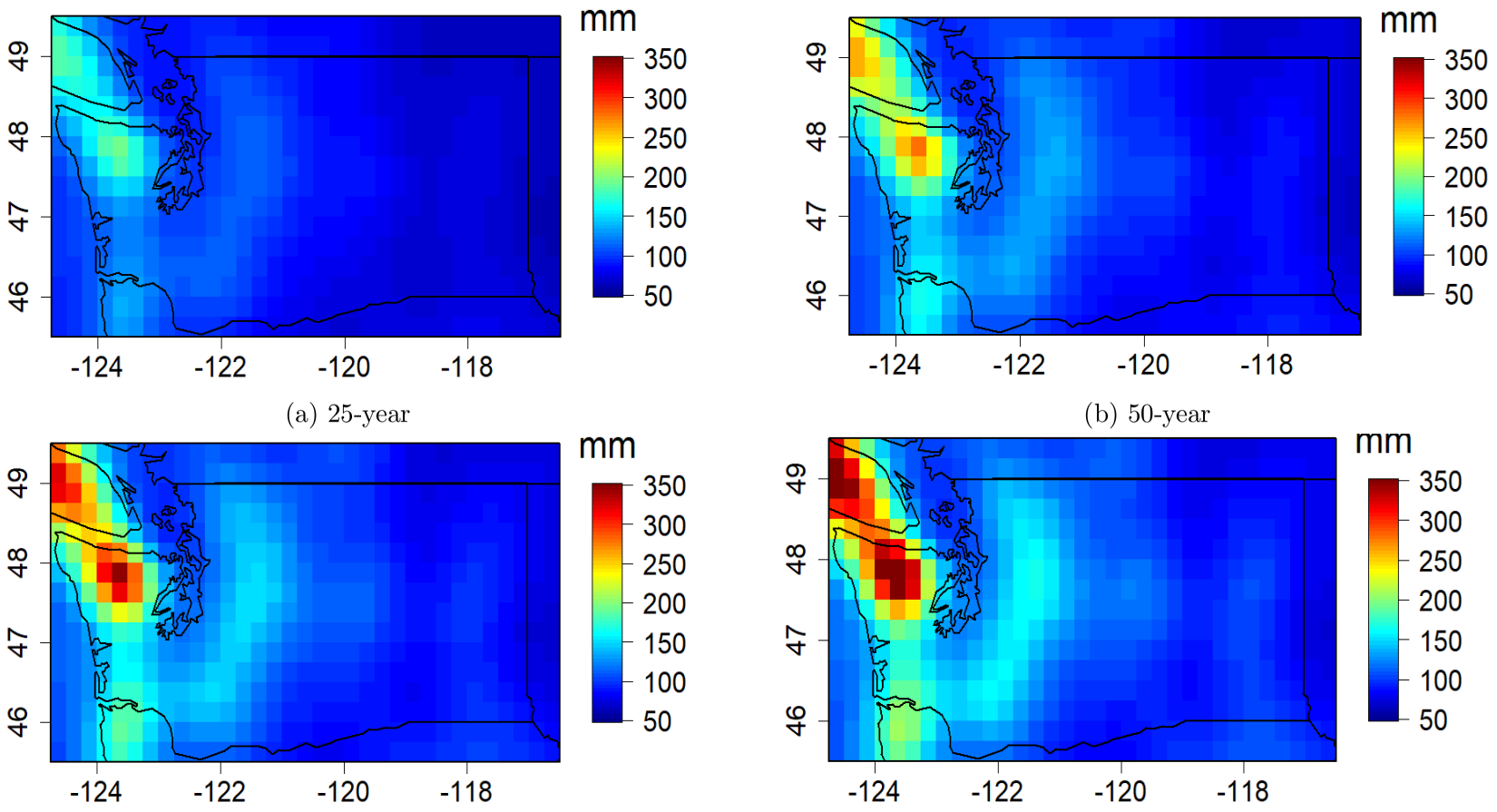

(a) 25-year

(b) 50-year

(c) 75-year

(d) 100-year

Figure 3.9: Maps of the extrapolated return levels of precipitation estimated by LVM model

moisture with heavy orographic precipitations occur at the mountain ranges parallel to the coast. The first release happens at the Western slopes of the Coastal Mountain Range and the Olympia Mountains, where the orographic lifting mechanism results in heavy precipitations in the windward side of the coastal mountains. The effect of this phenomenon is clearly depicted in Figure 9 as larger extremes are computed for the Western and the Northwestern areas of the state. The second release of moisture takes place after a similar orographic lifting mechanism along the Western slopes of the Cascade mountain range. Thus, extreme precipitations take place in the central areas of the state in the windward side of the Cascade Mountain Range. The Cascade Mountain range, acts as a topographic barrier across the central areas of the basin and prevents the passage of moist air to the Columbia basin and the Eastern parts of the state and results in desert conditions in the lowlands of Columbia Basin.

3.4.5 Satellite-based Depth-Duration-Frequency Curves

One practical application of the extreme precipitation models is the derivation of depth-duration-frequency (DDF) curves, which are widely used in hydrologic designs. Figure 3.10 displays the DDF curves of daily extremes along with the standard error of the estimates for four randomly selected locations over the state of Washington. Locations 1 and 2 are located over the western areas of the state of Washington, where more intense extremes take place. Less intense extremes are observed over the central and eastern parts of the state (Figure 3.9) , which is also reflected in the DDF curves for locations 3 and 4.

Figure 3.10 also depicts the standard errors of the generated DDF curves. The standard errors of the return level estimates become larger with increasing return periods. This higher uncertainty is because of the smaller sample size at the tails of the distribution. Also, it is worth mentioning that the confidence interval is estimated by calculating the standard error

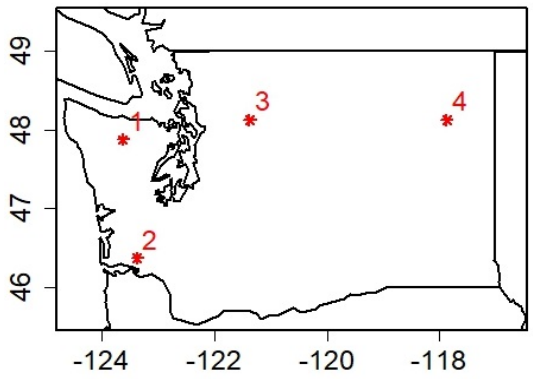

(a) Spatial distribution of the selected locations

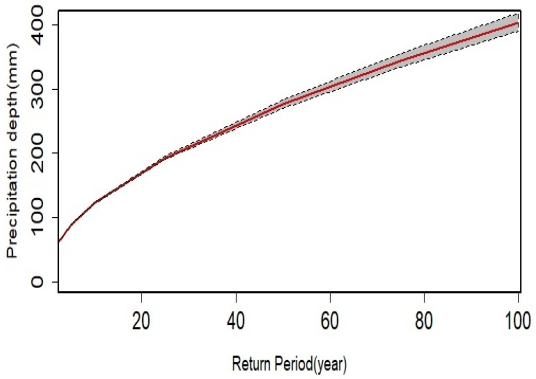

(b) Location No. 1

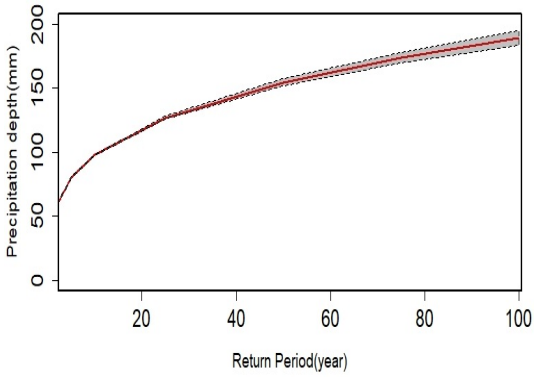

(c) Location No. 2

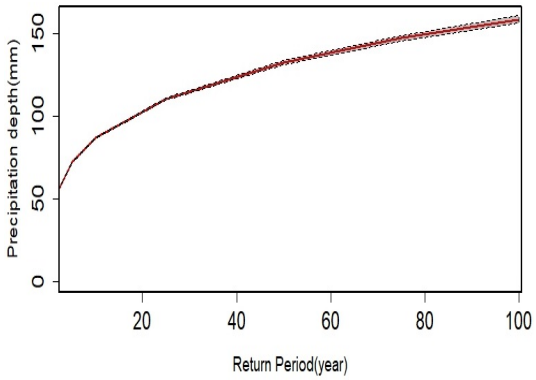

(d) Location No. 3

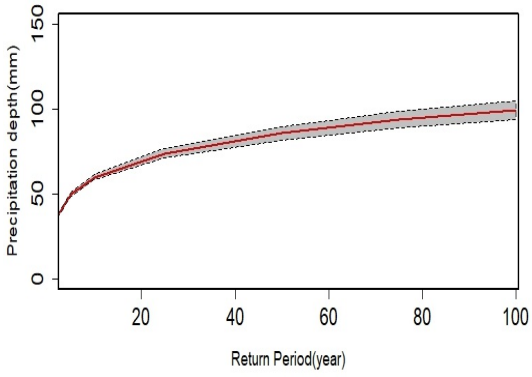

(e) Location No. 4

Figure 3.10: Sample IDF curves for some randomly chosen locations over Washington state

of the mean value from the Markov chain of return level estimates at each individual pixel. Therefore, the confidence intervals might be slightly different at various locations based on the model fit and the magnitude of return level.

3.4.6 Model Verification

Goodness of Fit

To assess the goodness of fit for the applied hierarchical model, return level plots showing the modeled return levels versus the empirical return level from the bias-corrected PERSIANN-CDR data are generated for some randomly selected locations over the study area (Figure 3.11). Geographic locations of the selected random points are also shown in this figure. The random points are selected in a way that the model's performance is assessed at locations with various climatic and elevation conditions.

As seen in Figure 3.11, the return level estimates from the constructed LVM model match well with the empirical estimates from the bias-corrected PERSIANN-CDR data. It is observed that the LVM model provides a good fit to the bias-corrected PERSIANN-CDR data. Therefore, the constructed model performs well in capturing and simulating the marginal behavior of the extreme rainfall data at various parts of the study region.

Comparison with Gauge-based Estimates

In order to verify the performance of the fitted model in extrapolating the extreme events, the satellite-based DDF curves at two random locations are compared with the gauge-based DDF curves at the corresponding locations. At each gauge location, the annual maximum data are extracted from the gauge records and the GEV distribution is fitted to the maxima data using the maximum likelihood method. Various point-wise return levels are then extrapolated from

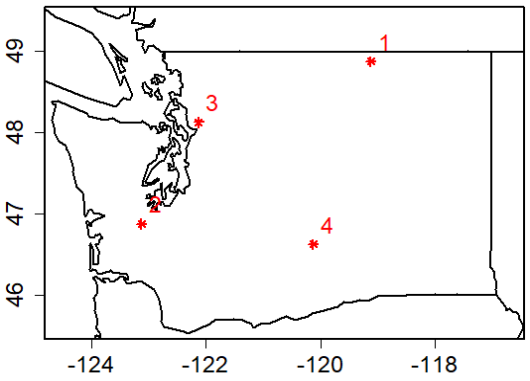

(a) Spatial distribution of the selected locations

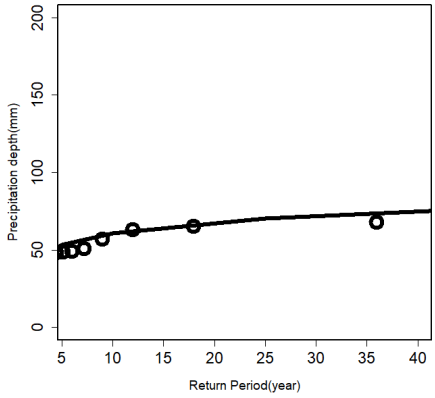

(b) Location No. 1

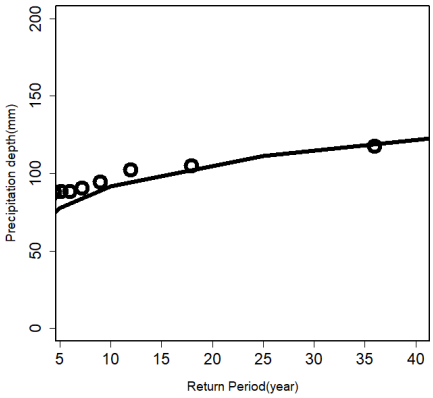

(c) Location No. 2

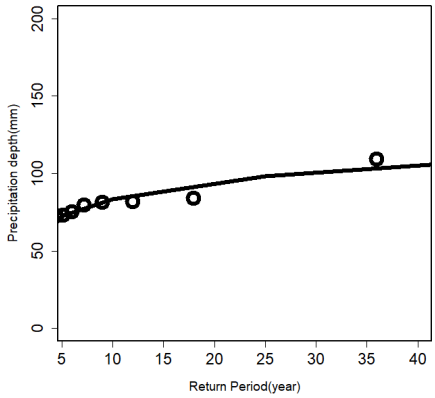

(d) Location No. 3

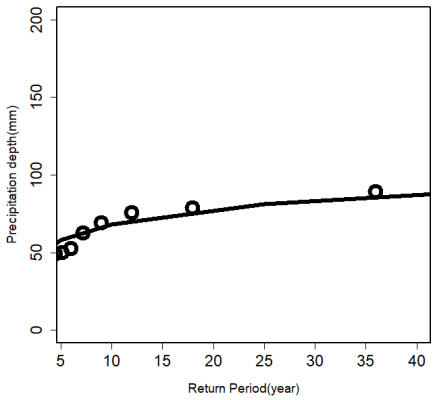

(e) Location No. 4

Figure 3.11: Return level plots from the LVM model versus the empirical return level estimates from the bias-corrected PERSIANN-CDR data

the fitted distributions to generate the gauge-based DDF curves. It is worth mentioning that for the sake of temporal consistency with the satellite data, gauge data for the similar period (i.e. 1983-2018) was used. The satellite-based DDF curves are also extracted for the corresponding locations from the fitted LVM model.

According to Figure 3.12, the satellite-based DDF estimates correspond well the gauge-based estimates at the selected locations. Also, the extracted DDF curves at the eight gauge locations suggest that there are slight underestimations and overestimations in the satellite-based DDF curves and the fitted model does not demonstrate a systematic error behaviour.

To further verify the performance of the satellite-based LVM model, we compared the generated return level maps with two available references over the study domain. The first one is the NOAA Atlas 2 volume 9 published in 1973, which is the latest frequency atlas prepared and published by NOAA for the state of Washington (Miller et al., 1973). Miller et al. (1973) used simplified relations between the precipitation durations and return periods to generate various combinations of these variables from multiple key maps. Associations between the precipitation frequencies and meteorological and topographic factor at the gauge stations were developed to assist interpolation between the rain gauges. The other reference that we used to validate the performance of the satellite-based LVM model was the paper by Wallis et al. (2007) in which the authors focused on regional precipitation frequency analysis over the state of Washington. Wallis et al. (2007) used the regional frequency analysis method together with L-moment technique (Hosking and Wallis, 2005), which is commonly used in the frequency Atlas of the United States (Bonnin et al., 2006).

Comparison of the return level maps generated from the satellite data with the gauge-based estimates given in Miller et al. (1973) and Wallis et al. (2007) showed that for 24-hr extreme events associated with various return periods, our estimates are consistent with the gauge-based estimates in terms of spatial pattern and magnitude.

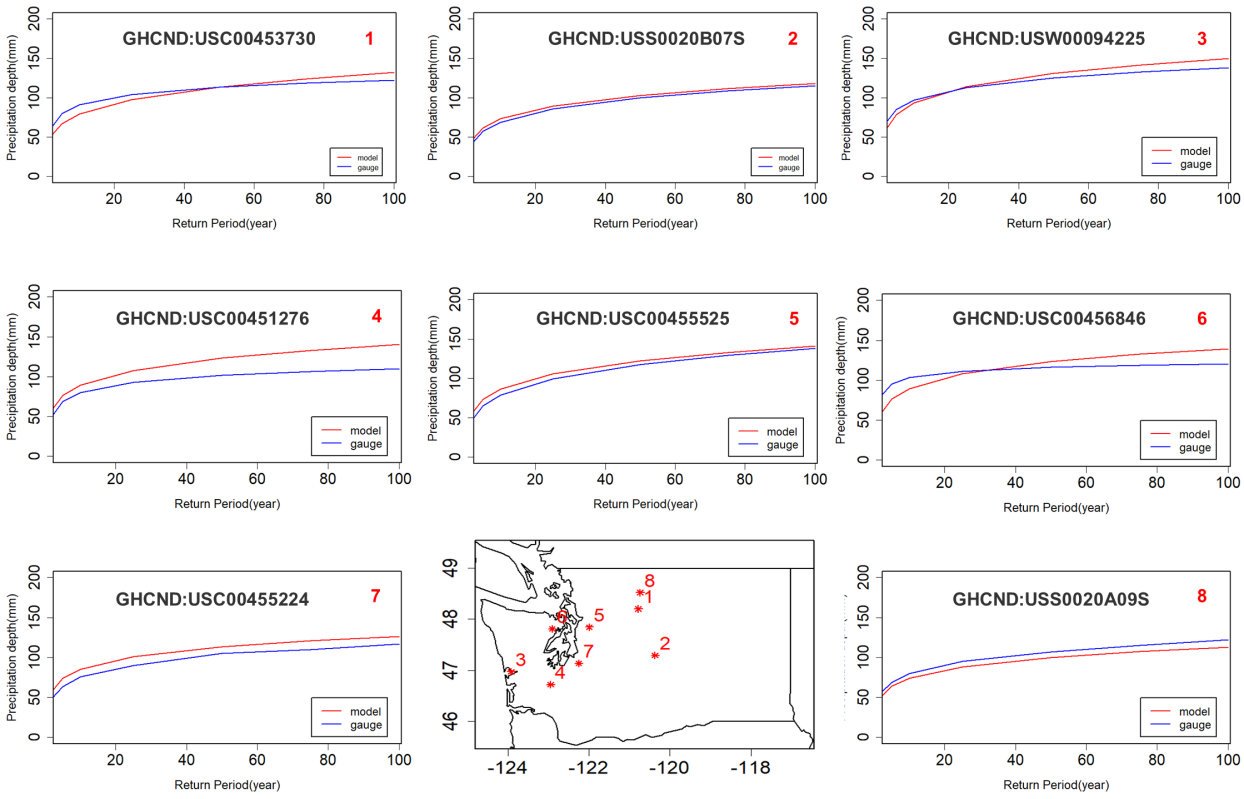

Figure 3.12: Satellite-based and gauge-based DDF curves for eight gauge locations within Washington state

3.5 Summary and Conclusions

Extreme precipitations are associated with increased flood hazards, and therefore, require a diligent modeling effort. The conventional approach for modeling extreme precipitations is based on using the ground-based observations, which in many parts of the world are limited or even non-existent. In recent years, information from weather radars and earth observing satellites have been used for modeling intense precipitations. However, such information often suffers from the shortness of data length and estimation uncertainties for frequency analysis. The PERSIANN-CDR, a satellite-based precipitation dataset with 35+ years of high resolution(daily, 0.25$\circ$) precipitation information provides a unique opportunity to analyze the historical extreme rainfalls, especially in poorly instrumented regions.

In this study, the PERSIANN-CDR dataset has been employed to spatially model the extreme precipitations over the state of Washington. This state is among the few states that its rainfall frequency information has not been updated in the recent versions of the frequency Atlas of the United States. A hierarchical Bayesian model namely the latent variable model (LVM) was used to spatially model the satellite-based extreme precipitation estimates over the study domain. A Markov chain Monte Carlo algorithm was further applied to make inference on the posterior probabilities of the model parameters. An exploratory analysis was also performed to investigate the extent of spatial dependence in the data.

Results of the exploratory analysis demonstrated the existence of a spatial dependence structure in the extreme precipitation data in the state of Washington. The spatial pattern for the location and the scale parameters of the spatial GEV model were almost similar, with generally larger values over the Western areas of the study domain. However, the spatial pattern was not clear for the shape parameter, which is the parameter that characterizes the tail behavior of the GEV distribution. This observation also corresponded with the previous knowledge regarding the difficulty of estimating the shape parameter, especially when the

data length is short.

After constructing and fitting the LVM model, it has to be assessed in terms of convergence, prior to making any marginal extrapolation. For this purpose, traceplots and autocorrelation plots were generated. The estimated convergence diagnostics demonstrated that the simulated chains have converged to the stationary distributions. In fact, the traceplots showed that the chain values are almost steady and there are no long-term trends in the chain values. Also, the autocorrelation plots revealed that the chain values at successive iterations are independent from each other.

Spatial maps for the GEV parameters and various extreme rainfall quantiles were also generated. Our results show that for the location and the scale parameters of the GEV distribution, there is a west-east gradient with larger values over the west and smaller values over the east. For the shape parameter, the spatial pattern seemed to be largely influenced by the precipitation pattern and the topography over the study region. The observed spatial pattern for the extreme quantiles was comparable to that of the annual precipitation over the study region with the most extreme events taking place near the windward slopes of the Coastal range and the Cascade mountain range. This pattern corresponds with the moisture regime over this region, where the two major releases of the moisture take place near the mountain ranges parallel to the coastal line where intense orographic precipitations always happen.

Model testing procedures suggested that the LVM model fits well to the empirical quantiles from the bias-corrected PERSIANN-CDR data at the randomly selected locations. Furthermore, it was shown that the depth-duration-frequency(DDF) curves generated by the proposed model mimic the gauge-based DDF curves at the tested gauge stations. Comparison of the satellite-based return level maps with the gauge-based maps also revealed that the extreme quantiles from the proposed model are consistent with the gauge-based estimates in terms of spatial pattern and magnitude.

Results of this study demonstrate that by employing proper statistical methods, satellite-based precipitation information could be used for real world engineering designs and hydrological risk assessment studies, especially where the observational networks are poor.

Chapter 4

Extreme Precipitation Modeling for the Pacific Northwest United States Using Satellite Information and Max-Stable Processes

4.1 Introduction

Extreme rainfall information is crucial for a wide range of engineering applications such as planning and designing hydraulic and hydrologic structures. This information is given to the extreme precipitation models for estimating the magnitude of extreme events for a given return period at the location of interest. Given the sparsity of gauge observations, especially in remote and high elevation regions, different methods have been proposed to augment the parameter estimation at ungauged locations. Typically, the regional frequency analysis (RFA) approach is used to characterize the frequency of extreme events. The RFA

approach is based on the regionalization concept, which trades space for time to acquire more information from the gauge networks to enhance the efficiency of parameter inference. RFA methods also improve the at-site frequency estimates by reducing the uncertainties of the point-wise estimation.

The RFA approach utilizes the observations from a group of rain gauges recognized to be in a "homogeneous" region to estimate the characteristics of extreme rainfalls at each location in the region. It pools the short records from a sparse gauge network in a homogeneous region to estimate the parameters of the extreme precipitation model. One of the most commonly applied RFA approaches is the index flood (IF) method (Dalrymple, 1960), which assumes the marginal parameter distributions are identical apart from a site-specific scaling factor. Though the RFA approach has been widely used for the hydrologic frequency analysis, there are a few restrictive assumptions. The defined conditions for the so-called "homogeneous" regions in many cases cannot be met unless the size of the region shrinks considerably. The regionalization introduces discontinuities at the regions' boundaries, and further results in contrasting quantile estimates at two sites that are separated by a virtual region boundary. Furthermore, the L-moment technique (Hosking and Wallis, 1997), which is often used for parameter estimation in RFA approach is not able to accommodate additional geographical and meteorological information in the model. The inclusion of additional information (i.e. covariates) contributes to the model's abilities in assessing the model parameters (Renard, 2011).

Given the recent advances in the in the area of extreme value modeling in statistics literature, alternative methods with more solid mathematical foundations have been proposed to model extreme events; see Davison et al. (2012) for a review of recent methods. Max-stable processes, as the extension of multivariate extreme value theory to the infinite dimensional scale (De Haan et al., 1984), can model the marginal distributions and the dependence structure of the model parameters simultaneously. These features suggest the max-stable processes

could be a suitable tool for modeling spatial extremes. De Haan et al. (1984) also proposed a spectral representation for the max-stable processes based on some previous studies using various spatial max-stable models, such as Brown and Resnick (1977), Schlather (2002), Schlather and Tawn (2003), and Opitz (2013). In more recent literature, Gaume et al. (2013) used the max-stable processes to map the extreme snowfalls over the French Alps and generated some return level maps for operational risk management. Mujumdar et al. (2018) modeled the dependence structure of the urban precipitation using the max-stable models with various geographical and meteorological covariates. Reich and Shaby (2012) modeled extreme precipitation over the Eastern United States using a spatial max-stable model.

Another limitation of conducing RFA is the availability of data. In recent years, various satellite-based precipitation products have been developed providing rainfall information in high spatial and temporal resolution over the globe. This information is extremely valuable for the parts of the world where the in-situ observational networks are sparse or not available. Yet, the satellite-based precipitation products are not free from errors and estimations biases. Careful evaluations of these products before applying them for the practical designs are necessary. Recently, a few studies have applied and evaluated the remotely-sensed information for extreme precipitation modeling and rainfall frequency analysis (Overeem et al., 2009; Wright et al., 2013; Eldardiry et al., 2015; Marra and Morin, 2015; Gado et al., 2017; Faridzad et al., 2018; Ombadi et al., 2018). Given the need to the long-term precipitation records with high spatial and temporal resolutions to, In order to construct reliable extreme precipitation frequency models, long-term data records with high spatial and temporal resolutions are always needed. Among a few of the available satellite rainfall products providing long-term precipitation data, , the Precipitation Estimation from Remotely Sensed Information and Artificial Neural Networks-Climate Data Record (PERSIANN-CDR) has the longest data records (from 1983 to present), and the rainfall records are with high temporal and spatial resolutions (daily and 0.25-degree). Gado et al. (2017) applied the PERSIANN-CDR product for rainfall frequency analysis in Colorado and California, and verified the

suitability of PERSIANN-CDR for rainfall frequency analysis. Faridzad et al. (2018) proposed a bias-correction approach to adjust the PERSIANN-CDR extreme rainfall estimates and applied the bias-corrected data for rainfall frequency analysis and obtained consistent estimates with the NOAA Atlas 14.

In this chapter, we further applied the PERSIANN-CDR product together with max-stable processes for constructing spatial extreme precipitation models for the Pacific Northwest (PNW) region in the United States. The PNW region consists of the 5 states located in the Northwest United States, including the states of Washington, Oregon, Idaho, Montana, and Wyoming. This region has been selected since the rainfall frequency Atlas of the United States, known as Atlas 14, has not been updated for this region since 1973. This designed study was conducted in three steps: (1) bias-correction of the PERSIANN-CDR extreme rainfall estimates using gauge information, (2) applying spatial max-stable models with various dependence structures to the bias-corrected precipitation data, and (3) assessment of the models' performances based on various evaluation metrics.

The remainder of this chapter is organized as follows: the utilized data are explained in Section 2. A review of the univariate extreme value theory and the explanation of the various parametric max-stable processes are presented in Section 3. Results and discussions are presented and discussed in Section 4. The main conclusions of the study are summarized in Section 5.

4.2 Study Area and Data

4.2.1 Study Area

The study area of this research is a rectangular region over the PNW, and includes the states of Washington (WA), Oregon (OR), Idaho (ID), Montana (MT), and Wyoming (WY). The corresponding coordinates of this rectangular region are $125°30'W$ to $102°30'W$, and $40°00'N$ to $50°00'N$ (Figure 4.1).

To model spatial extreme precipitation, PERSIANN-CDR pixels within the study area are treated as individual rain gauges located at the centroids of the corresponding pixels. Figure 4.1b demonstrates the PERSIANN-CDR grid boxes and the locations of the virtual rain gauges.

4.2.2 Satellite-based Data

Bias-adjusted PERSIANN-CDR Data

Extreme precipitation models in this study are fitted to the annual maximum time series (AMS) from the bias-adjusted PERSIANN-CDR data (rather than the original PERSIANN-CDR data). The methods of removing the biases are reported in in some recent studies of applying the PERSIANN-CDR data for extreme precipitation analysis (Faridzad et al., 2018; Miao et al., 2015). Furthermore, in order to achieve satellite-based return level estimates comparable to that of the NOAA Atlas 14, the gridded data must be downscaled to the point resolution (Faridzad et al., 2018).

In details, the approach proposed by Faridzad et al. (2018) was used to in removing some biases of the PERSIANN-CDR extreme rainfall estimates over the United States. This

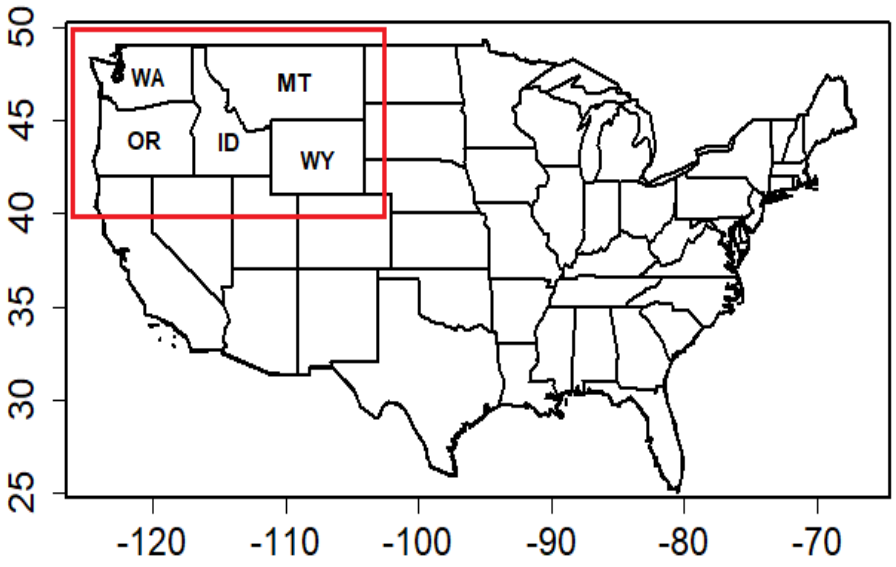

(a)

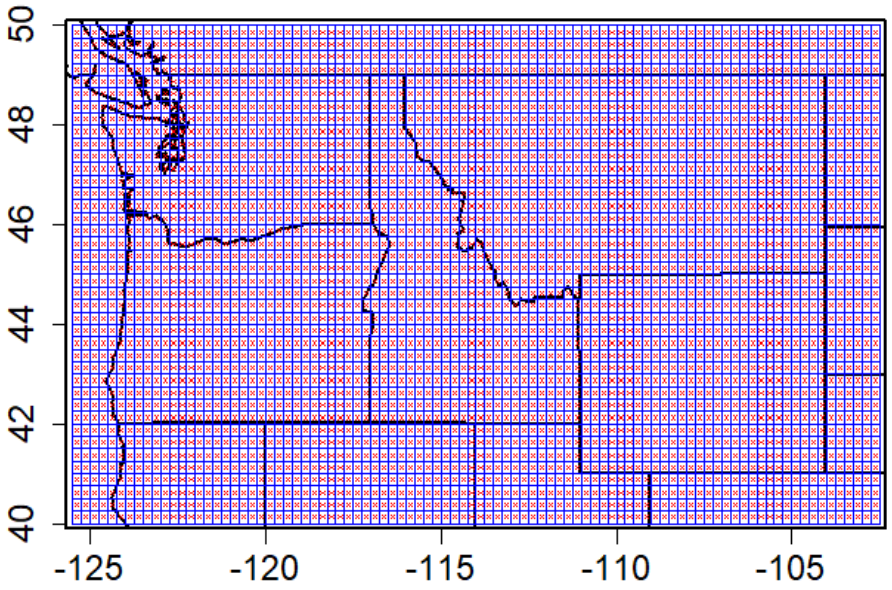

(b)

Figure 4.1: (a) Map of the Contiguous United States and the location of the study area; and (b) map of the Pacific Northwest region along with the location of PERSIANN-CDR pixels. The blue grid lines show the boundaries of PERSIANN-CDR and DEM pixels and the red asterisks denote the centroid of each grid box

approach is based on an elevation-based regression function that adjusts the AMS at each pixel of PERSIANN-CDR based on its altitude. In practice, the following steps were taken to achieve the bias-adjusted precipitation data for spatial extreme precipitation modeling: the annual maximum time series (AMS) of precipitation is extracted at each pixel of PERSIANN-CDR over the study region. Then, the extracted AMS at each pixel is bias-corrected using a correction function that generates correction factors (C.F.) for each location based on the elevation of that location. The applied correction function proposed by Faridzad et al. (2018) for PERSIANN-CDR data over the United States is $C.F. = 2.4855 \times elevation^{-0.215}$;where, $C.F$ is the correction factor for the AMS at each pixel. The elevation information for each gauge location(i.e. PERSIANN-CDR pixel) is extracted from the digital elevation model (DEM) for the PNW region.

4.2.3 Elevation Data

The elevation information for each gauge location(i.e. PERSIANN-CDR pixel) is extracted from the digital elevation model (DEM) for the PNW region. In this study, elevation information was used for two purposes: 1) for bias-adjusting the AMS at each PERSIANN-CDR pixel; 2) as an additional spatial covariate for the spatial extreme value models. For the sake of consistency with the precipitation dataset,a digital elevation model(DEM) with the spatial resolution of 0.25-degree($\sim$ 25 km) developed by NOAA was obtained and used. This dataset can be downloaded from the following url: http://research.jisao.washington.edu/data_sets/elevation/

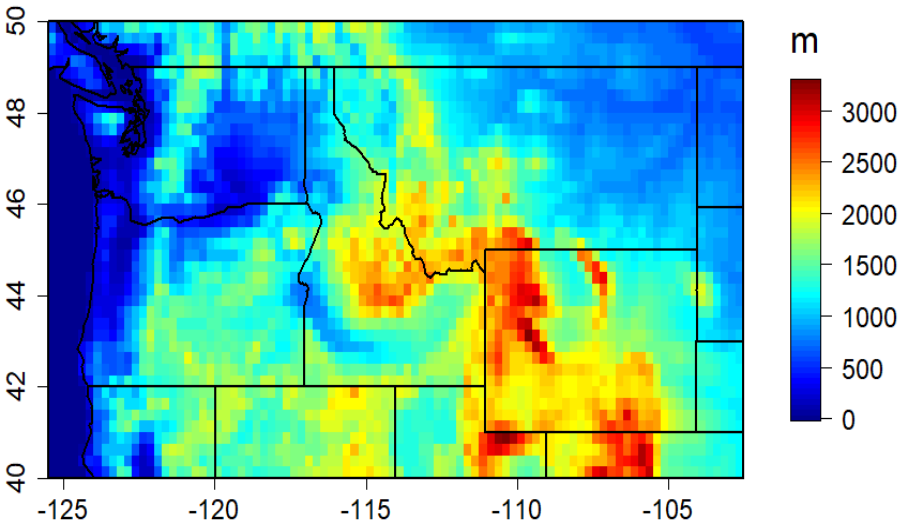

(a)

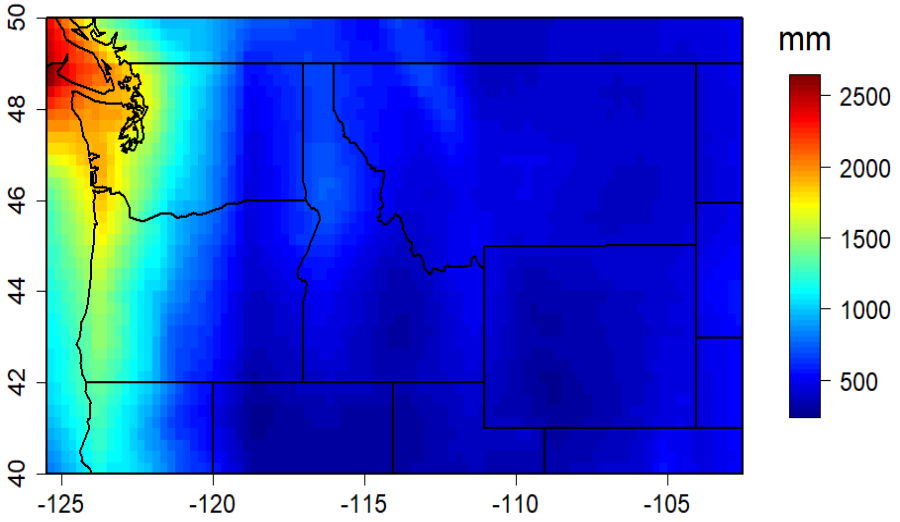

(b)

Figure 4.2: (a) Elevation map of Washington state; and (b) Map of the mean annual precipitation over Washington state from PERSIANN-CDR data

4.3 Methodology

4.3.1 Univariate Extreme Value Analysis

Let $X_1, ..., X_n$ be a set of independent and identically distributed random variables. The univariate extreme value theory defines the statistical behavior of the random variable $Y_n = \text{Max}\{X_1, ..., X_n\}$. If F is the non-degenerate limiting distribution to the linearly rescaled process Y_n, then for all $n > 1$, F must be a max-stable process with the following formulation:

$$F^n\left(\alpha_n y + \beta_n\right) = F(y) \tag{4.1}$$

where $\alpha_n > 0$ and $\beta_n \in \mathbb{R}$ are normalizing constants. The only distribution function that satisfies equation (4.1) is the generalized extreme value distribution or GEV(μ, σ, ξ), where $\mu \in \mathbb{R}$ is the location parameter, $\sigma > 0$ is the scale parameter, and $\xi \in \mathbb{R}$ is the shape parameter. The shape parameter specifies the characteristics of the tail of the GEV distribution, with $\xi < 0$ corresponding to the Weibull case with a finite upper bound, $\xi = 0$ corresponding to the light-tailed Gumbel distribution, and $\xi > 0$ corresponding to the heavy-tailed Fréchet distribution. The cumulative distribution function (CDF) of the GEV distribution is given by equation (4.2):

$$F(y) = \begin{cases} \exp\left(-\left[1 + \xi\dfrac{y-\mu}{\sigma}\right]^{-\dfrac{1}{\xi}}\right) & \text{if} \quad \xi \neq 0 \\ \exp\left(-\exp\left[\dfrac{y-\mu}{\sigma}\right]\right) & \text{if} \quad \xi = 0 \end{cases} \tag{4.2}$$

4.3.2 Max-stable Processes

Max-stable processes generalize the univariate extreme value theory to the infinite dimensional scale. The max-stable process $Z(\cdot)$ is the limiting distribution to the independent and identically distributed maxima random fields $Y_i(\cdot) \in \mathbb{R}$ if there exist continuous normalizing functions $a_n(\cdot) > 0$ and $b_n(\cdot) \in \mathbb{R}$ such that :

$$Z(\cdot) = \lim_{n \to +\infty} \frac{\max_{i=1}^{n} Y_i(\cdot) - b_n(\cdot)}{a_n(\cdot)} \tag{4.3}$$

Through this representation, the marginal distribution at each point $s \in S$ follows a univariate GEV distribution while the marginal distribution for multiple points is modeled through the continuous spatial functions of the GEV parameters $\mu(s), \sigma(s)$, and $\xi(s)$. In practice, it is often more convenient to construct a simple max-stable model by transforming the margins into a standard Fréchet distribution. The margins can subsequently be transformed back to the GEV form.

Extremal Coefficient

Modeling max-stable processes consists of two parts. The first part is modeling the marginal behavior of the data which is implemented using the processes that involve the GEV parameters. This part is often carried out using a linear modeling approach and by taking advantage from some additional covariates. The second part is modeling the spatial dependence of the extremes using some measures of spatial dependence. A common method to summarize the spatial dependence structure of data is through the extremal coefficient

function $\theta(\cdot)$ (Schlather and Tawn, 2003).

$$Pr\left\{Y(s_1) \leq y, Y(s_2) \leq y\right\} = \exp\left\{\frac{-\theta}{y}\right\} = Pr\left\{Y(s_1) \leq y\right\}^{\theta}, \qquad y \geq 0 \tag{4.4}$$

The value of θ_d can be considered as the effective number of the independent random variables in the d-dimensional variable space. The extremal coefficient takes value in $[1, 2]$ where 1 indicates complete independence, and 2 shows dependence.

F-madogram

From the field of statistics, variogram is a mathematical function that describes the degree of spatial dependence of a spatial random field, or a stochastic process that occur with spatial connectivity. Variogram is commonly used for assessing the dependence structure in the data (Cressie, 1993). However, when dealing with the extreme data, variogram could not be useful since it may not exist. A comparable tool to variogram in geostatistics is called madogram (Matheron, 1987). The madogram is defined by equation (4.5):

$$\nu(x_1 - x_2) = \frac{1}{2}\mathbb{E}\left[|Z(x_1) - Z(x_2)|\right] \tag{4.5}$$

where $Z(\cdot)$ is a stationary random field with a finite mean. However, since the choice of the GEV parameters to compute the madogram is arbitrary, Cooley et al. (2006) proposed a modified version of madogram, called F-madogram, given in equation (4.6):

$$\nu_F(x_1 - x_2) = \frac{1}{2}\mathbb{E}\left[|F(Z(x_1)) - F(Z(x_2))|\right] \tag{4.6}$$

where $Z(\cdot)$ is a stationary max-stable random field with marginal distribution F. Since $F(Z(x_1))$ is being used instead of $Z(x_1)$, the F-madogram is well defined. Equation (4.6) can be estimated using the following simplified equation:

$$\hat{\nu}_F(x_1 - x_2) = \frac{1}{2n} \sum_{i=1}^{n} [|F(Z(x_1)) - F(Z(x_2))|] \tag{4.7}$$

where $z_i(x_1)$ and $z_i(x_2)$ are the i-th observations of the random field at locations x_1 and x_2 and n is the number of observations. The F-madogram values range from 0 to 1/6 which correspond to complete dependence and complete independence, respectively.

The F-madogram is closely related to the extremal coefficient using equation (4.8):

$$\theta(x_1 - x_2) = \frac{1 + 2\nu_F(x_1 - x_2)}{1 - 2\nu_F(x_1 - x_2)} \tag{4.8}$$

4.3.3 Spectral Representation and Parametric Models

Max-stable processes can be explained by the spectral representation of De Haan et al. (1984). Let $\{\zeta_j\}_{j\in\mathbb{N}}$ be a Poisson point process and $W(s)$ be a stationary process, then the process $Z(s)$ in (4.9) for each $s \in S$ is a max-stable process with unit Fréchet margins.

$$Z(s) = \max_{i\geq 1} \zeta_i W_i(s) \tag{4.9}$$

Based on the various choices for the spectral processes $W_j(\cdot)$, different max-stable process models are introduced. Three types of such max-stable models are applied in this study which are described in the next sections.

The Extremal Gaussian Process(Schlather Model)

A first possible option, which is known as Schlather model (Schlather, 2002), is to take $W_i(s) = \sqrt{2\pi} max\{0, \varepsilon(s)\}$ where $\varepsilon(\cdot)$ is a standard stationary Gaussian process with correlation function $\rho(\cdot)$. The bivariate cumulative distribution function by the Schlather model for two given sites s_1 and s_2 is given in equation (4.9).

$$Pr\{Y(s_1) \leq y_1, Y(s_2) \leq y_2\} = \exp\left[-\frac{1}{2}\left(\frac{1}{y_1} + \frac{1}{y_2}\right)\left(1 + \sqrt{1 - \frac{2\{1 + \rho(s_1 - s_2)\} s_1 s_2}{(s_1 + s_2)^2}}\right)\right] \tag{4.10}$$

One of the limitations of the Schlather model is that it is unable to describe the asymptotic independence. Because of a positive definite $\rho(\cdot)$, the extremal coefficient does not span over the $[1, 2]$ interval and instead, takes values in $[0, 1.838]$. Subsequently, even if the distance between the two sites converge to infinity, the Schlather model does not show a complete independence of these two sites.

The powered exponential correlation function was used throughout this study which has the form $\rho(h) = \exp[-(h/\lambda)^\nu]$, where $\lambda \geq 0$ is the range parameter and $\nu \in (0, 2]$ is the smoothness parameter. These parameters are estimated when fitting the Schlather model to the data.

The Brown-Resnick process

A second possible choice, known as Brown-Resnick model (Brown and Resnick, 1977), is to take $W_i(s) = \exp\{\varepsilon_i(s) - \sigma^2(s)/2\}$ where $\varepsilon(\cdot)$ is a centered Gaussian process with stationary increments and $\sigma^2(s) = Var\{W(s)\}$. The bivariate cumulative distribution function of the

Brown-Resnick process is given by equation (4.10).

$$Pr\left\{Y(s_1) \leq y_1, Y(s_2) \leq y_2\right\} = \exp\left[-\frac{1}{y_1}\Phi\left(\frac{a}{2} + \frac{1}{a}log\frac{y_2}{y_1}\right) - \frac{1}{y_2}\Phi\left(\frac{a}{2} + \frac{1}{a}log\frac{y_1}{y_2}\right)\right] \quad (4.11)$$

where $a^2 = Var(W(s_1 - s_2))$ and Φ denotes the standard normal cumulative distribution function.

The Extremal-t Process

Finally, a third possible choice which is a generalization of the Schlather model, is known as the extremal-t process (Opitz, 2013) and is formulated by defining the spectral process $W_i(\cdot)$ in the following format:

$$W_i(s) = c_v \max\left\{0, \varepsilon_i(s)\right\}^v \quad (4.12)$$

where ε is a standard Gaussian process with correlation function ρ and c_v is given as follows:

$$c_v = \sqrt{\pi}2^{-(v-2)/2}\Gamma\left(\frac{v+1}{2}\right)^{-1}, v \geq 1 \quad (4.13)$$

where Γ is the Gamma function. The bivariate cumulative distribution function for the extremal-t process is given by:

$$Pr\left\{Y(s_1) \leq y_1, Y(s_2) \leq y_2\right\} = \exp\left[-\frac{1}{y_1}T_{v+1}\left\{-\frac{\rho(s_1-s_2)}{b}+\frac{1}{b}\left(\frac{y_2}{y_1}\right)^{1/v}\right\}-\right.$$
$$\left.\frac{1}{y_2}T_{v+1}\left\{-\frac{\rho(s_1-s_2)}{b}+\frac{1}{b}\left(\frac{y_1}{y_2}\right)^{1/v}\right\}\right] \tag{4.14}$$

where T_v is the cumulative distribution function of a Student random variable with v degrees of freedom and $b^2 = \left\{1-\rho(s_1-s_2)^2\right\}/(v+1)$.

4.3.4 Inference Procedure

Because of computational burden, estimating the full-likelihood of max-stable processes have been less desirable. Instead, the composite likelihood or more specifically, the pair-wise likelihood is always used as an alternative. The composite likelihood is evaluated at all pairs of locations is maximized when making inference on the parametric max-stable models(Padoan et al., 2010). The pairwise log-likelihood for a set of n independent copies of a max-stable process observed at D sites is:

$$\ell(\phi) = \sum_{k=1}^{n}\sum_{i\leq j} \log f(y_i^k, y_j^k; \phi), \quad i,j \in D \tag{4.15}$$

where $\phi = [\theta, \alpha]$, with θ as the marginal parameter, $\alpha = [\lambda, \nu]$ as the dependence parameter, and f is the probability density function of the bivariate max-stable process.

The estimation procedure for the applied max-stable models was conducted in R environment

(R Core Team, 2013) and `SpatialExtremes` package (Ribatet, 2013) was also used in some parts of the analysis.

4.3.5 Model selection

model selection is conducted by minimizing the composite likelihood information criterion (CLIC) which has similar properties to the Takeuchi's information criterion (TIC) (Takeuchi, 1976). TIC is computed as follows:

$$TIC = -2\ell\left(\hat{\phi}\right) + 2tr\left\{J^{-1}\left(\hat{\phi}\right) H\left(\hat{\phi}\right)\right\} \tag{4.16}$$

where $\hat{J}$ and $\hat{H}$ are the estimated Jacobian and Hessian information matrices, respectively. TIC value for each model is computed using the `SpatialExtremes` package (Ribatet, 2013) in R (R Core Team, 2013). The model with the lowest TIC value is considered as the best model.

4.3.6 Fitting Model to Data

The spatial max-stable models defined earlier are fitted to the precipitation data using a pre-defined structure for the trend surfaces. Consequently, the following model for the marginal

parameters of the GEV distribution is considered:

$$\begin{cases} \mu(s) = \beta_{\mu}^{T} c(s) + \varepsilon_{\mu}(s) \\ \sigma(s) = \beta_{\sigma}^{T} c(s) + \varepsilon_{\sigma}(s) \\ \xi(s) = \beta_{\xi}^{T} c(s) + \varepsilon_{\xi}(s) \end{cases} \tag{4.17}$$

where the random parts $\varepsilon_{\mu}(\cdot)$, $\varepsilon_{\sigma}(\cdot)$, and $\varepsilon_{\xi}(\cdot)$ are assumed to be independent stationary zero-mean Gaussian processes with covariance function $\alpha_n \exp(-\|h\|/\lambda)$ with unknown sill and range parameters. All of the GEV parameters including the location $\mu(\cdot)$, the scale $\sigma(\cdot)$, and the shape $\xi(\cdot)$ parameters are assumed to be linear combinations of the covariates associated with each location $s \in S$ with unknown vector of coefficients β_{μ} ,β_{σ}, and β_{ξ}.

Covariates that we used in this chapter are latitude(lat), longitude(lon), altitude(alt), and mean annual precipitation (MAP). MAP value at each pixel was estimated using the entire record of PERSIANN-CDR dataset. The values of all of the above-mentioned covariates were computed for the centroids of PERSIANN-CDR (resp. DEM and MAP layers) grid boxes. In order to minimize the effect of large covariates on the coefficient values, all of the covariates were normalized prior to fitting the max-stable models.

4.4 Results

4.4.1 Exploratory Analysis

An exploratory analysis is performed to investigate the existence of any spatial structure in the extreme rainfall data. The exploratory analysis tools applied here are extremal coeffi-

cient, f-madogram, and symbol plots.

Extremal Coefficient and F-madogram

As mentioned in section 4.3.2, extremal coefficient and f-madogram are two indices that summarize the spatial dependence structure in the extreme rainfall data. Figure 4.3 displays the empirical estimates of bivariate f-madogram(left panels) and extremal coefficient(right panels) as a function of the 2-D distance between the sites(in degrees). The top panels demonstrate the bivariate estimates for all pairs of sites within the study region and the bottom panels are their binned estimates with the bin size of 500. As shown in this figure, the empirical estimates for both of these variables are low at short distances and increase to their asymptotic values at larger distances. It is also observed that the full independence ($\theta = 2$) exist only at small number of pairs. The smaller values f-madogram and extremal coefficient at short distances suggest that there is a strong statistical association in the daily extreme rainfall at nearby locations. This spatial dependence decreases as the distance between the locations increase. This is in accordance with our general understanding that nearby locations are likely to be impacted in a similar fashion by the extreme rainfall events.

Symbol Plots

In order to visually assess the tail dependence structure in the extreme precipitation data, symbol plots of the pointwise GEV parameter estimates are presented in Figure 4.4. The three parameters of GEV distribution are estimated separately by maximizing the marginal likelihood at each pixel. In order to better visualize the spatial structure in GEV parameters, a circle with a radius proportional to the deviation of parameter value to areal mean value has been plotted at each pixel. The red circles suggest positive deviation and blue circles show negative deviation from the areal mean values. As seen in Figure 4.4, there is a clear

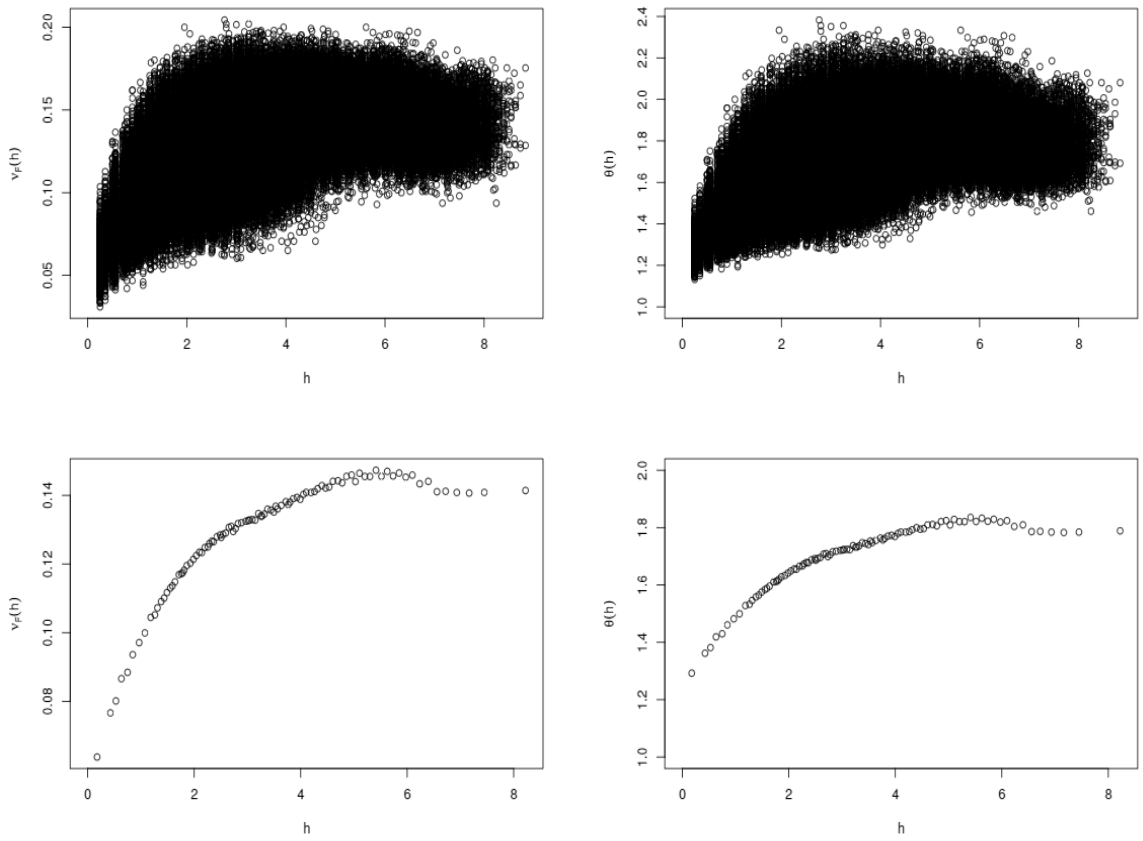

Figure 4.3: Empirical F-madogram (left panels) and the bivariate extremal coefficient (right panels) values as a function of distance(number of pixels) between locations. Lower panels are the binned representations of the top panels.

spatial pattern for location and scale parameters of the GEV distribution. Generally, larger location and scale values are observed over the western parts of the study area and they decrease gradually from west to east. This spatial pattern is similar to that of the mean annual precipitation (Figure 4.2b) over the study area. Therefore, mean annual precipitation and longitude seem to be good covariates for explaining the location and scale parameters. For the shape parameter, which characterizes the tail behavior of the GEV distribution, it is hard to find a clear spatial pattern. Lack of a clear spatial pattern is a common issue when dealing with precipitation data in large domain. Yet, there seems to be a week association between the shape parameter values and altitude(Figure 4.2a) where larger shape parameter values are observed over the Rocky Mountains in the central parts of the study area. Also, the shape parameter value are slightly larger over the northern parts of the study area. Therefore, it seems that altitude and latitude could be potential covariates for explaining the shape parameter.

Nevertheless, selecting the appropriate covariates based on the spatial variations of the GEV parameters must be implemented with care. The GEV parameter values are correlated and they can compensate each other. Yet, these preliminary results suggest that there is a strong spatial variability in extreme precipitation over the study area. Specifically, the precipitation spatial patterns over the western areas of the PNW seem to behave differently than the central and eastern areas. This is primarily due to the precipitation mechanism in this region where atmospheric rivers generate intense rainfalls over the western edges of the Washington state. The Cascade Mountain range near the western boundaries of the Washington state acts as a topographic barrier which prevents the passage of moisture to the east. As a result, while heavy orographic rainfalls are observed over the western slopes of the Cascade mountain ranges, there is desert conditions over its eastern slopes.

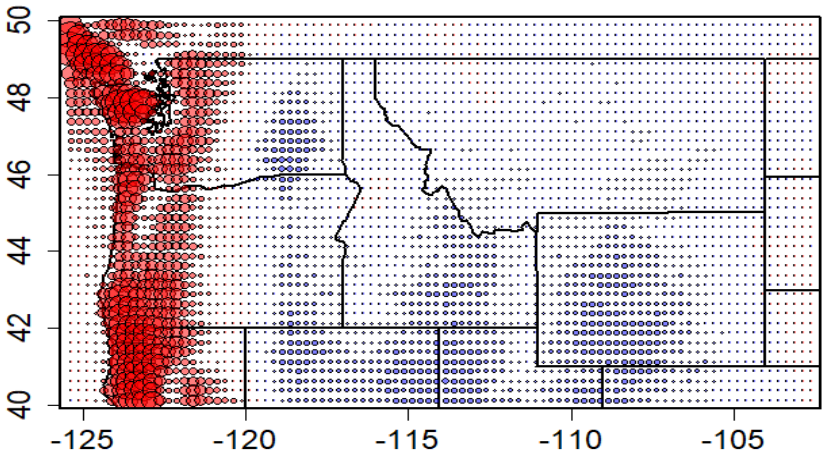

(a) location parameter (μ)

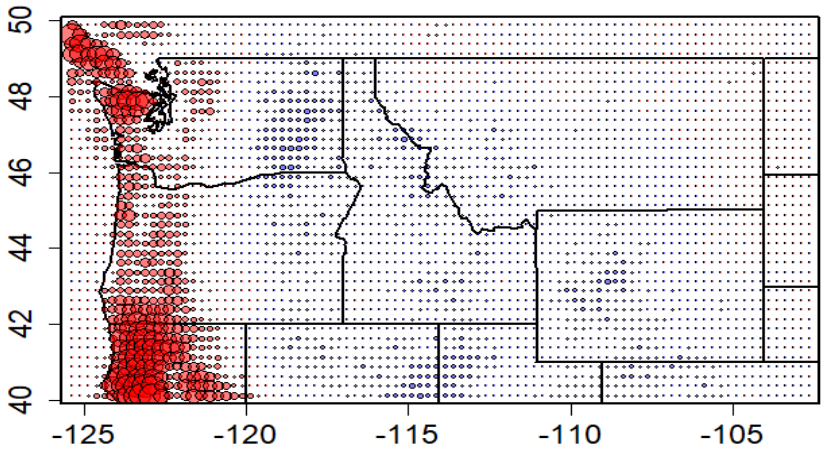

(b) scale parameter (σ)

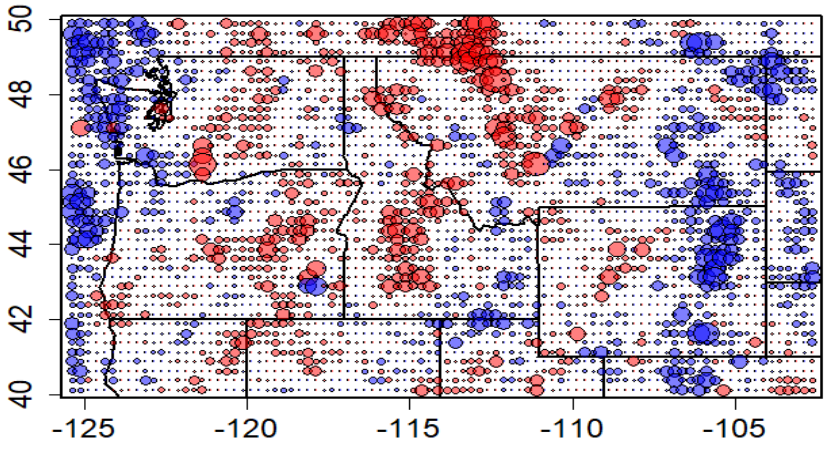

(c) shape parameter (ξ)

Figure 4.4: Symbol plot displaying the spatial pattern of point-wise estimates of GEV parameters: a) location (μ) , b) scale (σ), and c) shape (ξ) over the Washington State. The radius of the circle at each location is proportional to the departure of the parameter value at that location to the areal mean value.

4.4.2 Max-stable Models Performances

The fitted max-stable models are evaluated based on two criteria. First ,the applied models are assessed in terms of how they can model the dependence structure of the extreme rainfall data. The second criteria is TIC which is a means of evaluating the quality of the statistical models.

Modeling the Tail Dependence Structure

The fitted max-stable processes, including the Schlather, Brown-Resnick, and Extremal-t are assessed in terms of modeling the empirical bivariate extremal coefficient and f-madogram (Figure 4.5). The black shaded areas and the red lines show the empirical pairwise estimates and the models' estimates, respectively. We notice that the Schlather model provides a poor fit to the empirical estimates of both metrics. Also, according to asymptotic values of the Schlather model, this model suggests a rather strong dependence in extreme rainfall even for locations where are situated at long distances from each other. In other words, this model suggests there is still a strong association between the extreme rainfall data even at far distances and this association never disappears. This is physically not possible given that the climate and rainfall patterns could be completely different at distant locations. The Brown-Resnick and Extremal-t process models provide similar good performances in modeling the empirical bivariate extremal coefficient and f-madogram estimates. Both models capture the variability of the dependence metrics and suggest a complete dependence and an independence at short and long distances, respectively.

The poor performance of the Schlather model is due to having only one parameter (dependence range) which makes this model rather inflexible ($\theta_{Sc}(h) = 1 + \sqrt{2}/2$ for $\|h\| \to \infty$) and leads to a relatively strong dependence structure even for pairs of sites located at long distances. On the other hand, the Brown-Resnick and Extremal-t models have additional

Table 4.1: TIC values associated with each of the applied max-stable processes. Lowest TIC value indicates the best performing model

Max-stable Model	**Covariates**	**Funcation Evaluations**	**TIC**
Schlather	Lat, Lon, Alt, MAP	1705	613,249,351
Brown-Resnick	Lat, Lon, Alt, MAP	731	610,209,862
Extremal-t	Lat, Lon, Alt, MAP	903	610,203,117

* Lat: Latitude; Lon: Longitude; Alt: Altitude; MAP : Mean Annual Precipitation

smoothing parameters that increase their flexibility and lead to a superior fit to the extremal coefficient and f-madogram estimates. Therefore, they can model the entire range of tail dependence and suggest more physically possible spatial structures.

Model Selection Based on TIC

TIC is equivalent to AIC and summarizes the information that is lost by a model. The lower the information loss, the higher the quality of the model. The TIC value for each of the applied max-stable models was calculated using the `SpatialExtremes` package in R. The TIC values associated with each model is reported in Table 4.1. All the applied models had similar covariates. The presented function evaluations and TIC values were computed after the convergence was achieved. In terms of TIC, the Schlather model has the largest value among others, which implies the poorest performance. The Brown-Resnick and Extremal-t processes show superior performances compared to the Schlather model, with a slight advantage for the Extremal-t model. Yet, as shown by the number of function evaluations, this superior performance is achieved at the price of slightly longer convergence time.

Based on the applied performance metrics, the Extremal-t process is chosen as the best performing max-stable model. Therefore, this model is selected from this point forward for making inference on the GEV parameters and extreme return levels.

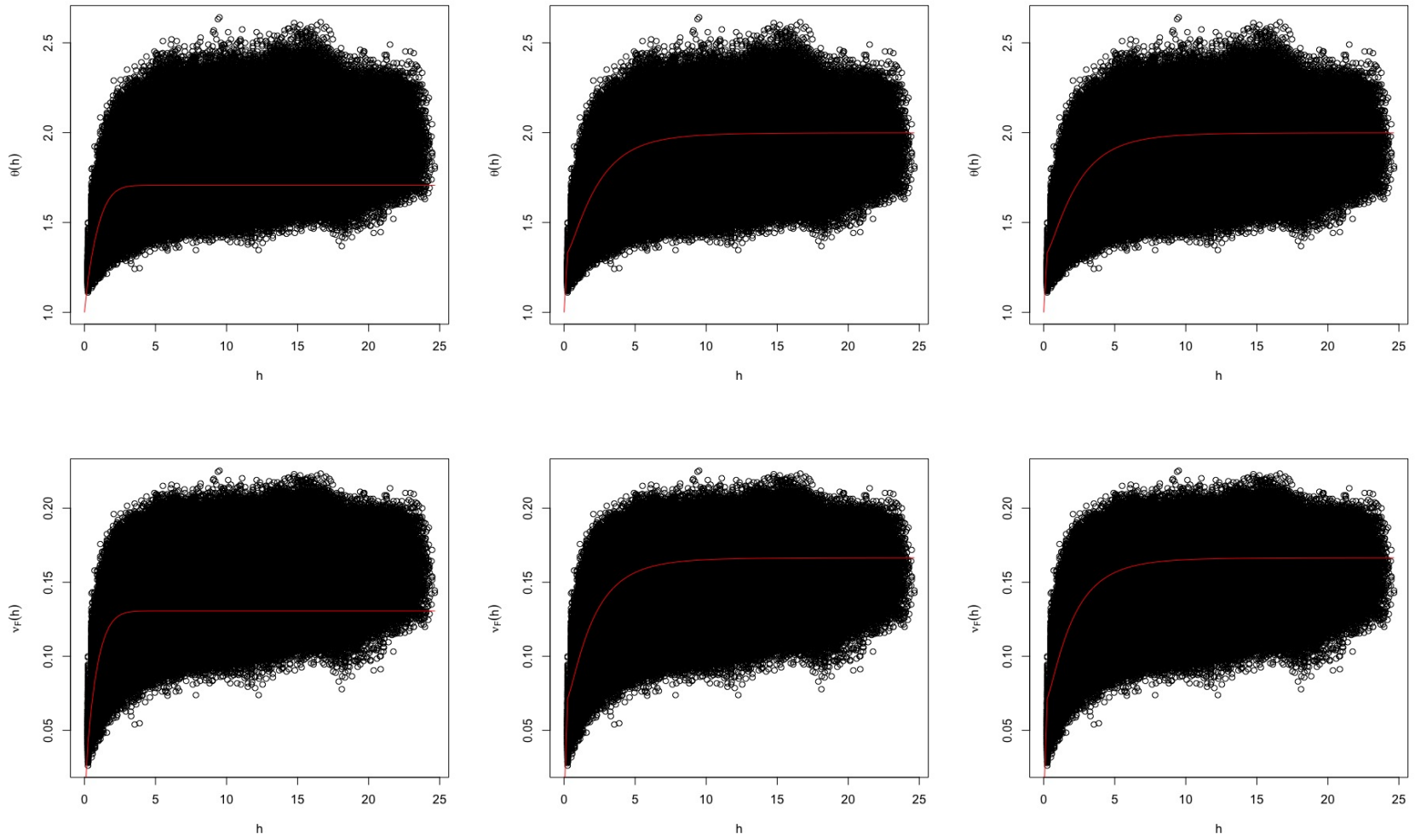

(a) Schlather (b) Brown-Resnick (c) Extremal-t

Figure 4.5: Models' fits to the empirical pairwise extremal coefficients (top row) and f-madogram estimates(bottom row) by : (a) Schlather model; (b) Brown-Resnick model; (c) Extremal-t model. The shaded areas are the empirical estimates and the red lines are the models' estimates

4.4.3 Spatial Distribution of GEV Parameters

After selecting the superior max-stable model (Extremal-t process), this model is used to calculate the GEV parameters and the extreme return levels over the study region. Figure 4.6 presents the spatial distribution of the location (μ), scale (σ), and shape (ξ) parameters of the GEV distribution. The spatial patterns of the location and scale parameters are similar, with a west-east gradient. This pattern is identical to that of the mean annual precipitation (Figure 4.2b) which indicates that these two parameters are mostly influenced by the general precipitation pattern in this region. For the shape parameter, the values are mostly positive which confirms a heavy-tailed behaviour by the data in the Fréchet domain. In terms of spatial pattern, the shape parameter values seem to be mostly influenced by the altitude covariate (Figure 4.2a) with larger parameter values over the mountainous areas such as Cascade mountain range and Rocky mountains.

4.4.4 Return Level Maps

The fitted Extremal-t model is used to generate return level maps for extreme precipitation with various return periods over the PNW region. Figure 4.7 displays the spatial patterns of extreme precipitation with 10-, 25-, 50-, and 100-years return periods over the study area. The general pattern of extreme precipitation is relatively consistent across the estimated return periods. More intense extremes are observed over the western boundaries of the study area and the magnitude of heavy rainfalls decreases as we move toward the eastern parts of the study region. This spatial pattern is similar to that of the mean annual precipitation (Figure 4.2). Extreme precipitation pattern over this region seems to be mostly influenced by the general moisture regime. The moisture traveling from the Pacific Ocean is responsible for much of the precipitation over the Washington, Oregon states, as well as the Cascade mountain range acting as a natural barrier against the movement of moisture. As a result,

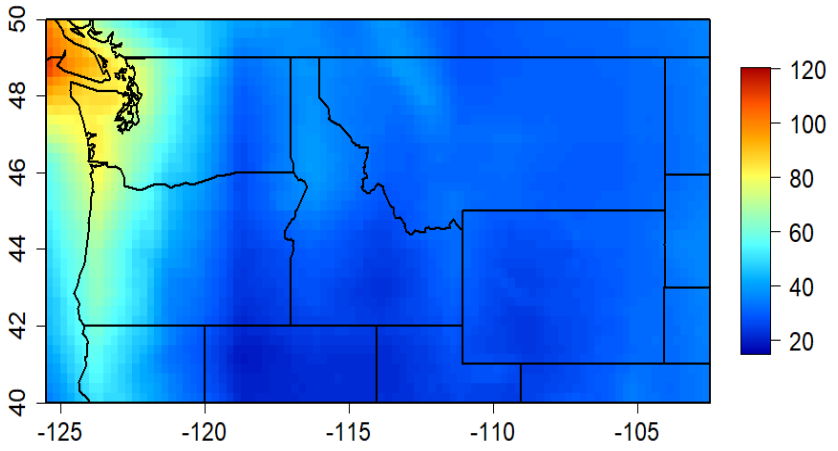

(a) location parameter (μ)

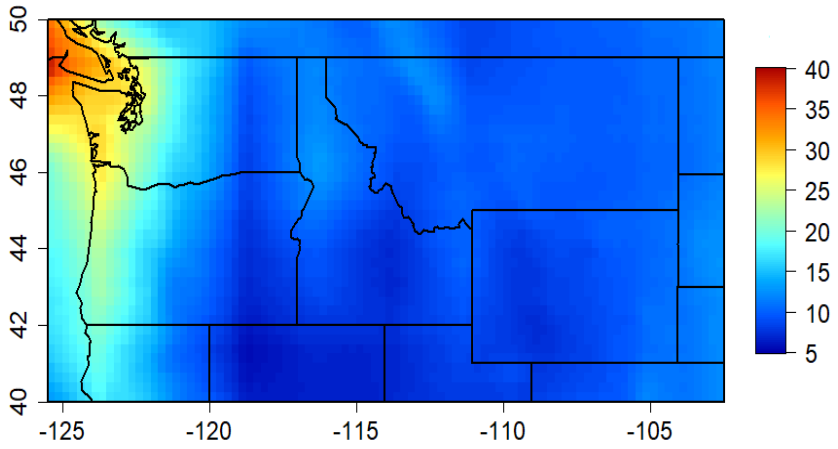

(b) scale parameter (σ)

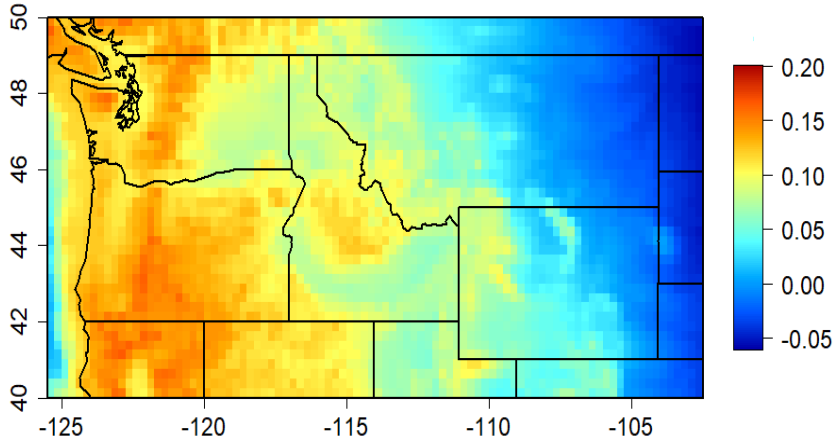

(c) shape parameter (ξ)

Figure 4.6: Spatial distribution of the GEV parameters estimated by the Extremal-t process model

heavy orographic rainfalls occur over the west-ward slopes of this mountain, while there is desert condition over the eastern slopes.

4.4.5 Model Validation

The constructed max-stable model is verified in three steps. In the first step, the ability of the Extremal-t model in capturing the spatial dependence structure of the extreme rainfall data is explored. We plot the pairwise and group-wise maxima from the fitted model and the extreme rainfall data at some randomly selected locations over the study area. In the second step, the return level estimates from the model are compared with the empirical return level estimates from the bias-corrected PERSIANN-CDR data. In this way, it ensures the quality of model fits to the observation data. Finally, the quantile estimates from the Extremal-t model are compared with the point-wise return level estimates from the ground-based gauges.

QQ plots for Groupwise Maxima

Figure 4.8 demonstrates the QQ plots of pair-wise and block-wise maxima (with a block size of 4) at some randomly selected locations separated by 65 km, 192 km, and 335 km. The values are transformed to a unit Gumble scale for a better comparison. As seen in this figure, the simulations of the annual maxima data from the Extremal-t model are in a good agreement with the observed maxima data at locations with various distances.

Comparison with Empirical Return Levels

Figure 4.9 shows the return level estimates for various return periods as suggested by the Extremal-t model versus the point-wise empirical return level estimates from the bias-adjusted PERSIANN-CDR data at some randomly selected locations. These locations are

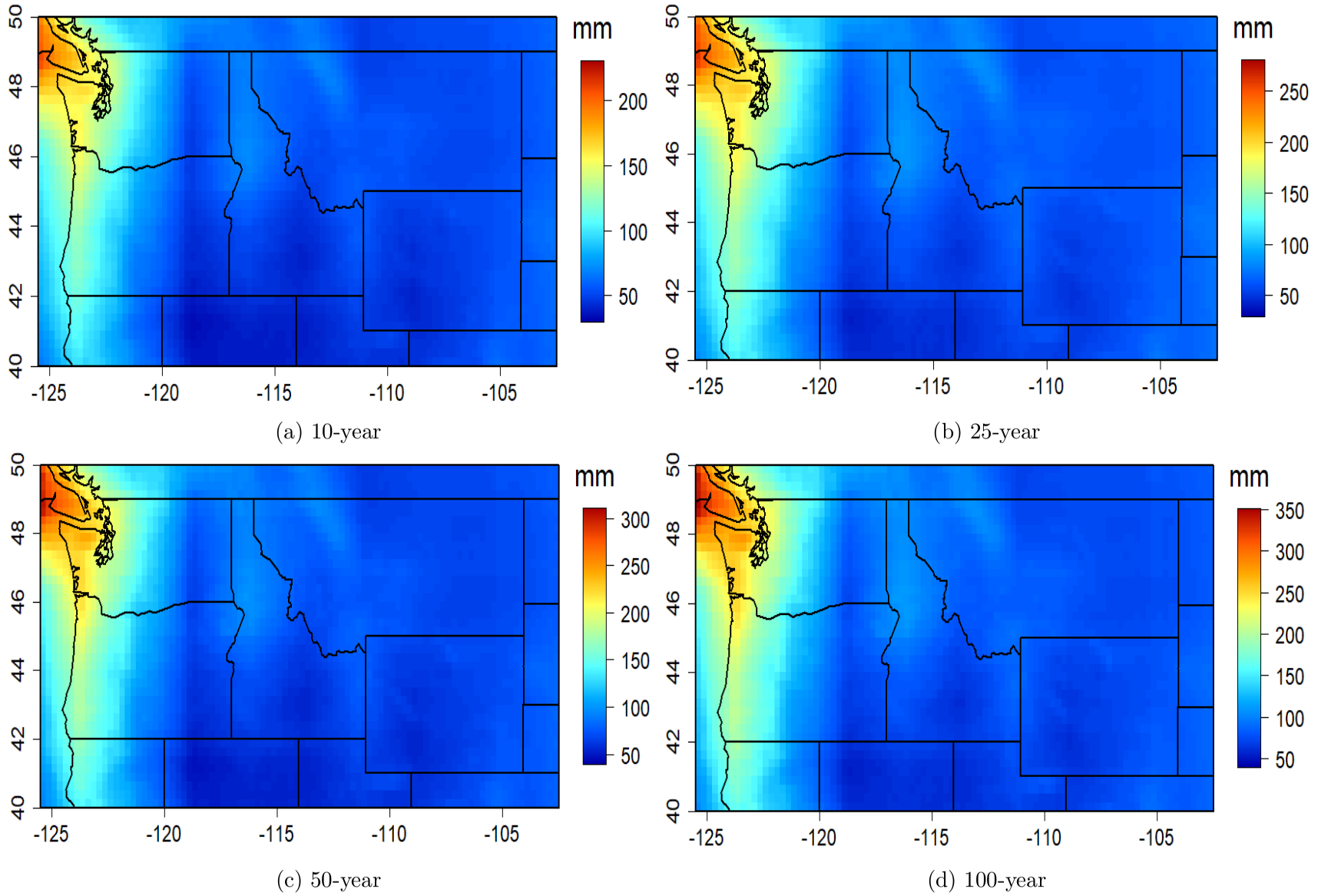

(a) 10-year

(b) 25-year

(c) 50-year

(d) 100-year

Figure 4.7: Return level maps of extreme precipitation with various return periods generated by the Extremal-t process model

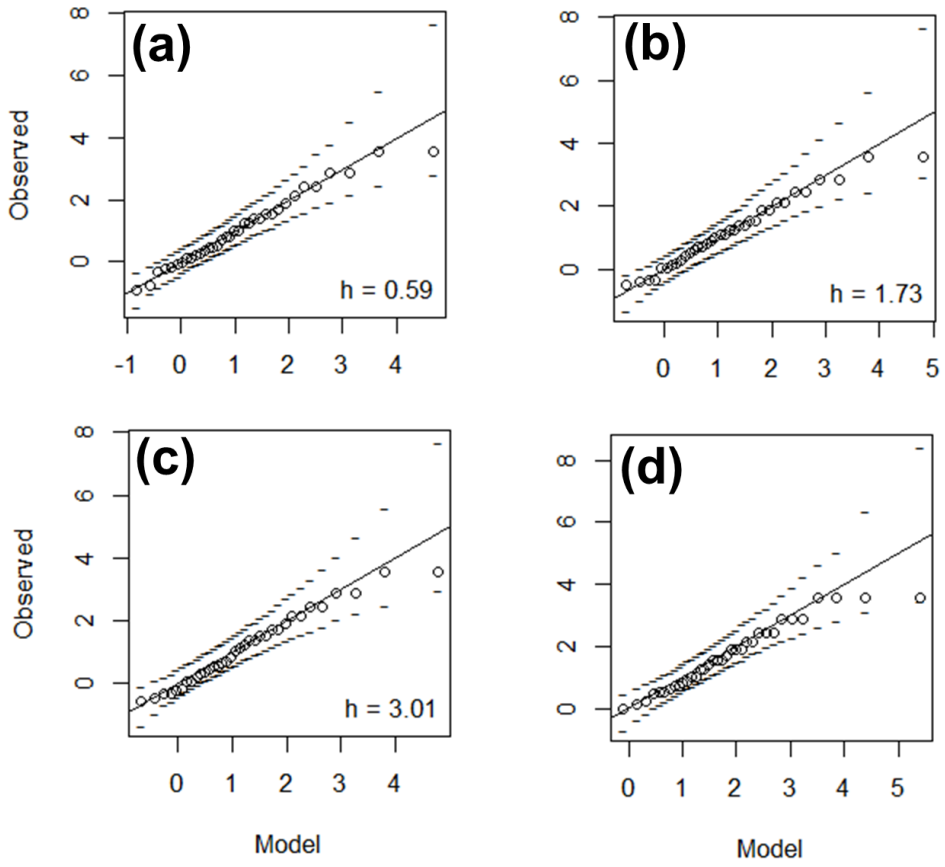

Figure 4.8: Comparison of pairwise maxima simulated from the extremal-t model and observed maxima for pairs of randomly selected stations separated by: (a) 65 km, (b) 192 km, (c) 335 km, and (d) QQ-plot for the block-wise maxima with a block size of 4. Dotted lines show the 95 % confidence intervals. For clarity, the values are transformed to unit Gumble scale

situated in various parts of the study area, which are associated with various climate and precipitation patterns. As suggested by this figure, the quantile estimates from the model agree with the empirical estimates and there is no systematic overestimation or underestimation in the model's behavior. Therefore, it can be concluded that the model has a good fit to the annual maximum data and the estimates are neither far from empirical estimates, nor over-fitted to the data. Overfitting the model to the data may result in losing the spatial dependence structure of extreme precipitation and causes the extreme estimates to develop independently at various parts of the study area. As a result, return level estimates at neighboring sites could be quite different and lacking a reasonable smooth variation in space.

Comparison with Gauge-based Return Levels

The quantile estimates from the fitted Extremal-t model are compared with the gauge-based return level estimates at 27 gauge locations distributed across the PNW region. The characteristic of the selected gauges, including their station IDs, climate classes, and geographical coordinates are presented in Table 4.2. The selected gauges represent various elevation ranges within the study area from coastal and low elevation regions to mountainous high elevations areas. Also, the various climates within the study area include dry, temperate, and Continental. The gauge-based return levels are calculated by extracting the annual maximum time series and then fitting the GEV distribution to the extreme rainfall data at each individual location. The maximum likelihood method is used at each location to estimate the three parameters of the GEV distribution. Finally, return levels associated with various return periods are computed at each location by plugging the parameter values and the return periods into the inverse GEV function. The gauge-based return level values are then compared with the model-based estimates at the collocated PERSIANN-CDR pixels.

Figure 4.10 presents the return level estimates from the Extremal-t model fitted to the bias-

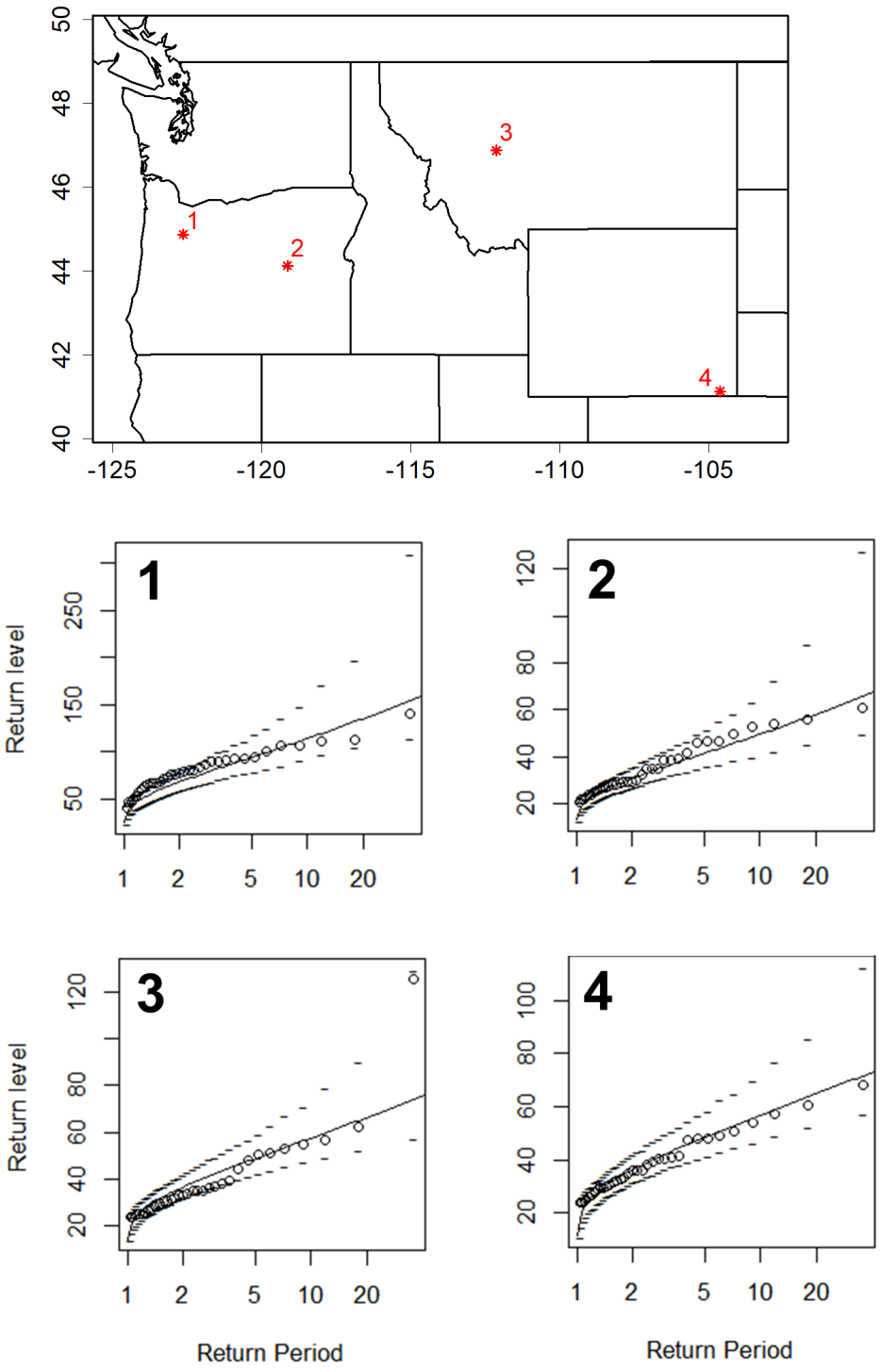

Figure 4.9: Empirical return levels from the model inputs (bias-corrected PERSIANN-CDR data) and Extremal-t model at some randomly selected locations over the study area. Each column belongs to a specific location. Map shows the spatial distribution of the selected locations

adjusted PERSIANN-CDR data and the gauge-based quantiles at 27 gauge locations over the Washington state. According to this figure, there is a good agreement between the return level estimates by the model and the estimates by rain gauges across various return periods and gauge locations. The model's performance is consistent across the various extreme event magnitudes. The proposed model is able to capture the extreme precipitation properties at regions characterized by either highly intense or low intense extremes. Also, the model-based estimates demonstrate slightly larger or smaller return level values than the gauge-based estimates at various locations. This result implies that there is no systematic overestimation or underestimation behavior by the model.

Table 4.2: Description of the selected gauges for model validation

Station No.	Station ID	Coordinates		Basin name	HUC	Köppen-Geiger	Climate description
1	GHCND:USC00244328	48.35	-114	Kootenai-Pend Oreille-Spokane	1701	Dsb, Dfb	Continental
2	GHCND:USS0013A24S	48.35	-114	Kootenai-Pend Oreille-Spokane	1701	Dsb, Dfb	Continental
3	GHCND:USS0013B22S	48.43	-113.94	Kootenai-Pend Oreille-Spokane	1701	Dsb, Dfb	Continental
4	GHCND:USS0013C31S	47.43	-113.78	Kootenai-Pend Oreille-Spokane	1701	Dsb, Dfb	Continental
5	GHCND:USS0013C43S	46.87	-113.28	Kootenai-Pend Oreille-Spokane	1701	Dsb, Dfb	Continental
6	GHCND:USS0014C13S	46.27	-113.16	Kootenai-Pend Oreille-Spokane	1701	Dsb, Dfb	Continental
7	GHCND:USS0014E01S	46.14	-114.45	Lower Snake	1706	Dfb, Dsb	Continental
8	GHCND:USC00354622	44.47	-114.49	Lower Snake	1706	Dfb, Dsb	Continental
9	GHCND:USS0017D07S	45.32	-118.08	Lower Snake	1706	Dfb, Dsb	Continental
10	GHCND:USS0013E18S	45.08	-117.55	Lower Snake	1706	Dfb, Dsb	Continental
11	GHCND:USS0013D16S	44.44	-113.32	Lower Snake	1706	Dfb, Dsb	Continental
12	GHCND:USC00451395	45.67	-113.95	Upper Columbia	1702	Dfb, Dsb, BSk	Continental, dry
13	GHCND:USC00454572	48.28	-117.71	Upper Columbia	1702	Dfb, Dsb, BSk	Continental, dry
14	GHCND:USC00456534	47.56	-120.68	Upper Columbia	1702	Dfb, Dsb, BSk	Continental, dry
15	GHCND:USC00456974	47.78	-120.65	Upper Columbia	1702	Dfb, Dsb, BSk	Continental, dry
16	GHCND:USS0020A05S	48.65	-118.73	Upper Columbia	1702	Dfb, Dsb, BSk	Continental, dry
17	GHCNDUSC00241938	48.72	-120.66	Upper Yellowstone	1007	Dfb, Dfc, BSk	Continental, dry
18	GHCND:USC00247800	45.63	-109.23	Upper Yellowstone	1007	Dfb, Dfc, BSk	Continental, dry
19	GHCND:USS0010E06S	45.73	-110.23	Upper Yellowstone	1007	Dfb, Dfc, BSk	Continental, dry
20	GHCND:USS0009E11S	44.48	-110.16	Upper Yellowstone	1007	Dfb, Dfc, BSk	Continental, dry
21	GHCND:USC00249023	44.65	-109.78	Upper Yellowstone	1007	Dfb, Dfc, BSk	Continental, dry
22	GHCND:USC00240802	46.03	-110.5	Upper Yellowstone	1007	Dfb, Dfc, BSk	Continental, dry
23	GHCND:USS0021E05S	45.76	-108.48	Willamette	1709	Csb, Dsb, Dsc	Temperate, continental
24	GHCND:USS0021D13S	44.44	-121.95	Willamette	1709	Csb, Dsb, Dsc	Temperate, continental
25	GHCND:USS0022F03S	45.1	-121.75	Willamette	1709	Csb, Dsb, Dsc	Temperate, continental
26	GHCND:USC00355221	43.59	-122.06	Willamette	1709	Csb, Dsb, Dsc	Temperate, continental
27	GHCND:USC00354606	44.62	-121.95	Willamette	1709	Csb, Dsb, Dsc	Temperate, continental

4.5 Summary and Conclusions

The main goal of this study is to model the spatial extreme precipitation over the Pacific Northwest United States using satellite-based rainfall estimates from PERSIANN-CDR product. To do so, several max-stable models were used, including the Schlather, the Brown-Resnick, and the Extremal-t models. The inputs to these model are the bias-corrected PERSIANN-CDR data. Latitude, longitude, altitude, and mean annual precipitation information were also used as covariates. In order to identify the most suitable model over the study region, we evaluated the performances in terms of capturing the spatial dependence structure of the extreme rainfall data, and models' capability in estimating the marginal distributions of the data. Extremal coefficient and f-madogram indices were used to as evaluation metrics. The quality of the applied statistical models was also assessed using the TIC metric. After identifying the superior max-stable model, we found the Extremal-t model demonstrated the highest skill, and was further applied to estimate the GEV parameters and develop the extreme return levels. The return level estimates from the Etremal-t model were verified in terms of pair-wise and group-wise maxima using Q-Q plots. The generated return level plots from this model were compared with the empirical quantile estimates from the bias-corrected PERSIANN-CDR data. Finally, the constructed DDF curves were compared with the gauge-based estimates at multiple gauge locations across the study area.

The results of our exploratory analysis demonstrated that there was an evident spatial pattern in the extreme rainfall data over the PNW region. Specifically, the extremal coefficient and f-madogram plots showed there was a strong statistical association in the extreme rainfall observations at nearby locations and this association dissipated as the distances between the locations increased. Also, the symbol plots suggested that there was an identical east-ward gradient in the location and scale parameters of the GEV distribution over the study region with higher values near the coastal areas in the west. This pattern seemed to be mostly influenced by the general precipitation patterns in this region. For the shape parameter, there

was no clear spatial pattern observed, and it became one of the challenges in estimating the corresponding parameter of the GEV distribution.

Comparison of the extremal coefficient and f-madogram estimates from each of the applied max-stable models with the empirical pairwise estimates suggested that the Brown-Resnick and Extremal-t processes provide similar good performances in capturing the tail dependence structure of the extreme rainfall data. The Schlather model suggested a rather strong dependence in the data even at far distances. Also, the model selection procedure based on the TIC metric suggested that the Extremal-t model is the superior model given its lowest TIC value among others. Therefore, the Extremal-t process was identified as the best performing max-stable model and was used to extrapolate the extreme return levels.

The spatial distribution of the location, scale, and shape parameters of the GEV distribution by the Extremal-t model demonstrated that the first two parameters have a similar spatial pattern with higher values over the western areas of the PNW region. This pattern was similar to that of the mean annual precipitation and demonstrated that the longitude and mean annual precipitation were suitable covariates for that parameter. Also, the spatial pattern of the shape parameter seemed to be influenced by the elevation according to the DEM layer. Particularly, higher shape parameter values were observed in both shallow coastal regions and the high elevation areas. Return level maps for various return periods based on the Extremal-t model were similar to that of the location and scale parameters in terms of spatial distribution. Also, the most intense extreme events were observed in the coastal areas of the Washington state, to the west of the Cascade mountain range and near the Olympic mountain.

The Extremal-t model was validated in three steps: 1) The model's performance in capturing the dependence structure of the data was verified. QQ plots for the pairwise and the groupwise maxima at some randomly selected locations showed that there was a good agreement between the model simulations and observations for the sites located at various distances;

2) The quality of the model fit to the data was assessed by comparing the return level estimates from the Extremal-t model with the empirical estimates from the bias-corrected PERSIANN-CDR data. It was shown that there is a good agreement between the two estimates at various return periods and locations over the study area; and 3) The model's overall performance in extrapolating the extreme quantiles was assessed using the ground-based rainfall observations. Return level plots generated by the gauge data at 27 stations over the PNW region were compared with the estimates by the Extremal-t model at the corresponding locations. The comparison showed that the extrapolated quantiles from the model agreed well with the gauge-based estimates at various locations and for different return periods.

Results of this study demonstrate the capabilities of the remotely sensed precipitation information for spatial extreme rainfall modeling over the poorly gauged regions. Specifically, the PERSIANN-CDR product fits well to this goal given its long record and high spatial resolution among those available remotely sensed sources of rainfall information. Yet, the length of the satellite-based information is relatively short compared to the long-term gauge data and the return periods often considered for the hydrological designs. Therefore, the applied statistical analysis tools must have sufficient mathematical foundation so that the extrapolations are logical and have lower uncertainties.

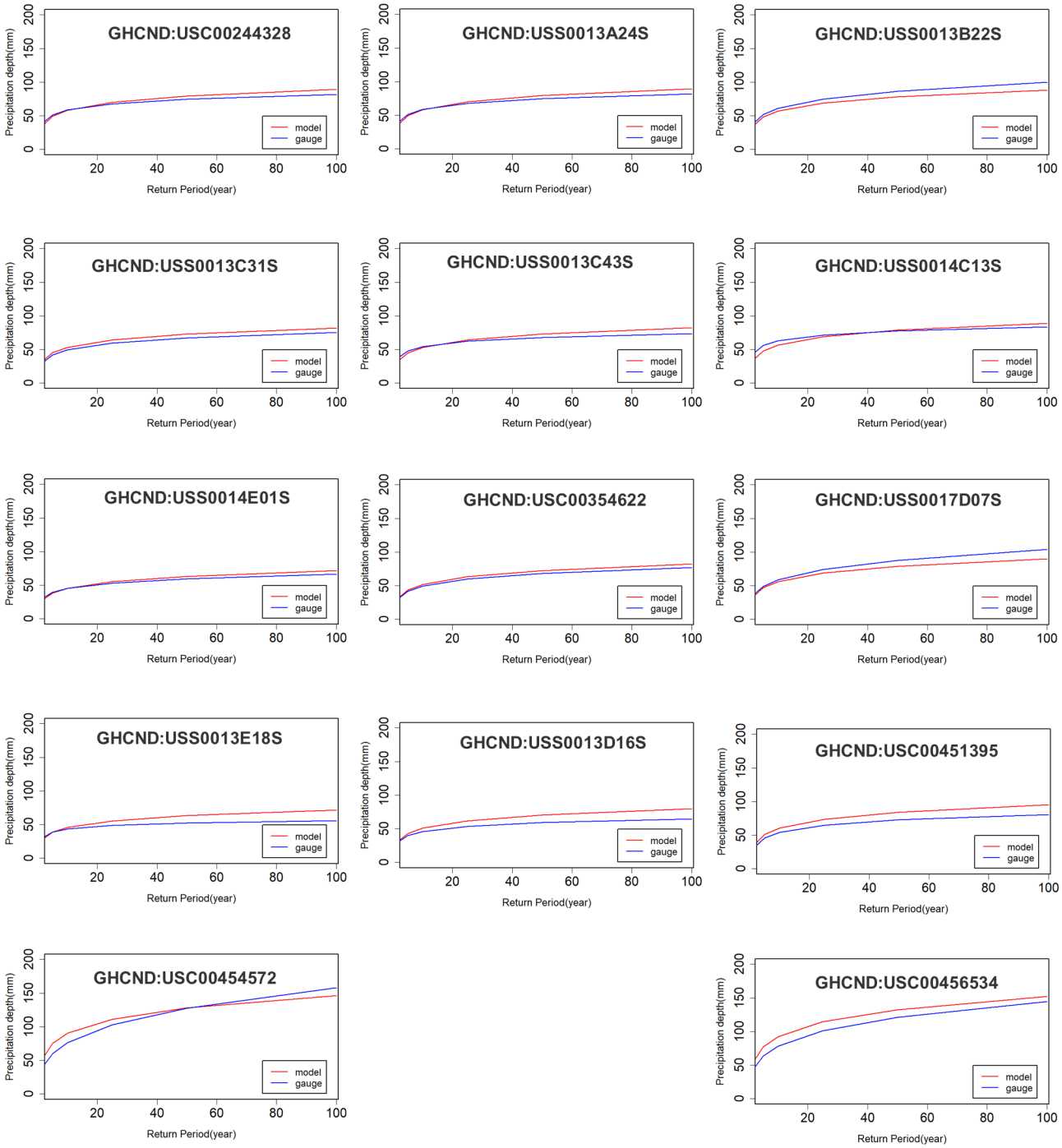

Figure 4.10: Return level plots by the Extremal-t process model and the gauge-based estimates at multiple gauge locations

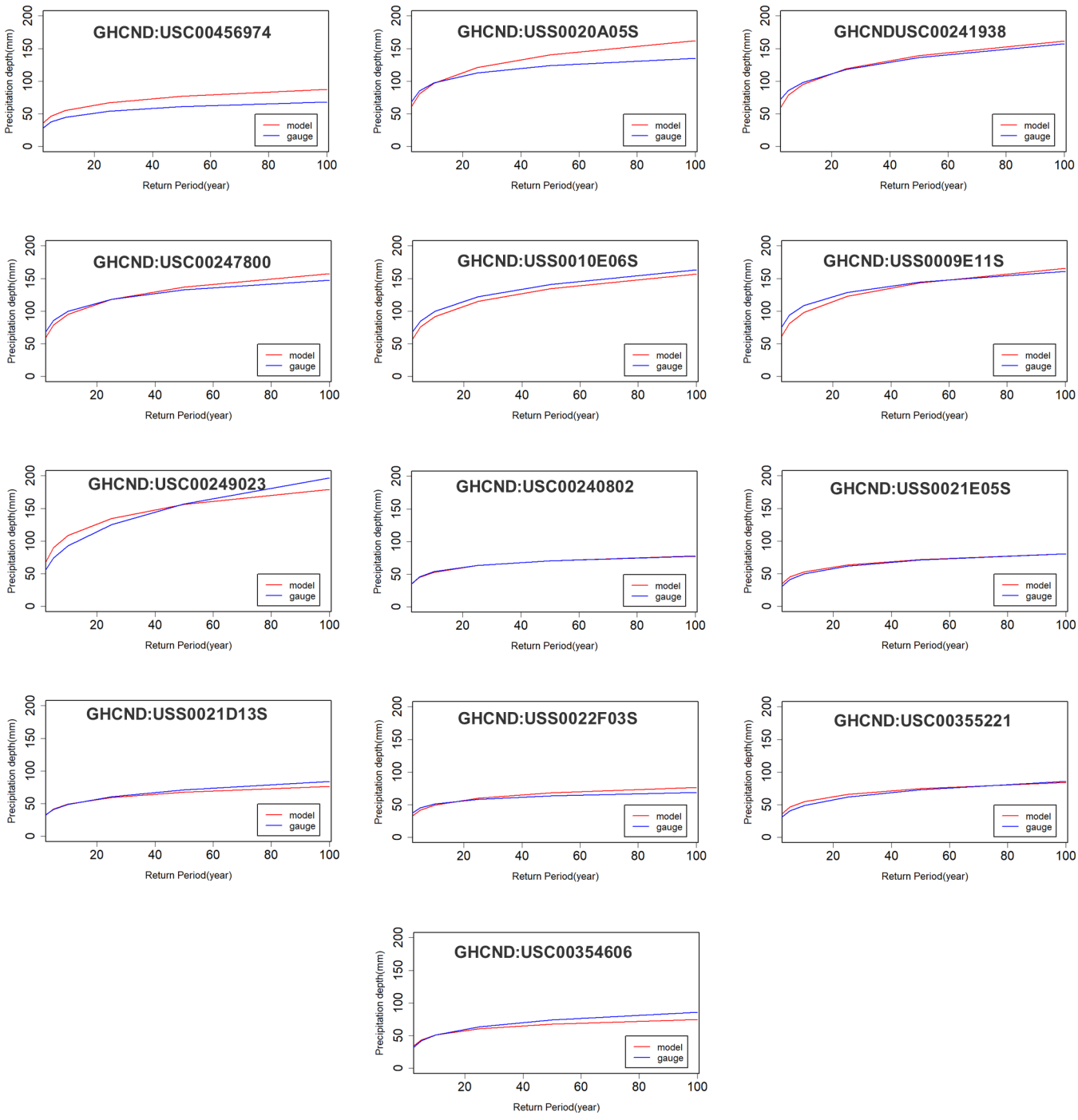

Figure 4.10: Continued

Chapter 5

Conclusions and Future Directions

Extreme precipitation events can cause major floods and may result in loss of lives and financial damages. Therefore, they need a careful modeling effort. The common approach for modeling extreme precipitation is based on using ground-based precipitation information from sparse gauge networks with short to long precipitation record and applying regional frequency analysis methods. This approach has been working effectively for the parts of the world that have sufficient observational networks. Yet, in many parts of the world, gauge networks are sparse and short. Sparse gauge networks cannot describe the spatial and temporal variation of extreme precipitation events that are highly variable in space and time. Also, extrapolated quantiles that are often required for hydrological applications (e.g. 100 year return level) are highly uncertain when they are estimated using short precipitation records. Limitations associated with the regional frequency analysis approaches together with the ad-hoc uncertainty assessment techniques commonly used, add to the complexity and unreliability of conventional approaches in poorly gauged regions. In recent years, remotely-sensed precipitation information, from weather radars and earth-observing satellites have been utilized for extreme precipitation modeling. This information could be very useful for the parts of the world that do not have abundant gauge information. Yet, given the

relatively short record of remotely-sensed rainfall datasets, extrapolating high quantiles from these sources is challenging. Therefore, advanced methodologies need to be applied so that extrapolations from such short records have sufficient mathematical foundation.

In this dissertation, an effort is made to present a framework by which remotely-sensed precipitation information can be reliably used for extreme precipitation modeling. The main focus of this dissertation is to minimize the existing gaps in the conventional extreme precipitation modeling approaches by: (1) investigating the possibility of applying satellite-based precipitation information for rainfall frequency analysis and evaluating the accuracy of RS-based quantile estimates with gauge-based observations; and (2) applying advanced statistical techniques that have sufficient mathematical basis and do not come with the limiting assumptions underlying conventional extreme precipitation modeling approaches. Given the necessity of long precipitation record, together with the high spatial and temporal resolution, PERSIANN-CDR which has one of the longest precipitation records among the remotely-sensed precipitation datasets, is used in this dissertation. Yet, methods and tools applied and proposed in this dissertation can be generalized and extended to other remotely-sensed precipitation datasets, as well.

In chapter 2, PERSIANN-CDR dataset is applied for rainfall frequency analysis in 20 basins across the United States. A bias-correction approach is proposed to adjust the PERSIANN-CDR estimates of extreme precipitation. This approach is implemented on the annual maximum time series estimates by PERSIANN-CDR dataset. The suggested approach is performed in two steps: (1) estimating correction factors using limited gauge information by applying a linear regression function that is based on elevation information; and (2) applying the estimated correction factors to adjust the annual maximum time series estimates by PERSIANN-CDR at ungauged regions. The proposed bias-correction approach is then used to adjust the PERSIANN-CDR extreme rainfall estimates and to perform rainfall frequency analysis and develop depth-duration-frequency curves at 16 basins in the continental United

States. It is shown that the suggested approach is effective in reducing the biases in the extreme rainfall estimates by PERSIANN-CDR dataset. Cross-validation results suggest that the bias-corrected extreme rainfall estimates are consistency more accurate than the gauge-interpolated estimates at poorly gauged regions. Also, it is demonstrated that the correction factors estimated using limited gauge information at a few basins can be generalized to other basins with similar climatic conditions. The bias-corrected estimates are then utilized for performing rainfall frequency analysis. Point-wise quantile estimates by the bias-corrected PERSIANN-CDR are compared with estimates from NOAA Atlas 14. It is shown that the frequency estimates from the bias-corrected PERSIANN-CDR dataset is consistent with NOAA Atlas 14. Therefore, it is show that the PERSIANN-CDR dataset is capable of being used for extreme precipitation modeling at ungauged basins.

In chapter 3 of this dissertation, a hierarchical Bayesian approach is applied to model extreme precipitation estimates by the bias-adjusted PERSIANN-CDR dataset. The applied approach is similar to RFA in that it uses information from nearby locations to generate consistent return level estimates; and to reduce uncertainties in the quantile estimates. However, it has several advantages to the conventional RFA approaches, such as: the ability to incorporate expert knowledge through the use of prior information, possibility of including additional physical and geographical information, and allowing to explicitly quantify the model uncertainties. The latent variable model (LVM) is used in this chapter to model extreme precipitation in Washington state. Parameter estimation is also implemented using MCMC algorithm. Using various model diagnostics measures, it is shown that the generated Markov chains are converged to their stationary distributions. Model verification showed that return level estimates from the LVM model fitted to the bias-corrected PERSIANN-CDR are consistent with the quantile estimates from the point gauge data. Also, comparison of the return level maps with that of the available literature showed that the satellite-based return level estimates are similar to the gauge-based estimates in terms of spatial pattern and magnitude. The constructed model is also capable of reasonably reducing the uncer-

tainties of the of the parameters and quantile estimates. It is worth mentioning that the constructed hierarchical model cannot capture the tail dependence structure of the extreme rainfall data due to the conditional independence assumption. Yet, if the goal of the modeling is to simulate the marginal properties of the data, such as the return level values at every single location in the study area, the LVM approach would be an effective choice. This is of interest especially in predicting flood hazards at large catchments where the point-wise IDF curves or return level maps are provided as inputs to the hydraulic and hydrological models Schubert et al. (2017). If the goal of modeling involves capturing the tail dependence structure of the data, a Max-stable process would be a better choice.

In chapter 4, a spatial extreme value modeling approach is taken to model extreme precipitation in the Pacific Northwest United States. Max-stable processes were applied in this chapter due to their abilities in modeling the tail dependence structure of the data, which was not achieved in the previous chapter because of the conditional independence assumption underlying the LVM approach. Max-stable processes are used in this chapter to model the marginal properties and the tail dependence structure of the extreme rainfall data, simultaneously. Conventional RFA approaches typically assume independence in the extreme data at neighboring sites which is not an accurate assumption. Abilities of Max-stable processes in capturing the asymptotic dependence in the extreme data make these models appealing for many geophysical applications which involve simulating the joint probabilities of extreme events. Various max-stable models including Schlather, Brown-Resnick, and Extremal-t are used in this chapter to model spatial extreme precipitation. Results of this chapter demonstrate superior performance by the Extremal-t process in modeling dependence structure of the extreme rainfall data. Also, this model suggest the lowest TIC value which is a measure of model quality. The best performing model was later used to generate return level maps and rainfall depth-duration-frequency curves. Constructed DDF curves by the Extremal-t model are also compared with the quantile estimates at 27 gauge locations. It is shown that the estimates by the Extremal-t model agree well with the gauge-based estimates at various

locations and return periods.

It is worth mentioning that we only applied a few covariates (i.e. elevation, latitude, longitude, and mean daily precipitation) for characterizing extreme precipitation in the constructed hierarchical and Max-stable models. Although these covariates were effective in capturing the spatial and temporal characteristics of extreme events, there might be other useful covariates that can better explain the extreme rainfall characteristics in different study regions. These covariates must be identified for each study area based on the factors that influence the precipitation mechanism in that specific region. For instance, when modeling extremes in Florida, Texas, and Louisiana, we probably need to take into accounts covariates that can explain the warm convective precipitation mechanism that impacts these regions.

In general, approaches and methods applied in this dissertation resulted in outstanding performance in modeling extreme precipitation from remotely-sensed information. This study serves as an introduction to the application of advanced statistical techniques, such as hierarchical Bayesian methods and Max-stable processes, for extreme precipitation modeling using gridded and remotely-sensed information. Yet, there are multiple directions for future investigation in order to further improve and enhance the extreme value modeling capabilities from remotely-sensed information.

- Given the short length of remotely-sensed precipitation datasets, extrapolating high quantiles from these datasets are highly uncertain. One way to remedy this limitation, is to take advantage from the peak-over-threshold approach (Solari et al., 2017). This way, the length of the extreme rainfall time series used for extreme value modeling is increased. As a result of the increased sample size, parameter estimation would be more accurate and less uncertain. Especially, the shape parameter of the GEV distribution which characterizes the tail behavior of this distribution could be more accurately estimated. A challenge here would be the automation of the threshold

selection procedure, given that a separate threshold must be selected for each pixel and when the size of the studied area becomes large relative to the resolution of the dataset, it becomes impossible to manually select the thresholds.

- Hierarchical Bayesian method and Max-stable processes approach applied in this study showed good performances in capturing the extreme rainfall characteristics from satellite datasets. However, running these models for large areas with too many pixels are likely to take too long. Specially, the hierarchical models are pretty slow and convergence of hierarchical models fed with a large number of pixels is hard to achieve. The latent variable model approach applied here is a simple hierarchical which has shown good performance in capturing the marginal properties of the data. Yet, more advanced techniques, such as the Hierarchical Kernel Extreme Value Process (HKEVP) (Reich and Shaby, 2012), or the the hierarchical model proposed by Dyrrdal et al. (2015) require more computational resources in order to converge in a reasonable time period. One way to advance the current work, would be to improve the computational efficiency of these methods using advanced statistical methods and utilizing more powerful processing units.

- The available remotely-sensed precipitation datasets suffer from serious limitations such as shortness of record(especially for radar data), poor spatial resolution (in the case of satellite-based estimates), and poor temporal resolution (daily and coarser for satellite-based datasets). Improvements in rainfall estimation methods (Akbari Asanjan et al., 2018; Sadeghi et al., 2019b,a), in terms of estimation accuracy and spatiotemporal resolutions, will contribute to the usefulness of remotely-sensed information for extreme precipitation modeling.

- The bias-correction method used throughout this dissertation could improve the accuracy of the extreme rainfall estimates. Yet, more advanced bias-correction techniques that can further improve the accuracy of the more intense events could result in more

accurate extreme precipitation models based on remotely-sensed datasets. Especially, as suggested by (Marra et al., 2019), use of downscaling methods that can preserve the correlation structure of the the rainfall fields from point-wise gauge information would be a solution (Foufoula-Georgiou et al., 2013; Zorzetto and Marani, 2019).

Bibliography

Adler, R., Sapiano, M., Huffman, G., Wang, J.-J., Gu, G., Bolvin, D., Chiu, L., Schneider, U., Becker, A., Nelkin, E., et al. (2018). The global precipitation climatology project (gpcp) monthly analysis (new version 2.3) and a review of 2017 global precipitation. *Atmosphere*, 9(4):138.

Adler, R. F., Huffman, G. J., Chang, A., Ferraro, R., Xie, P.-P., Janowiak, J., Rudolf, B., Schneider, U., Curtis, S., Bolvin, D., et al. (2003). The version-2 global precipitation climatology project (gpcp) monthly precipitation analysis (1979–present). *Journal of hydrometeorology*, 4(6):1147–1167.

Akbari Asanjan, A., Yang, T., Hsu, K., Sorooshian, S., Lin, J., and Peng, Q. (2018). Short-term precipitation forecast based on the persiann system and lstm recurrent neural networks. *Journal of Geophysical Research: Atmospheres*, 123(22):12–543.

Allen, R. J. and DeGaetano, A. T. (2005). Considerations for the use of radar-derived precipitation estimates in determining return intervals for extreme areal precipitation amounts. *Journal of Hydrology*, 315(1-4):203–219.

Ashouri, H., Hsu, K.-L., Sorooshian, S., Braithwaite, D. K., Knapp, K. R., Cecil, L. D., Nelson, B. R., and Prat, O. P. (2015). Persiann-cdr: Daily precipitation climate data record from multisatellite observations for hydrological and climate studies. *Bulletin of the American Meteorological Society*, 96(1):69–83.

Awadallah, A. G., ElGamal, M., ElMostafa, A., and ElBadry, H. (2011). Developing intensity-duration-frequency curves in scarce data region: an approach using regional analysis and satellite data. *Engineering*, 3(03):215.

Banerjee, S., Carlin, B. P., and Gelfand, A. E. (2004). *Hierarchical modeling and analysis for spatial data*. Chapman and Hall/CRC.

Ben-Zvi, A. (2009). Rainfall intensity–duration–frequency relationships derived from large partial duration series. *Journal of Hydrology*, 367(1-2):104–114.

Bonnin, G. M., Martin, D., Lin, B., Parzybok, T., Yekta, M., and Riley, D. (2006). Precipitation-frequency atlas of the united states. *NOAA atlas*, 14(2):1–65.

Bougadis, J. and Adamowski, K. (2006). Scaling model of a rainfall intensity-duration-frequency relationship. *Hydrological Processes*, 20(17):3747–3757.

Brown, B. M. and Resnick, S. I. (1977). Extreme values of independent stochastic processes. *Journal of Applied Probability*, 14(4):732–739.

Burn, D. H. (1990). Evaluation of regional flood frequency analysis with a region of influence approach. *Water Resources Research*, 26(10):2257–2265.

Chen, M., Shi, W., Xie, P., Silva, V. B., Kousky, V. E., Wayne Higgins, R., and Janowiak, J. E. (2008). Assessing objective techniques for gauge-based analyses of global daily precipitation. *Journal of Geophysical Research: Atmospheres*, 113(D4).

Coles, S. and Casson, E. (1998). Extreme value modelling of hurricane wind speeds. *Structural Safety*, 20(3):283–296.

Coles, S. G. and Tawn, J. A. (1991). Modelling extreme multivariate events. *Journal of the Royal Statistical Society. Series B (Methodological)*, pages 377–392.

Cooley, D., Cisewski, J., Erhardt, R. J., Jeon, S., Mannshardt, E., Omolo, B. O., and Sun, Y. (2012). A survey of spatial extremes: Measuring spatial dependence and modeling spatial effects. *Revstat*, 10(1):135–165.

Cooley, D., Naveau, P., and Poncet, P. (2006). Variograms for spatial max-stable random fields. In *Dependence in probability and statistics*, pages 373–390. Springer.

Cooley, D., Nychka, D., and Naveau, P. (2007). Bayesian spatial modeling of extreme precipitation return levels. *Journal of the American Statistical Association*, 102(479):824–840.

Cooley, D. and Sain, S. R. (2010). Spatial hierarchical modeling of precipitation extremes from a regional climate model. *Journal of agricultural, biological, and environmental statistics*, 15(3):381–402.

Cressie, N. A. (1993). Statistics for spatial data: Wiley series in probability and mathematical statistics. *Find this article online*.

Cunnane, C. (1988). Methods and merits of regional flood frequency analysis. *Journal of Hydrology*, 100(1-3):269–290.

Dalrymple, T. (1960). Flood-frequency analyses, manual of hydrology: Part 3. Technical report, USGPO,.

Davison, A. C., Padoan, S. A., Ribatet, M., et al. (2012). Statistical modeling of spatial extremes. *Statistical science*, 27(2):161–186.

De Haan, L. et al. (1984). A spectral representation for max-stable processes. *The annals of probability*, 12(4):1194–1204.

Demirdjian, L., Zhou, Y., and Huffman, G. J. (2018). Statistical modeling of extreme precipitation with trmm data. *Journal of applied meteorology and climatology*, 57(1):15–30.

Diggle, P. J., Tawn, J. A., and Moyeed, R. (1998). Model-based geostatistics. *Journal of the Royal Statistical Society: Series C (Applied Statistics)*, 47(3):299–350.

Dinku, T., Chidzambwa, S., Ceccato, P., Connor, S., and Ropelewski, C. (2008). Validation of high-resolution satellite rainfall products over complex terrain. *International Journal of Remote Sensing*, 29(14):4097–4110.

Doumounia, A., Gosset, M., Cazenave, F., Kacou, M., and Zougmore, F. (2014). Rainfall monitoring based on microwave links from cellular telecommunication networks: First results from a west african test bed. *Geophysical Research Letters*, 41(16):6016–6022.

Duan, Z., Liu, J., Tuo, Y., Chiogna, G., and Disse, M. (2016). Evaluation of eight high spatial resolution gridded precipitation products in adige basin (italy) at multiple temporal and spatial scales. *Science of the Total Environment*, 573:1536–1553.

Durrans, S. R., Julian, L. T., and Yekta, M. (2002). Estimation of depth-area relationships using radar-rainfall data. *Journal of hydrologic Engineering*, 7(5):356–367.

Dyrrdal, A. V., Lenkoski, A., Thorarinsdottir, T. L., and Stordal, F. (2015). Bayesian hierarchical modeling of extreme hourly precipitation in norway. *Environmetrics*, 26(2):89–106.

Eldardiry, H., Habib, E., and Zhang, Y. (2015). On the use of radar-based quantitative precipitation estimates for precipitation frequency analysis. *Journal of Hydrology*, 531:441–453.

Embrechts, P., Klüppelberg, C., and Mikosch, T. (2013). *Modelling extremal events: for insurance and finance*, volume 33. Springer Science & Business Media.

Endreny, T. A. and Imbeah, N. (2009). Generating robust rainfall intensity–duration–frequency estimates with short-record satellite data. *Journal of hydrology*, 371(1-4):182–191.

Faridzad, M., Yang, T., Hsu, K., Sorooshian, S., and Xiao, C. (2018). Rainfall frequency analysis for ungauged regions using remotely sensed precipitation information. *Journal of hydrology*, 563:123–142.

Fawcett, L. and Walshaw, D. (2006). A hierarchical model for extreme wind speeds. *Journal of the Royal Statistical Society: Series C (Applied Statistics)*, 55(5):631–646.

Foufoula-Georgiou, E., Ebtehaj, A. M., Zhang, S., and Hou, A. (2013). Downscaling satellite precipitation with emphasis on extremes: A variational 1-norm regularization in the derivative domain. In *The Earth's Hydrological Cycle*, pages 765–783. Springer.

Fowler, H. and Kilsby, C. (2003). A regional frequency analysis of united kingdom extreme rainfall from 1961 to 2000. *International Journal of Climatology: A Journal of the Royal Meteorological Society*, 23(11):1313–1334.

Gado, T. A., Hsu, K., and Sorooshian, S. (2017). Rainfall frequency analysis for ungauged sites using satellite precipitation products. *Journal of hydrology*, 554:646–655.

Gaume, J., Eckert, N., Chambon, G., Naaim, M., and Bel, L. (2013). Mapping extreme snowfalls in the french alps using max-stable processes. *Water Resources Research*, 49(2):1079–1098.

Gebregiorgis, A. and Hossain, F. (2014). Making satellite precipitation data work for the developing world. *IEEE Geoscience and Remote Sensing Magazine*, 2(2):24–36.

Gellens, D. (2002). Combining regional approach and data extension procedure for assessing gev distribution of extreme precipitation in belgium. *Journal of Hydrology*, 268(1-4):113–126.

Goudenhoofdt, E., Delobbe, L., and Willems, P. (2017). Regional frequency analysis of extreme rainfall in belgium based on radar estimates. *Hydrology and Earth System Sciences*, 21(10):5385–5399.

Greenwood, J. A., Landwehr, J. M., Matalas, N. C., and Wallis, J. R. (1979). Probability weighted moments: definition and relation to parameters of several distributions expressable in inverse form. *Water resources research*, 15(5):1049–1054.

Hailegeorgis, T. T., Thorolfsson, S. T., and Alfredsen, K. (2013). Regional frequency analysis of extreme precipitation with consideration of uncertainties to update idf curves for the city of trondheim. *Journal of Hydrology*, 498:305–318.

Hashemi, H., Nordin, M., Lakshmi, V., Huffman, G. J., and Knight, R. (2017). Bias correction of long-term satellite monthly precipitation product (trmm 3b43) over the conterminous united states. *Journal Of Hydrometeorology*, 18(9):2491–2509.

Hastings, W. K. (1970). Monte carlo sampling methods using markov chains and their applications.

Hershfield, D. M. (1961). Rainfall frequency atlas of the united states. *Technical paper*, 40.

Hong, Y., Gochis, D., Cheng, J.-t., Hsu, K.-l., and Sorooshian, S. (2007). Evaluation of persiann-ccs rainfall measurement using the name event rain gauge network. *Journal of Hydrometeorology*, 8(3):469–482.

Hosking, J. and Wallis, J. (1997). *Regional Frequency Analysis: An Approach Based on L-Moments*. Cambridge University Press.

Hosking, J. R. M. (1990). L-moments: Analysis and estimation of distributions using linear combinations of order statistics. *Journal of the Royal Statistical Society: Series B (Methodological)*, 52(1):105–124.

Hosking, J. R. M. and Wallis, J. R. (2005). *Regional frequency analysis: an approach based on L-moments*. Cambridge University Press.

Hsu, K.-l., Gao, X., Sorooshian, S., and Gupta, H. V. (1997). Precipitation estimation from remotely sensed information using artificial neural networks. *Journal of Applied Meteorology*, 36(9):1176–1190.

Huffman, G. J., Adler, R. F., Arkin, P., Chang, A., Ferraro, R., Gruber, A., Janowiak, J., McNab, A., Rudolf, B., and Schneider, U. (1997). The global precipitation climatology project (gpcp) combined precipitation dataset. *Bulletin of the American Meteorological Society*, 78(1):5–20.

Huffman, G. J., Bolvin, D. T., Nelkin, E. J., Wolff, D. B., Adler, R. F., Gu, G., Hong, Y., Bowman, K. P., and Stocker, E. F. (2007). The trmm multisatellite precipitation analysis (tmpa): Quasi-global, multiyear, combined-sensor precipitation estimates at fine scales. *Journal of hydrometeorology*, 8(1):38–55.

Jenkinson, A. F. (1955). The frequency distribution of the annual maximum (or minimum) values of meteorological elements. *Quarterly Journal of the Royal Meteorological Society*, 81(348):158–171.

Joyce, R. J., Janowiak, J. E., Arkin, P. A., and Xie, P. (2004). Cmorph: A method that produces global precipitation estimates from passive microwave and infrared data at high spatial and temporal resolution. *Journal of Hydrometeorology*, 5(3):487–503.

Katz, R. W., Parlange, M. B., and Naveau, P. (2002). Statistics of extremes in hydrology. *Advances in water resources*, 25(8-12):1287–1304.

Kidd, C., Becker, A., Huffman, G. J., Muller, C. L., Joe, P., Skofronick-Jackson, G., and Kirschbaum, D. B. (2017). So, how much of the earth's surface is covered by rain gauges? *Bulletin of the American Meteorological Society*, 98(1):69–78.

Knapp, K. R., Ansari, S., Bain, C. L., Bourassa, M. A., Dickinson, M. J., Funk, C., Helms, C. N., Hennon, C. C., Holmes, C. D., Huffman, G. J., et al. (2011). Globally gridded satellite observations for climate studies. *Bulletin of the American Meteorological Society*, 92(7):893–907.

Kotz, S. and Nadarajah, S. (2000). *Extreme value distributions: theory and applications*. World Scientific.

Kubota, T., Ushio, T., Shige, S., Kida, S., Kachi, M., and Okamoto, K. (2009). Verification of high-resolution satellite-based rainfall estimates around japan using a gauge-calibrated ground-radar dataset. *Journal of the Meteorological Society of Japan. Ser. II*, 87:203–222.

Langousis, A., Mamalakis, A., Puliga, M., and Deidda, R. (2016). Threshold detection for the generalized pareto distribution: Review of representative methods and application to the noaa ncdc daily rainfall database. *Water Resources Research*, 52(4):2659–2681.

Libertino, A., Sharma, A., Lakshmi, V., and Claps, P. (2016). A global assessment of the timing of extreme rainfall from trmm and gpm for improving hydrologic design. *Environmental Research Letters*, 11(5):054003.

Liu, C. and Zipser, E. J. (2009). "warm rain" in the tropics: Seasonal and regional distributions based on 9 yr of trmm data. *Journal of Climate*, 22(3):767–779.

Liu, X., Yang, T., Hsu, K., Liu, C., and Sorooshian, S. (2017). Evaluating the streamflow simulation capability of persiann-cdr daily rainfall products in two river basins on the tibetan plateau. *Hydrology and Earth System Sciences (Online)*, 21(1).

Lombardo, F., Napolitano, F., Russo, F., Scialanga, G., Baldini, L., and Gorgucci, E. (2006). Rainfall estimation and ground clutter rejection with dual polarization weather radar. *Advances in Geosciences*, 7:127–130.

Marra, F. and Morin, E. (2015). Use of radar qpe for the derivation of intensity–duration–frequency curves in a range of climatic regimes. *Journal of hydrology*, 531:427–440.

Marra, F., Morin, E., Peleg, N., Mei, Y., and Anagnostou, E. N. (2017a). Intensity–duration–frequency curves from remote sensing rainfall estimates: comparing satellite and weather radar over the eastern mediterranean. *Hydrology and Earth System Sciences*, 21(5):2389–2404.

Marra, F., Morin, E., Peleg, N., Mei, Y., and Anagnostou, E. N. (2017b). Intensity-duration-frequency curves from remote sensing rainfall estimates: comparing satellite and weather radar over the eastern mediterranean. *Hydrology and Earth System Sciences*, 21(5):2389–2404.

Marra, F., Nikolopoulos, E. I., Anagnostou, E. N., Bardossy, A., and Morin, E. (2019). Precipitation frequency analysis from remotely sensed datasets: A focused review. *Journal of Hydrology*.

Marra, F., Nikolopoulos, E. I., Anagnostou, E. N., and Morin, E. (2018). Metastatistical extreme value analysis of hourly rainfall from short records: Estimation of high quantiles and impact of measurement errors. *Advances in water resources*, 117:27–39.

Matheron, G. (1987). Suffit-il, pour une covariance, d'être de type positif. *Sciences de la Terre, série informatique géologique*, 26:51–66.

Mazdiyasni, O., Sadegh, M., Chiang, F., and AghaKouchak, A. (2019). Heat wave intensity duration frequency curve: A multivariate approach for hazard and attribution analysis. *Scientific Reports*, 9(1):1–8.

Miao, C., Ashouri, H., Hsu, K.-L., Sorooshian, S., and Duan, Q. (2015). Evaluation of the persiann-cdr daily rainfall estimates in capturing the behavior of extreme precipitation events over china. *Journal of Hydrometeorology*, 16(3):1387–1396.

Miller, J. F., Frederick, R. H., and Tracey, R. J. (1973). Precipitation-frequency atlas of the western united states.

Mujumdar, P. et al. (2018). Dependence structure of urban precipitation extremes. *Advances in Water Resources*, 121:206–218.

Naeini, M. R., Yang, T., Sadegh, M., AghaKouchak, A., Hsu, K.-l., Sorooshian, S., Duan, Q., and Lei, X. (2018). Shuffled complex-self adaptive hybrid evolution (sc-sahel) optimization framework. *Environmental Modelling & Software*, 104:215–235.

Norbiato, D., Borga, M., Sangati, M., and Zanon, F. (2007). Regional frequency analysis of extreme precipitation in the eastern italian alps and the august 29, 2003 flash flood. *Journal of hydrology*, 345(3-4):149–166.

Ombadi, M., Nguyen, P., Sorooshian, S., and Hsu, K.-l. (2018). Developing intensity-duration-frequency (idf) curves from satellite-based precipitation: Methodology and evaluation. *Water Resources Research*, 54(10):7752–7766.

Opitz, T. (2013). Extremal t processes: Elliptical domain of attraction and a spectral representation. *Journal of Multivariate Analysis*, 122:409–413.

Overeem, A., Buishand, A., and Holleman, I. (2008). Rainfall depth-duration-frequency curves and their uncertainties. *Journal of Hydrology*, 348(1-2):124–134.

Overeem, A., Buishand, T., and Holleman, I. (2009). Extreme rainfall analysis and estimation of depth-duration-frequency curves using weather radar. *Water resources research*, 45(10).

Padoan, S. A., Ribatet, M., and Sisson, S. A. (2010). Likelihood-based inference for max-stable processes. *Journal of the American Statistical Association*, 105(489):263–277.

Peleg, N., Marra, F., Fatichi, S., Molnar, P., Morin, E., Sharma, A., and Burlando, P. (2018). Intensification of convective rain cells at warmer temperatures observed from high-resolution weather radar data. *Journal of Hydrometeorology*, 19(4):715–726.

R Core Team (2013). *R: A Language and Environment for Statistical Computing*. R Foundation for Statistical Computing, Vienna, Austria.

Ragno, E., AghaKouchak, A., Love, C. A., Cheng, L., Vahedifard, F., and Lima, C. H. (2018). Quantifying changes in future intensity-duration-frequency curves using multimodel ensemble simulations. *Water Resources Research*, 54(3):1751–1764.

Reich, B. J. and Shaby, B. A. (2012). A hierarchical max-stable spatial model for extreme precipitation. *The annals of applied statistics*, 6(4):1430.

Renard, B. (2011). A bayesian hierarchical approach to regional frequency analysis. *Water Resources Research*, 47(11).

Ribatet, M. (2013). Spatial extremes: Max-stable processes at work. *Journal de la Société Française de Statistique*, 154(2):156–177.

Ribatet, M., Cooley, D., and Davison, A. C. (2012). Bayesian inference from composite likelihoods, with an application to spatial extremes. *Statistica Sinica*, pages 813–845.

Robert, C. and Casella, G. (2013). *Monte Carlo statistical methods*. Springer Science & Business Media.

Sadeghi, M., Akbari Asanjan, A., Faridzad, M., Afzali Gorooh, V., Nguyen, P., Hsu, K., Sorooshian, S., and Braithwaite, D. (2019a). Evaluation of persiann-cdr constructed using gpcp v2. 2 and v2. 3 and a comparison with trmm 3b42 v7 and cpc unified gauge-based analysis in global scale. *Remote Sensing*, 11(23):2755.

Sadeghi, M., Asanjan, A. A., Faridzad, M., Nguyen, P., Hsu, K., Sorooshian, S., and Braithwaite, D. (2019b). Persiann-cnn: Precipitation estimation from remotely sensed information using artificial neural networks-convolutional neural networks. *Journal of Hydrometeorology*, (2019).

Schlather, M. (2002). Models for stationary max-stable random fields. *Extremes*, 5(1):33–44.

Schlather, M. and Tawn, J. A. (2003). A dependence measure for multivariate and spatial extreme values: Properties and inference. *Biometrika*, 90(1):139–156.

Schubert, J. E., Burns, M. J., Fletcher, T. D., and Sanders, B. F. (2017). A framework for the case-specific assessment of green infrastructure in mitigating urban flood hazards. *Advances in Water Resources*, 108:55–68.

Sebille, Q. (2016). hkevp: A hierarchical model for spatial extremes. *R package version*, 1.

Sebille, Q., Fougères, A.-L., and Mercadier, C. (2017). Modeling extreme rainfall a comparative study of spatial extreme value models. *Spatial Statistics*, 21:187–208.

Shaby, B. A. and Reich, B. J. (2012). Bayesian spatial extreme value analysis to assess the changing risk of concurrent high temperatures across large portions of european cropland. *Environmetrics*, 23(8):638–648.

Shah, H. L. and Mishra, V. (2016). Uncertainty and bias in satellite-based precipitation estimates over indian subcontinental basins: Implications for real-time streamflow simulation and flood prediction. *Journal of Hydrometeorology*, 17(2):615–636.

Sharkey, P. and Winter, H. C. (2017). A bayesian spatial hierarchical model for extreme precipitation in great britain. *arXiv preprint arXiv:1710.02091*.

Shige, S., Kida, S., Ashiwake, H., Kubota, T., and Aonashi, K. (2013). Improvement of tmi rain retrievals in mountainous areas. *Journal of Applied Meteorology and Climatology*, 52(1):242–254.

Solari, S., Egüen, M., Polo, M. J., and Losada, M. A. (2017). Peaks over threshold (pot): A methodology for automatic threshold estimation using goodness of fit p-value. *Water Resources Research*, 53(4):2833–2849.

Sorooshian, S., Gao, X., Hsu, K., Maddox, R., Hong, Y., Gupta, H. V., and Imam, B. (2002). Diurnal variability of tropical rainfall retrieved from combined goes and trmm satellite information. *Journal of climate*, 15(9):983–1001.

Stedinger, J. R. (1993). Frequency analysis of extreme events. *in Handbook of Hydrology*.

Sveinsson, O. G., Boes, D. C., and Salas, J. D. (2001). Population index flood method for regional frequency analysis. *Water Resources Research*, 37(11):2733–2748.

Takeuchi, K. (1976). Distribution of informational statistics and a criterion of model fitting. suri-kagaku (mathematical sciences) 153 12-18.

Tao, Y., Yang, T., Faridzad, M., Jiang, L., He, X., and Zhang, X. (2018). Non-stationary bias correction of monthly cmip5 temperature projections over china using a residual-based bagging tree model. *International Journal of Climatology*, 38(1):467–482.

Turkman, K. F., Turkman, M. A., and Pereira, J. (2010). Asymptotic models and inference for extremes of spatio-temporal data. *Extremes*, 13(4):375–397.

Villarini, G., Smith, J. A., Baeck, M. L., Vitolo, R., Stephenson, D. B., and Krajewski, W. F. (2011). On the frequency of heavy rainfall for the midwest of the united states. *Journal of Hydrology*, 400(1-2):103–120.

Wallis, J., Schaefer, M., Barker, B., and Taylor, G. (2007). Regional precipitation-frequency analysis and spatial mapping for 24-hour and 2-hour durations for washington state. *Hydrology and Earth System Sciences*, 11(1):415–442.

Wiltshire, S. (1986). Regional flood frequency analysis i: Homogeneity statistics. *Hydrological Sciences Journal*, 31(3):321–333.

Wright, D. B., Mantilla, R., and Peters-Lidard, C. D. (2017). A remote sensing-based tool for assessing rainfall-driven hazards. *Environmental modelling & software*, 90:34–54.

Wright, D. B., Smith, J. A., Villarini, G., and Baeck, M. L. (2013). Estimating the frequency of extreme rainfall using weather radar and stochastic storm transposition. *Journal of hydrology*, 488:150–165.

Yang, T., Asanjan, A. A., Faridzad, M., Hayatbini, N., Gao, X., and Sorooshian, S. (2017). An enhanced artificial neural network with a shuffled complex evolutionary global optimization with principal component analysis. *Information Sciences*, 418:302–316.

Yang, X., Yong, B., Hong, Y., Chen, S., and Zhang, X. (2016). Error analysis of multi-satellite precipitation estimates with an independent raingauge observation network over a medium-sized humid basin. *Hydrological Sciences Journal*, 61(10):1813–1830.

Zhou, Y., Lau, W. K., and Huffman, G. J. (2015). Mapping trmm tmpa into average recurrence interval for monitoring extreme precipitation events. *Journal of Applied Meteorology and Climatology*, 54(5):979–995.

Zorzetto, E. and Marani, M. (2019). Downscaling of rainfall extremes from satellite observations. *Water Resources Research*, 55(1):156–174.